The response of seep and methane hydrate biogeochemical systems to variability in climate, hydrogeology, and trace metal availability

Theresa L Whorley

A dissertation

submitted in partial fulfillment of the

requirements for the degree of

Doctor of Philosophy

University of Washington

2021

Reading Committee:

Evan A. Solomon, Chair

John A. Baross

Randelle M. Bundy

Program Authorized to Offer Degree:

School of Oceanography

University of Washington

Abstract

The response of seep and methane hydrate biogeochemical systems to variability in climate, hydrogeology, and trace metal availability

Theresa L Whorley

Chair of the Supervisory Committee:
Professor Evan A. Solomon
School of Oceanography

Cold seeps are seafloor manifestations of fluid flow from deeper within marine sediments, and they are often locations where methane discharges into the ocean. These dynamic environments are typically found along continental margins and serve as biological oases for specialized seafloor macro- and meio-fauna as well as seafloor and subseafloor chemoautotrophic microorganisms.

Microbial methanogenesis is ubiquitous in the upper few 100s of meters of sediments along continental margins and, as such, continental margin sediments constitute an enormous geologic reservoir of methane. Methane exists as a dissolved component of pore water within continental margin sediments and concentrations are often high enough that methane can also exist as a free gas or is stored in methane hydrates. Burial of dissolved methane in pore water and sequestration within methane hydrate represent two important sinks that prevent the release of this greenhouse gas into the ocean/atmosphere system. The largest sink of microbial methane within marine sediments is the anaerobic oxidation of methane (AOM) performed by a syntrophic consortium of bacteria and archaea within pore water. Bisulfide produced by this reaction is transported to the seafloor where it serves as a key metabolic component for thiotrophic organisms. The amount of methane oxidized through AOM is variable but can be up to 100% of the dissolved methane flux to the seafloor. The reasons for variability in the efficiency of this process remains a pivotal unknown impacting estimates of methane input to the ocean from marine sediments.

This dissertation explores the response of cold seep and methane hydrate systems to environmental variability. Chapter 1 presents an introduction to microbially-mediated reactions in marine sediments including microbial methanogenesis and the anaerobic oxidation of methane, the global methane hydrate reservoir, and the importance and characteristics of the organisms involved in the vital process of AOM. In Chapter 2, pore water geochemical tracers are used to test the hypothesis that contemporary bottom water warming along the Washington sector of the Cascadia margin has induced widespread dissociation of buried methane hydrate

along the upper continental slope where the reservoir is most sensitive to changes in bottom water temperature. This work reveals that fluid emitted at actively venting seeps in this region is largely sourced from deeper mineral dehydration reactions and from meteoric water discharge, and is not the result of modern methane hydrate dissociation.

Chapter 3 presents the longest continuous record of time-series fluid flow rate and composition data at a cold seep to date. The time-series record documents the persistent downward flow of seawater directly beneath a *Beggiatoa* bacterial mat. *Beggiaotoa* is a filamentous bacterium common in reducing environments such as cold seeps that requires the upward flux of reduced sulfur for survival. Geochemical modeling shows that downward flow of fluid rich in electron acceptors stimulates enhanced rates of sulfate reduction and bisulfide production via AOM, driving a strong diffusional gradient of bisulfide to the seafloor. These results show that *Beggiatoa* can persist and thrive in regions of downward fluid advection, and that the shallow circulation of seawater at cold seeps increases the consumption of oxygen, nitrate, and sulfate from seawater, influencing local biogeochemical cycling

The research presented in Chapter 4 explores the possibility that anaerobic methanotrophic (ANME) archaeal communities involved in AOM are limited by the bioavailability of nickel in cold seep pore water, thus potentially impacting the efficiency of AOM in oxidizing methane before it can escape to the water column. Data presented in this chapter show that higher concentrations of bioavailable nickel exist at non-cold seep settings compared to cold seep settings where there is likely greater uptake and utilization of nickel from pore water to fuel ANME communities. It may be that ANME have successfully developed an evolutionary adaptation to acquire nickel from non-bioavailable forms, such as the production of nickel-specific extracellular ligands similar to siderophores. One or more of the organic ligands characterized in this study may be the result of such ligand expression. This study is the first to measure the bioavailability of nickel in marine pore water as well as to quantify and characterize organic nickel-binding ligands.

TABLE OF CONTENTS

LIST OF FIGURES

LIST OF TABLES

ACKNOWLEDGMENTS

This work would not have been possible without the many phenomenal teachers that fostered my curiosity of the wonders of the natural world and instilled in me the desire to always seek to learn more. Additionally, I firmly believe graduate school is impossible to endure without the confidence, support, and caring of a robust community. I am grateful to say that I have found a great community of friends and family and am privileged to have shared this journey with them.

I wish to thank my advisor, Evan Solomon, without whom I would not be nearly as critical of a scientist as I am today. His dedication to rigorous investigation of subseafloor processes has been inspirational. I appreciate his willingness to always sit down and discuss a new study or dataset, even until seven o'clock on a Friday night.

I also thank the members of my supervisory committee—Deb Kelley, Randelle (Randie) Bundy, John Baross, and Alex Gagnon—for their time, dedication, and guidance as well as their relentless enthusiasm. I particularly thank Randie Bundy for advising me in the research presented in Chapter 4. Her patience and calm guided me through several obstacles including navigating research and lab work during a global pandemic. Thank you also to Drew Gorman-Lewis who taught me everything I know about metal-ligand complexation.

My learning has benefitted immensely from the phenomenal faculty in the UW School of Oceanography. I am indebted to Mikelle Nuwer specifically for her guidance, support, and mentorship in learning not only how to be an effective teacher but also in demonstrating how to have a healthy work/life balance.

I am fortunate to have navigated graduate school with such phenomenal graduate students by my side. Rick Berg, Brendan Philip, Rita Aylward, and Claire McKinley have been excellent lab mates during my journey. Your friendship, calm, and companionship were invaluable. Thank you also to Romina Centurion, Lauren Kowalski, and Jamie Fields for your help acquiring the data presented in this dissertation both at sea and in the lab. I am thankful to the Ocean Observatories Initiative Regional Cabled Array team for letting me a part of your maintenance cruises. I specifically appreciate the guidance and mentorship from Deb Kelley and Orest Kawka. Our discussions have always been a joy.

Additionally, I am deeply grateful to have entered graduate school alongside the best cohort of students I could have hoped to call my friends. Angie Boysen, Susanna Michael, Robin McLachlan, Paige Levin, and Justin Penn have been unwavering supports during this journey and have always been available for hugs and compassion on those days when the slog seemed all too much. Thank you, especially, to Max Showalter who took on the extra duties of roommate and best friend.

Lastly, and most importantly, I thank my friends and family. Specifically, thank you to my wife, Haylee, for her unwavering support, encouragement, and strength during my graduate school journey. I look forward to our next big adventure together.

Chapter 1.

Introduction

1.1 Marine sediments in the global carbon cycle

Marine sediments cover approximately 70% of Earth's surface and store a vast quantity of carbon. Approximately 2,670 Pg C in the form of particulate organic carbon (POC) has been buried within marine sediments in just the last 11,700 years (LaRowe et al., 2020a). This inventory of geologically recent carbon is approximately 1.2–1.8 times more carbon than is stored as gas, oil, and coal (IPCC, 2013). Continental margin environments see the highest proportions of organic carbon burial compared to any other seafloor region (Burdige, 2007; Wallman et al., 2012; Keil 2017). High rates of nutrient input from land, primary productivity in the surface ocean, and terrestrial sedimentation contribute to an increased burial of organic matter within continental margin sediments (Hedges & Keil, 1995). Less than 1% of POC from photosynthetic production escapes remineralization in the water column and reaches the sediment, yet this carbon supply plays a key role in marine biogeochemical cycling (Rothman, 2002; Hedges & Keil, 1995; Schneider et al., 2006) and is the primary driver of microbially-mediated diagenetic reactions that support the sedimentary biosphere. The refractory fraction that is not degraded by microbial reactions is buried and stored over geologic time, representing a key sink in the global carbon cycle and regulating atmospheric oxygen concentrations over geologic timescales (Berner, 1989; D'Hondt et al., 2019; LaRowe et al., 2020b).

1.2 Early diagenesis of organic matter and methanogenesis

The early diagenesis of organic matter within marine sediments links the short-term, ocean-atmosphere carbon cycle with the longer-term cycle of carbon burial and eventual exhumation through volcanic and tectonic processes. POC buried in seafloor sediments is degraded by microbially-mediated biogeochemical reactions and fuels the deep marine biosphere, one of the largest ecosystems on Earth (Edwards et al., 2012). The large ecosystem of microbes in marine sediments is composed of expert chemoautotrophs capable of thriving under harsh conditions of low temperature, high pressure, and scant delivery of organic carbon. These communities of microorganisms gain energy by oxidizing organic carbon using a variety of electron acceptors present in buried pore water and sediments. The use of these electron acceptors forms a predictable sequence following decreasing Gibbs free energy yield known as the redox ladder (Figure 1.1, Table 1.1) (Claypool and Kaplan, 1974; Froelich et al., 1979).

The first electron acceptor to be depleted in pore water is oxygen (O_2). Once pore water O_2 is depleted, organic matter oxidation is coupled to nitrate (NO_3^-) reduction (Froelich et al., 1979) which has a lower Gibbs free energy yield than aerobic respiration. Once NO_3^- is depleted, bacteria predominantly reduce manganese- and iron-oxides to fuel metabolism, followed by the reduction of sulfate (SO_4^{2-}) once the previous electron acceptors are exhausted (Claypool and Kaplan, 1974). In continental margin sediments, high delivery of organic material leads to the total consumption of O_2 and NO_3^- in the upper millimeters to centimeters of sediment. The majority of organic matter oxidation in this environment is supported using SO_4^{2-} as an electron acceptor (Thullner et al., 2009). Following the reduction of all SO_4^{2-}, the final rung of the redox ladder is the fermentation of organic carbon coupled to the reduction of carbon dioxide (CO_2) with hydrogen (H_2), which produces methane (CH_4) as a byproduct. The depth within marine sediments marking the depletion of SO_4^{2-} and production of CH_4 is known as the sulfate-methane transition zone (SMTZ). Rapid utilization of electron acceptors within continental margin pore waters promotes microbial methanogenesis at shallow sediment depths (e.g. Claypool and

Kaplan, 1974; Froelich et al., 1979; Malinverno, 2010; Wallmann et al., 2012). As a consequence, the upper few 100s of meters of continental margin sediments constitute a large geologic reservoir of this greenhouse gas.

Microbial methanogenesis via POC degradation is an ubiquitous process in continental margin sediments, accounting for up to 75% of POC degradation in some cases (Wallmann et al., 2012). This process is performed by a special group of archaea known as methanogens. Archaeal methanogenesis can proceed using a variety of substrates for carbon reduction including CO_2/H_2 (hydrogenotrophic, Equation 1.1), acetate (acetoclastic, Equation 1.2), and methylated compounds (methylotrophic) (Lang et al., 2015).

$$CO_2 + 4H_2 \rightarrow CH_4 + 2H_2O \qquad \text{(Eqn. 1.1)}$$

$$CH_3COOH \rightarrow CH_4 + CO_2 \qquad \text{(Eqn. 1.2)}$$

The CO_2/H_2 pathway is the most common methanogenic pathway in marine sediments **(**Thauer et al., 2008). An additional process that produces methane is the thermocatalytic degradation of complex organic molecules, known as kerogens, with peak generation occurring at temperatures in excess of 150ºC (Quigly & Mackenzie, 1988). Though this process tends to occur deeper than 1 km, thermogenic methane may be present in small quantities within shallow continental margin sediments where microbial methane production dominates.

1.3 Fate of methane in marine sediments

1.3.1 – Methane burial, hydrate formation, and the anaerobic oxidation of methane

Pore water methane concentrations increase with depth as buried POC is microbially converted to methane. Methane in continental margin sediments exists as dissolved, gaseous, or solid methane hydrate. Methane hydrate is composed of a water ice cage-like lattice surrounding free methane that is stable at moderate-to-high pressure and low temperature conditions where the concentration of pore water methane is in excess of methane hydrate saturation (Figure 1.2) (Zatsepina and Buffett, 1998). The region within marine sediments that meets the pressure and temperature conditions for hydrate formation is known as the methane hydrate stability zone (MHSZ). In general, the dissolved methane concentration in pore water exceeds saturation with respect to methane hydrate formation within a few 10s of meters below the SMTZ. Methane in excess of this saturation is stored as methane hydrate in continental margin sediments. Methane hydrates are disseminated in continental margin sediments worldwide, typically occupying a small fraction of sediment pore space.

The accumulation of dissolved methane in pore water creates a diffusional gradient of methane from the zone of methanogenesis to the SMTZ where the anaerobic oxidation of methane (AOM) imparts a major control on the escape of methane to the water column. AOM is performed by a consortium of anaerobic methanotrophic archaea and sulfate reducing bacteria that syntrophically oxidize methane and reduce sulfate to form bicarbonate (HCO_3^-) and bisulfide (HS^-) (Equation 1.3).

$$CH_4 + SO_4^{2-} \rightarrow HCO_3^- + HS^- + H_2O \qquad \text{(Eqn. 1.3)}$$

Reactive transport modeling of a hypothetical continental margin site with moderate concentration of POC and high sedimentation rate indicates AOM is a sink for 52% of microbial methane produced in marine sediments, methane hydrate formation is responsible for sequestering 9%, and the remaining 39% is ultimately buried (Wallmann et al., 2012).

1.3.2 – Cold seeps and AOM efficiency

Regions on the seafloor associated with upward advection of water and gas are known as cold seeps. Cold seep regions can be indirectly identified by the presence of distinct oases of benthic fauna in otherwise sparsely inhabited regions of the seafloor and hydroacoustic observation of bubble plumes emanating from the seafloor. Benthic organisms associated with cold seeps require the upward flux of reduced sulfur from AOM and overlying oxygen from bottom water to fuel metabolic and symbiotic processes (Suess, 2014). Filamentous bacteria, often belonging to *Beggiatoa* or *Thioploca*, are universal indicators of cold seeps and typically occupy areas of the strongest flux of reduced sulfur (e.g. Sahling et al., 2002; Suess, 2014). Additional common seep fauna include symbiotic clams, mussels, and tubeworms (Suess, 2014).

Fluid advection, bioturbation, and bubble-induced mixing all enhance the rate of AOM and thus increase local biogeochemical cycling and impact benthic communities (Figure 1.3). Bicarbonate produced from AOM (Equation 1.3) drives authigenic carbonate formation which consumes Ca^{2+} from pore water. Bisulfide, also produced from AOM, diffuses or is advected toward the seafloor where it is oxidized by filamentous bacterial mats, clams, mussels, or tubeworms using oxygen or nitrate (Equation 1.4). Clams and mussels bioturbate the sediment to access reduced sulfur and in doing so pump oxygen into the sediment, thereby promoting the reoxidation of reduced sulfur to sulfate (Equation 1.5).

$$HS^- + NO_3^- + H_2O + H^+ \rightarrow SO_4^{2-} + NH_4^+ \qquad \text{(Eqn. 1.4)}$$

$$HS^- + 2O_2 \rightarrow SO_4^{2-} + H^+ \qquad \text{(Eqn. 1.5)}$$

Gas ebullition at the seafloor irrigates the shallow sediment column and mixes bottom water with pore water. This bubble-induced mixing introduces fresh electron acceptors that enhance the rates of POC degradation (Haeckel et al., 2007).

The ability of AOM to trap methane before it reaches the ocean is known as the AOM filter efficiency, commonly defined as the percent of total methane flux that is oxidized at the SMTZ (Boetius & Wenzhöfer, 2013). In diffusion-dominated systems, AOM efficiency is nearly 100%. That is, AOM quantitatively consumes all of the methane that diffuses to the SMTZ. However, the AOM filter efficiency decreases significantly in cold seep environments (Boetius & Wenzhöfer, 2013). Free and dissolved gas can bypass the AOM filter and escape into the water column at cold seeps when the rate of fluid advection is sufficiently high. Many studies have modeled the rates of microbial methanogenesis in global ocean sediments but the efficiency of the AOM filter and the factor(s) that provide the strongest influence on filter efficiency in different cold seep systems remain elusive unknowns. As such, the quantity of methane input to the hydrosphere from global marine sediments is not well constrained (Boetius & Wenzhöfer, 2013). Methane that bypasses oxidation via AOM ultimately escapes to the water column where oxidation of methane by methanotrophic bacteria (Valentine et al., 2001) contributes to the dissolved inorganic carbon (DIC = CO_3^{2-} + HCO_3^- + CO_2) concentration of bottom waters (Equation 1.6).

$$CH_4 + 2O_2 \rightarrow CO_2 + 2H_2O \qquad \text{(Eqn. 1.6)}$$

1.4 Dissertation Summary

Cold seeps and methane hydrate reservoirs along continental margins are dynamic environments that respond to environmental changes on a range of timescales spanning from 10^{-1}–10^4 years (e.g. Wallmann et al., 2017). This dissertation aims to investigate the response of the methane hydrate reservoir to modern bottom water warming along the Washington sector of the Cascadia margin (Chapter 2), how dynamic processes at seeps impact rates of AOM and benthic biological communities (Chapter 3), and the potential of trace nutrient bioavailability to impact AOM efficiency at cold seep environments (Chapter 4).

1.4.1 – Chapter 2 – The response of upper continental slope methane hydrates to contemporary bottom water warming

The pressure and temperature conditions appropriate for methane hydrate formation typically spans water depths >300 m in the Arctic and >500 m along mid-latitude margins of the modern ocean (Ruppel, 2011**)**. The total thickness of the MHSZ is governed by the geothermal gradient. The base of the MHSZ (BMHSZ) is typically distinguishable in seismic reflection profiles by a bottom-simulating reflector that marks the boundary between methane hydrate bearing sediments above and free gas below. Estimates of the amount of carbon stored in marine methane hydrates range from 500–5,000 Gt C, comprising a significant portion of global carbon stored in geologic reservoirs (Pińero et al., 2013; Wallmann et al., 2012).

Methane hydrates are metastable and, thus, a reduction in pressure (e.g. sea level) or increase in temperature could cause hydrates to dissociate, releasing methane into pore water. Dissociation of hydrates in cold seep settings where fluid more easily bypasses the AOM filter would result in an injection of methane into the hydrosphere where deep ocean aerobic methanotrophs oxidize the methane to CO_2, thus adding to the pool of marine DIC.

The MHSZ within continental slope sediments progressively thins upslope and pinches out at the “feather edge” of hydrate stability. Shallow buried hydrates typically occupy the upper few 10s of meters of sediment and are most at risk to dissociation from changes in bottom water temperature and therefore are at risk of dissociating on geologically short timescales of 10^2–10^3 years (e.g. Berndt et al., 2014; Ruppel, 2011). Warmer bottom water temperatures along the feather edge of methane hydrate stability has the potential to perturb this shallow reservoir. Indeed, simulations of the diffusion of heat from warmer bottom water identified at the predicted feather edge of methane hydrate stability along the Washington (WA), USA margin have indicated that the gas hydrate stability zone (MHSZ) has retreated downslope by ~1–2 km, or ~40 m water depth between 1970 and 2013 (Hautala et al., 2014). Retreat of the MHSZ of the magnitude suggested by Hautala et al. (2014) has the potential to release a significant amount of methane into the sediment pore space. Fifteen years of hydroacoustic data along the WA margin shows a pronounced clustering of gas plumes around the predicted upper limit of methane hydrate stability, indicating potential methane release from dissociating hydrate (Riedel et al., 2018). Yet there is currently no direct evidence of active methane hydrate dissociation in response to the measured bottom water temperature change.

Research presented in Chapter 2 examines whether gas plumes identified along the expected upper limit of gas hydrate stability are fed by modern hydrate dissociation in response to increasing bottom water temperatures along the WA margin. This study analyzes pore water geochemistry from sediment cores collected at eight actively venting seeps to elucidate the source of emitted water and gas. None of the seeps investigated in this study yielded unambiguous geochemical evidence of contemporary gas hydrate dissociation hypothesized as a result of contemporary bottom water warming. All seeps sampled are likely long-lived and emit fluid from a variety of sources including smectite clay dehydration and potentially meteoric water. To explain the lack of geochemical evidence of gas hydrate dissociation as the source of fluid emission at the expected upper limit of methane hydrate stability, I postulate that the hydrate occurrence zone, defined as the region where pressure, temperature, and pore water methane concentration are conducive to hydrate formation, must be deeper in the sediment column than the penetration depth of heat from modern bottom water warming.

1.4.2 – Chapter 3 – Dynamic fluid flow and biogeochemical cycling at cold seeps

Fluid flow at cold seeps strongly influences communities of micro- and macro-organisms, chemical cycling, authigenic mineral formation, and the anaerobic oxidation of methane. Despite the importance of fluid and solute exchange with the ocean at seeps, our understanding of seep-related biogeochemical cycling is largely based on temporal snapshots from shallow (0–20 cm depth) sediment core pore water solute profiles, short-term benthic fluid flux meter deployments, or calculating advection from shallow temperature profiles (e.g. Torres et al., 2002; Tryon et al., 2002; Henry et al., 1992). Each snapshot likely does not capture the long-term state of fluid and chemical transport in these environments.

Southern Hydrate Ridge, approximately 90 km offshore Oregon, USA, is an example of a cold seep dominated by episodic gas expulsion and dynamic aqueous fluid flow, lush chemosynthetic communities, and massive near-surface gas hydrates. Many studies have sought to understand deep and near-surface water and gas transport in this broad region of upward fluid advection using a variety of techniques. Push core and multicore pore water solute profiles to 15–30 cm depth with concave down curvature in SO_4^{2-} and/or Ca^{2+} concentrations are evidence of the upward advection of fluid (Torres et al., 2002). However, downward flow at moderate rates to sediment depths greater than the push core penetration would appear as constant seawater values in the pore water chemistry, as commonly observed across seep sites (e.g. Torres et al., 2002; Vanneste et al., 2012). Short core modeling studies and short-term deployments of benthic fluid flux chambers may not fully capture the long-term state of advection and gas expulsion in the seep system (Suess and Whiticar, 1989; Carson et al., 1990; Torres et al., 2002; Tryon et al., 2002).

Torres et al (2002) modeled flow rates from 15 cm push cores along with hours-long benthic fluid flux chamber deployments to show that fluid flow at Southern Hydrate Ridge varies spatially in a complex hydrogeologic system. The authors of this study described three distinct fluid regimes at SHR: (1) discrete locations of methane ebullition possibly associated with methane hydrate destabilization; (2) upward advection of fluid at locations of dense bacterial mats overlying methane hydrate crusts; and (3) locations of downward advection of seawater into sediments associated with vesicomyid clam colonies.

Another study investigated the association of biological communities as visual proxies to estimate fluid flux rates at seep and non-seep settings, as well as quantified water and chemical flux rates and temporal and spatial heterogeneity within different biological communities at Hydrate Ridge (Tryon et al., 2002). This study deployed seven Chemical and Aqueous Transport (CAT) meters capable of measuring *in situ* fluid flow across the sediment-water interface via tracer injection as well as storing water samples for chemical characterization upon instrument recovery. CAT meters were deployed at non-seep sites with no identifiable surface biologic community, within chemosynthetic clam colonies (*Calyptogena pacifica*), or within microbial mats. Instrument deployments lasted 30 to 45 consecutive days each of the two years. The results in Figure 1.4 show the fluid flux rate and associated water chemistry for three CAT meters placed within microbial mats at SHR. Each of the three CAT meters show highly variable rates of fluid flow. Fluid flow rates range between -20 cm yr^{-1} to +1000 cm yr^{-1} depending on CAT location and day, where negative flow direction is into the sediment and positive flow direction is out of the sediment. A striking observation is that the instrument with the highest upward flux rates (99H) showed seawater concentration of both calcium and total sulfur during much of the deployment, which is not expected as the pore water composition at SHR is significantly modified from seawater at 10 m depth based on the ODP Leg 204 drilling results (Tomaru et al., 2006). The time-integrated fluid flow direction for each instrument is predominantly upward out of the sediment column over time, yet ODP temperature profiles at Hydrate Ridge show no curvature over the upper 100 m of the sediment column, indicating little-to-no upward flow of water. Curvature in the temperature profile would be observed if upward advection of fluid exceeded 10 cm yr^{-1} (Tréhu et al., 2006).

In 2013, two types of fluid flow meter, one CAT meter and one Mosquito meter, were deployed within a bacterial mat in an area known as Einstein's Grotto at SHR as part of the Ocean Observatories Initiative's Regional Cabled Array (OOI-RCA). Each instrument continuously sampled fluid flow and chemistry for one year and was then replaced each year thereafter during annual OOI-RCA maintenance cruises. This uninterrupted, multiyear record of long-term fluid flow and pore water chemistry represents a one-of-a-kind dataset that can be used to explore temporal fluctuations in seep fluid and chemical fluxes. Additional complementary qualitative data include time-series imaging and repeat seafloor surveys that document changes in seafloor communities that can be related to changes in flow regime. Chapter 3 focuses on data collected from Mosquito and CAT fluid flow meters between 2013 and 2018 to investigate long-term fluid and chemical flux across the seafloor underlying a bacterial mat community, rates of AOM, and how reduced sulfur is supplied to overlying communities of *Beggiatoa* at SHR.

Long-term monitoring of fluid flow and chemistry within the bacterial mat revealed chronic shallow circulation of seawater. *Beggiatoa* mat communities persistently colonized areas of the seafloor dominated by downward advection of seawater, contrary to conventional wisdom that these organisms only colonize areas characterized by the upward advection of HS^-. Seawater circulation drives enhanced fluxes of electron acceptors into the sediment column and as a result drives increased rates of microbial reactions within shallow pore water. This leads to enhanced consumption of O_2, NO_3^-, Ca^{2+}, and SO_4^{2-} as well as the production of alkalinity, thus amplifying the role of seeps in many marine biogeochemical cycles.

1.4.3 – Chapter 4 - Nickel bioavailability as a control of AOM efficiency

It is traditionally assumed that the process of AOM in cold seep environments is efficient in capturing >90% of methane before it reaches the water column (Knittel and Boetius, 2009). However, a recent study by Boetius and Wenzhöfer (2013) calculated AOM filter efficiency from 41 individual locations associated with 13 cold seep regions globally and showed that filter efficiency varies from 4–100% among seep systems. Low fluid flow systems tended to have ~80% methane filter efficiency whereas systems with intermediate to high fluid flow rates have ~20% efficiency, though the thresholds distinguishing low, intermediate, and high flow systems are undefined (Boetius and Wenzhöfer, 2013). The authors of this study proposed that high fluid flow rate and lack of bacterial mats and other fauna at the seafloor are reasons for areas of high methane escape to the water column (i.e. low AOM filter efficiency), but differences in the fitness of the microbial community performing AOM in these different regions may contribute to the wide variation in filter efficiency.

Anaerobic methanotrophic archaea (ANME) that couple with sulfate-reducing bacteria (SRB) to perform AOM are a novel type of archaea that are believed to be able to run the CO_2/H_2 metabolic pathway of methanogenesis in reverse to oxidize CH_4 into CO_2 (Equation 1.4)

(Krüger et al., 2003; Scheller et al., 2010; Thauer et al., 2010). Thus, it is assumed that the metabolic requirements for methanogens are identical to the requirements for ANME.

ANME possess one of the most metal-rich metabolisms known to modern biology and are considered one of—if not the—first forms of life on Earth. Many of the transition metals that are key to enzymatic processes are redox sensitive and were much more abundant in the marine environment before widespread oxygenation of the ocean ~2.4 Ga to 1.8 Ga (Anbar, 2008). With this rise in atmospheric oxygen, and therefore oceanic oxygen, came the geologically sudden trapping of these key metals in non-bioavailable forms (Glass and Dupont, 2017). Despite this obstacle, ANME and methanogenic archaea still persist and thrive in continental margin sediments.

Several different metals including iron, nickel, cobalt, zinc, tungsten, and molybdenum (Glass and Orphan, 2012; Glass et al. 2014) are required in varying concentrations for methanogen metabolism. The bioavailability of these metals to the methanogen community is largely unknown. Nickel is a potentially limiting nutrient to methanogen and ANME viability due to its low abundance in the modern ocean and the high cellular requirement (Schöndheit et al., 1979; Glass and DuPont, 2017) and vital nutrient limitation may be a reason for low filter efficiency at seep sites. The CO_2/H_2 metabolic pathway requires nickel for several hydrogenases and key enzymes that fuel cell growth and metabolism, particularly methyl-coenzyme M reductase (MCR) (Jaun and Thauer, 2007; Glass and Orphan, 2012). MCR catalyzes the final step of methanogenesis and the first step of the reverse reaction of methanotrophy (Krüger et al., 2014; Thauer et al., 2010) and contains the nickel-based cofactor F_{430}. Cofactor F_{430} encompasses 50-80% of total cellular Ni in ANME and methanogens and is found only in methane-metabolizing archaea (Diekert et al., 1981; Mayr et al., 2008).

A potential barrier for ANME to acquire trace metal nutrients is not only the total concentration of metals but also the bioavailability of these metals as determined by complexation (Jaun and Thauer, 2007; Glass et al., 2014). For example, if nickel is abundant in pore water but is strongly bound in complexes that ANME cannot access, the nickel available for growth and metabolism is drastically reduced. To date, there have been few trace metal clean measurements of subsurface trace metal distribution and no studies of the subsurface bioavailability of nickel in continental margin seeps where we expect enhanced AOM and lower probability of methane emission to the overlying bottom water.

In Chapter 4, I present measurements of the fraction of nickel that is accessible to ANME populations in pore water at two background, diffusion-dominated locations and two cold seep locations along the Hikurangi margin of New Zealand to understand if it is possible that low methanotrophic filter efficiency at seep sites may be a result of bioavailable nickel limitation at depth, thus reducing the amount of methanotrophy possible before methane escapes to the water column. The data from this research show that there is a higher concentration of bioavailable nickel in non-seep sediments than at seep locations, likely due to differences in nickel utilization and ANME community size in each type location. The results also show that a large fraction of pore water nickel is strongly bound in as-yet unidentified organic complexes. Ligands associated with these complexes are likely microbial in nature and potentially excreted for the specific purpose of regulating cellular uptake of nickel in response to metal limitation. This novel dataset, and the story it tells, spurs many new questions to be explored in future studies as we seek to understand the full scope of evolutionary adaptations ANME have overcome.

1.5 References

Anbar, A. (2008) Elements and Evolution. *Science* **322**: 1481-1482.

Berndt, C., Feseker, T., Treude, T., Krastel, S., Liebetrau, V., Niemann, H., Bertics, V.J., Dumke,

I., Dünnbier, K., Ferré, B., Graves, C., Gross, F., Hissmann, K., Hühnerbach, V., Krause, S., Lieser, K., Schauer, J., Steinle, L., 2014. Temporal Constraints on Hydrate-Controlled Methane Seepage off Svalbard. Science (80-.). 343, 284–287.

Berner, R.A. (1989) Biogeochemical cycles of carbon and sulfur and their effect on atmospheric oxygen over Phanerozoic time. *Global and Planetary Change* **1**(1-2):97-122.

Boetius, A. and Wenzhöfer, F. (2013) Seafloor oxygen consumption fuelled by methane from cold

seeps. *Nature Geoscience* **6**: 725-734.

Burdige, D.J. (2007) Preservation of Organic Matter in Marine Sediments: Controls, Mechanisms, and an Imbalance in Sediment Organic Carbon Budgets? *Chemical Reviews* **107**: 467-485.

Carson, B., Suess, E., Strasser, J.C. (1990) Fluid flow and mass flux determinations at vent sites on the Cascadia margin accretionary prism. *Journal of Geophysical Research* **95**(B6): 8891-8897.

Claypool, G.E. and I.R. Kaplan (1974) The Origin and Distribution of Methane in Marine Sediments. *Natural Gases in Marine Sediments* pp.99-139.

D'Hondt, S., Pockalny, R., Fulfer, V.M., Spivack, A.J. (2019) Subseafloor life and its biogeochemical impacts. *Nature Communications* **10**(1): 1-13.

Diekert, G., Konheiser, U., Piechulla, K., Thauer, R.K. (1981) Nickel requirement and factor F_{430} content of methanogenic bacteria. *Journal of Bacteriology* **148**(2): 459-464.

Edwards, K.J., Becker, K., and Colwell, F. (2012) The Deep, Dark Energy Biosphere: Intraterrestrial Life on Earth. *Annual Review of Earth and Planetary Sciences* **40**: 551-68.

Egger, M., Riedinger, N., Mogollón, J.M., Jørgensen, B.B. (2018) Global diffusive fluxes of methane in marine sediments. *Nature Geoscience* **11**: 421-425.

Froelich, P.N., Klinkhammer, G.P., Bender, M.L., Luedtke, N.A., Heath, G.R., Cullen, D., Hartman, B. (1979) Early oxidation of organic matter in pelagic sediments of the eastern equatorial Atlantic: suboxic diagenesis. *Geochimica et Cosmochimica Acta* **43**: 1075-1090.

Glass, J.B. and Orphan, V.J. (2012) Trace metal requirements for microbial enzymes involved in the production and consumption of methane and nitrous oxide. *Frontiers in Microbiology* **3**(61): 1-20.

Glass, J.B., Yu, H., Steele, J.A., Dawson, K.S., Sun, S., Chourey, K., Pan, C., Hettich, R.L., Orphan, V.J. (2014) Geochemical, metagenomic and metaproteomic insights into trace metal utilization by methane-oxidizing microbial consortia in sulphidic marine sediments. *Environmental Microbiology* **16**(6): 1592-1611.

Glass, J.B. and DuPont, C.L. (2017) Oceanic nickel biogeochemistry and the evolution of nickel use. In: *The Biological Chemistry of Nickel*, p. 12-26

Hautala, S.L., Solomon, E.A., Johnson, H.P., Harris, R.N., Miller, U.K. (2014) Dissociation of Cascadia margin gas hydrates in response to contemporary ocean warming. *Geophysical Research Letters*, *41* doi:10.1002/2014GL061606.

Haeckel, M., Boudreau, B.P., Wallmann, K. (2007) Bubble-induced porewater mixing: A 3-D model for deep porewater irrigation. *Geochimica et Cosmochimica Acta* **71**(21): 5135-5154.

Hedges, J.I. and R.G. Keil (1995) Sedimentary organic matter preservation: an assessment and speculative synthesis. *Marine Chemistry* **49**: 81-115.

Henry, P., Foucher, J-P., Le Pichon, X., Sibuet, M., Kobayashi, K., Tarits, P., Chamot-Rooke, N., Furuta, T., Schultheiss, P. (1992) Interpretation of temperature measurements from the Kaiko-Nankai cruise: Modeling of fluid flow in clam colonies. *Earth and Planetary Science Letters* **109**: 355-371.

IPCC (2013) *IPCC Fifth Assessment Report (AR5) – The physical science basis.*

Jaun, B. and Thauer, R.K. (2007) Methyl-Coenzyme M Reductase and its nickel corphin coenzyme F_{430} in methanogenic archaea. In: *Nickel and Its Surprising Impact in Nature, vol. 2*, p. 323-356.

Keil, R. (2017) Anthropogenic forcing of carbonate and organic carbon preservation in marine sediments. *Annual Reviews in Marine Science* **9**:151-172.

Knittel, K. and Boetius, A. (2009) Anaerobic oxidation of methane: Progress with an unknown process. *Annual Review of Microbiology* **63**(1): 311-334.

Krüger, M., Meyerdierks, A., Glöckner, F.O., Amann, R., Widdel, F., Kube, M., Reinhardt, R., Kahnt, J., Böcher, R., Thauer, R.K., Shima, S. (2003) A conspicuous nickel protein in microbial mats that oxidize methane anaerobically. *Nature* **426**(6968): 878-881.

Lang, K. *et al* (2015) New mode of energy metabolism in the seventh order of methanogens as revealed by comparative genome analysis of *'Candidatus Methanoplasma termitum'*. *Applied Environmental Microbiology* **81**:1338-1352.

LaRowe, D.E., Arndt, S., Bradley, J.A., Burwicz, E., Dale, A.W., Amend, J.P. (2020a) Organic carbon and microbial activity in nmarine sediments on a global scale throughout the Quaternary. *Geochimica et Cosmochimica Acta* **286**: 227-247.

LaRowe, D.E., Arndt, S., Bradley, J.A., Estes, E.R., Hoarfrost, A., Lang, S.Q., Lloyd, K.G., Mahmoudi, N., Orsi, W.D., Shah Walter, S.R., Steen, A.D., Zhao, R. (2020b) The fate of organic carbon in marine sediments – New insights from recent data and analysis. *Earth-Science Reviews* **204**:103146.

Malinverno, A. (2010) Marine gas hydrates in thin sand layers that soak up microbial methane. *Earth Planetary Science Letters* **292**:399-408.

Mayr, S., Latkoczy, C., Krüger, M., Günther, D., Shima, S., Thauer, R.K., Widdel, F., Jaun, B. (2008) Structure of an F430 variant from archaea associated with anaerobic oxidation of methane. *Journal of the American Chemical Society* **130**: 10758-10767.
oxidation of methane.

Piñero, E., Marquardt, M., Hensen, C., Haeckel, M., Wallmann, K. (2013) Estimation of the global inventory of methane hydrates in marine sediments using transfer functions. *Biogeosciences* **10**: 959-975

Quigley, T.M. & Mackenzie, A.S. (1988) The temperature of oil and gas formation in the sub-surface. *Nature* **339**(9): 549-552.

Riedel, M., Scherwath, M., Römer, M., Veloso, M., Heesemann, M., Spence, G.D. (2018) Distributed natural gas venting offshore along the Cascadia margin. *Nature Communications* **9**:3264.

Vanneste, H., Kelly-Gerreyn, B.A., Connelly, D.P., James, R.H., Haeckel, M., Fisher, R.E., Heeschen, K., Mills, R.A. (2011) Spatial variation in fluid flow and geochemical fluxes across the sediment-seawater interface at the Carlos Ribeiro mud volcano (Gulf of Cadiz). *Geochimica et Cosmochimica Acta* **75**: 1124-1144.

Rothman, D.J. (2002) Atmospheric carbon dioxide levels for the last 500 million years. *PNAS* **99**: 4167-4171.

Ruppel, C.D. (2011) Mehtane Hydrates and Contemporary Climate Change. *Nature Education Knowledge* **3**(10):29

Ruppel, C.D. and J.D. Kessler (2017) The interaction of climate change and methane hydrates. *Reviews of Geophysics* **55**: 1-43.

Sahling, H., Rickert, D., Lee, R.W., Linke, P., Suess, E. (2002) Macrofaunal community structure

and sulfide flux at gas hydrate deposits from the Cascadia convergent margin, NE Pacific. *Marine Ecology Progress Series* **231**: 121-138.

Scheller, S., Goenrich, M., Boecher, R., Thauer, R.K., Jaun, B. (2010) The key nickel enzyme of methanogenesis catalyses the anaerobic oxidation of methane. *Nature* **465**(3): 606-608.

Schneider, Schulz, and Hensen, *Marine Geochemistry* Chapter 9

Schönheit, P., Moll, J., Thauer, R.K. (1979) Nickel, cobalt, and molybdenum requirement for growth of *Methanobacterium thermautotrophicum*. *Archives of Microbiology* **123**: 105-107.

Suess, E. (2014) Marine cold seeps and their manifestations: geological control, biogeochemical criteria and environmental conditions. *International Journal of Earth Sciences* **103**(7): 1889-1916.

Suess, E. and Whiticar, M.J. (1989) Methane derived CO_2 in pore fluids expelled from the Oregon subduction complex. *Paleogeography, Paleoclimatology, Paleoecology* **71**: 119-136.

Telling, J.P., Hornibrook, E.R.C., and Parkes, R.J. (2005) CHAPTER TITLE *In:Hydrogeology of the Oceanic Lithosphere* Eds: Davis, E.E. and Elderfield, H.

Thauer, R.K. (1998) Biochemistry of methanogenesis: a tribute to Marjory Stephenson. *Microbiology* **144**: 2377-2406.

Thauer, R.K., Kaster, A.-K., Goenrich, M., Schick, M., Hiromoto, T., Shima, S. (2010) Hydrogenases from methanogenic archaea, nickel, a novel cofactor, and H_2 storage. *Annual Reviews in Biochemistry* **79**: 507-536.

Thullner, M., Dale, A.W., Regnier, P. (2009) Global-scale quantification of mineralization pathways in marine sediments: A reaction-transport modeling approach. *Geochemistry, Geophysics, Geosystems* **10**(10): 1-24.

Tomaru, H., Matsumoto, R., Torres, M.E., Borowski, W.S. (2006) Geological and geochemical constraints on the isotopic composition of interstitial waters from the Hydrate Ridge region, Cascadia Margin. In: Tréhu, A.M., Bohrmann, G., Torres, M.E., Colwell, F.S. (Eds.), *Proceedings of the ODP Scientific Results, Leg 204*: College Station, TX (Ocean Drilling Program), 1-20.

Torres, M.E., McManus, J., Hammond, D.E., de Angelis, M.A., Heeschen, K.U., Colbert, S.L., Tryon, M.D., Brown, K.M., Suess, E. (2002) Fluid and chemical flux in and out of sediments hosting methane hydrate deposits on Hydrate Ridge, OR, I: Hydrological provinces. *Earth and Planetary Science Letters* **201**: 525-540.

Tréhu, A.M., Bohrmann, G., Torres, M.E., and Colwell, F.S. (2006) Leg 204 synthesis: gas hydrate distribution and dynamics in the central Cascadia accretionary complex. *In* Tréhu, A.M., Bohrmann, G., Torres, M.E., and Colwell, F.S. (Eds.), *Proceedings of the Ocean drilling Program, Scientific Results*, 204: College Station, TX (Ocean Drilling Program), 1–40.

Tryon, M.D., Brown, K.M., Torres, M.E. (2002) Fluid and chemical flux in and out of sediments hosting methane hydrate deposits on Hydrate Ridge, OR, II: Hydrological processes. *Earth and Planetary Science* **201**: 541-557.

Valentine, D. L., Blanton, D. C., Reeburgh, W. S., et al.: Water col- umn methane oxidation adjacent to an area of active hydrate dis- sociation, Eel River Basin, Geochim. Cosmochim. Ac., 65(16), 2633–2640, 2001.

Vanneste, H., Kelly-Gerreyn, B.A., Connelly, D.P., James, R.H., Haeckel, M., Fisher, R.E., Heeschen, K., Mills, R.A. (2011) Spatial variation in fluid flow and geochemical fluxes across the sediment-seawater interface at the Carlos Ribeiro mud volcano (Gulf of Cadiz). *Geochimica et Cosmochimica Acta* **75**: 1124-1144.

Wallman, K., Pinero, E., Burwicz, E., Haeckel, M., Hensen, C., Dale, A., Ruepke, L. (2012) The Global Inventory of Methane Hydrate in Marine Sediments: A Theoretical Approach. *Energies* **5**: 2449-2498.

Wallman, K., Riedel, M., Hong, W.L., Patton, H., Hubbard, A., Pape, T., Hsu, C.W., Schmidt, C.,

Johnson, J.E., Torres, M.E., Andreassen, K., Berndt, C., Bohrmann, G. (2018) Gas hydrate dissociation off Svalbard induced by isostatic rebound rather than global warming. *Nature Communications* **9**(83):1-9.

Zatsepina, O.Y. and B.A. Buffett (1998) Thermodynamic conditions for the stability of gas hydrate in the seafloor. *Journal of Geophysical Research* **103**(B10): 24,127-24,139.

1.6 Figures & Tables

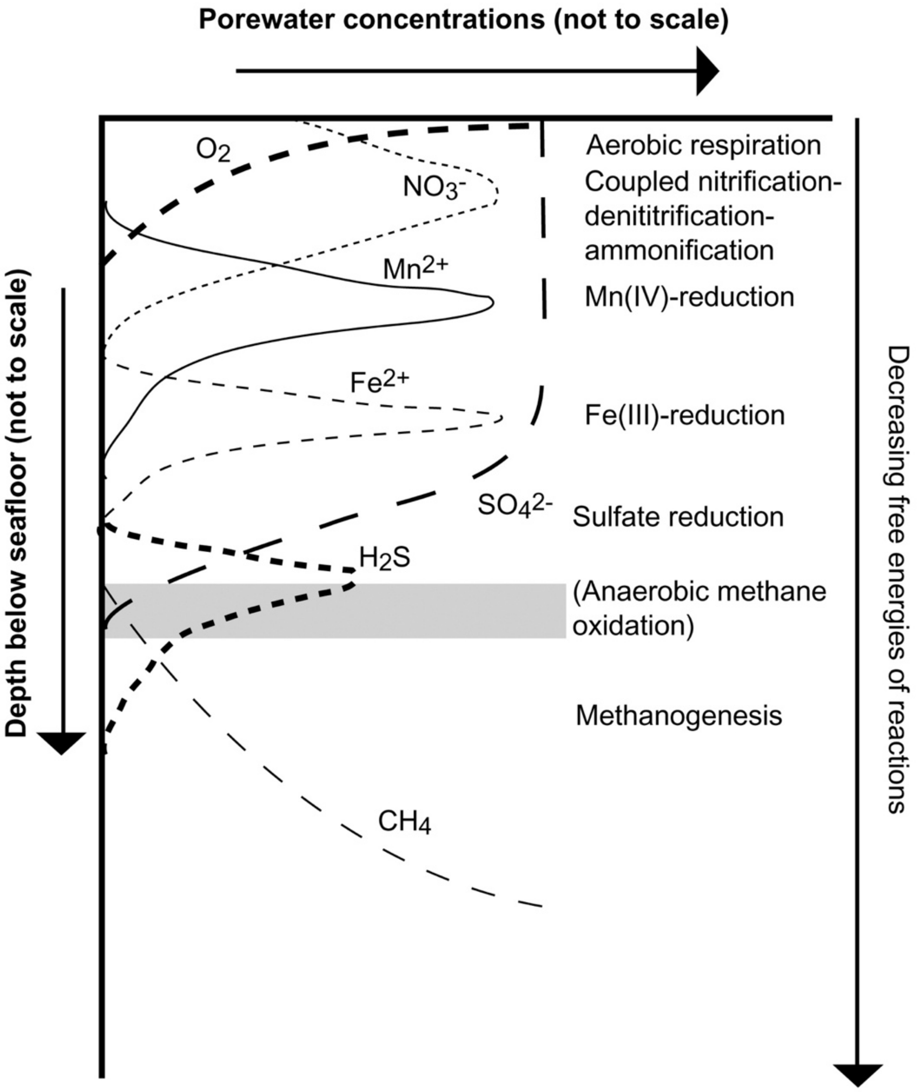

Figure 1.1. Idealized pore water profiles of major electron acceptors in marine sediment following the redox ladder. *(Image from Telling et al., 2005)*

Table 1.1. Equations for the reactions involved in the oxidation of organic carbon.

Redox Process	Reaction
Aerobic Respiration	$(CH_2O)_x(NH_3)_y(H_3PO_4)_z + (x\ + 2y)O_2 \rightarrow xCO_2 + (x + y)H_2O + yHNO_3 + zH_2PO_4$
Nitrate Reduction	$5(CH_2O)_x(NH_3)_y(H_3PO_4)_z + 4xNO_3^- \rightarrow xCO_2 + 3xH_2O + 4xHCO_3^- + 2xN_2 + 5yNH_3 + 5zH_3PO_4$
Manganese Reduction	$(CH_2O)_x(NH_3)_y(H_3PO_4)_z + 2xMnO_2(s) + 3xCO_2 + xH_2O \rightarrow 2xMn^{2+} + 4xHCO_3^- + yNH_3 + zH_3PO_4$
Iron Reduction	$(CH_2O)_x(NH_3)_y(H_3PO_4)_z + 4xFe(OH)_3(s) + 7xCO_2 \rightarrow 4xFe^{2+} + 8xHCO_3^- + 3xH_2O + yNH_3 + zH_3PO_4$
Sulfate Reduction	$2(CH_2O)_x(NH_3)_y(H_3PO_4)_z + xSO_4^{2-} \rightarrow xH_2S + 2xHCO_3^- + 2yNH_3 + 2zH_3PO_4$
Methane Production	$(CH_2O)_x(NH_3)_y(H_3PO_4)_z + xSO_4^{2-} \rightarrow xCH_4 + xCO_2^- + 2yNH_3 + 2zH_3PO_4$

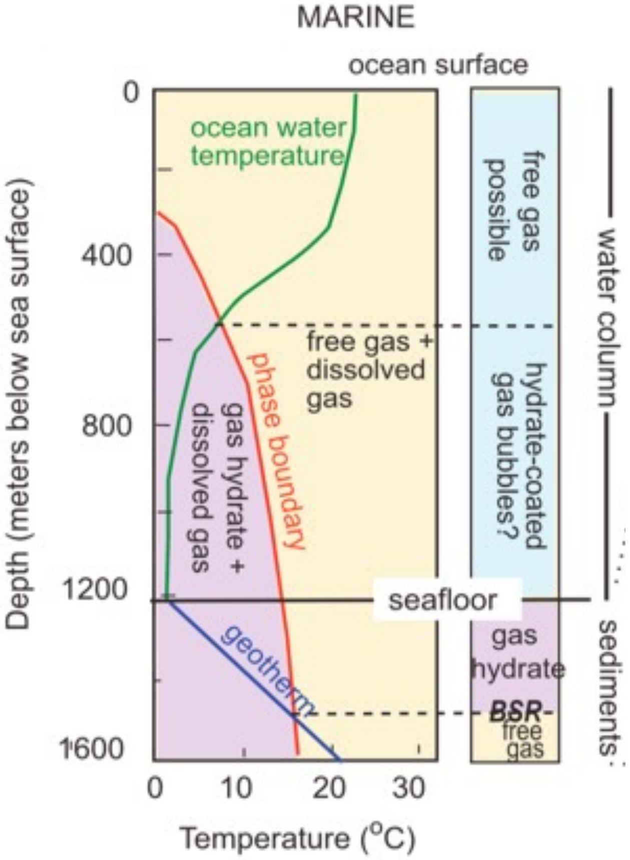

Figure 1.2. Example of the gas hydrate stability zone in the ocean and marine sediments. The schematic holds true for methane hydrate. The yellow region corresponds to the zone where methane can exist as free and dissolved gas. The purple region corresponds to gas hydrate and dissolved gas. Note that the concentration of dissolved methane in the water column is too low for methane hydrate to form. Dissolved methane concentrations only exceed saturation with respect to hydrate formation in continental margin sediments. The bottom-simulating reflector (BSR) indicates the base of the gas hydrate stability zone in seismic reflection profiles which is dictated by the geothermal gradient. The BSR is a seismic boundary between gas hydrate-bearing sediments (above) and free gas (below). (*Figure modified from Ruppel and Kessler (2017).*

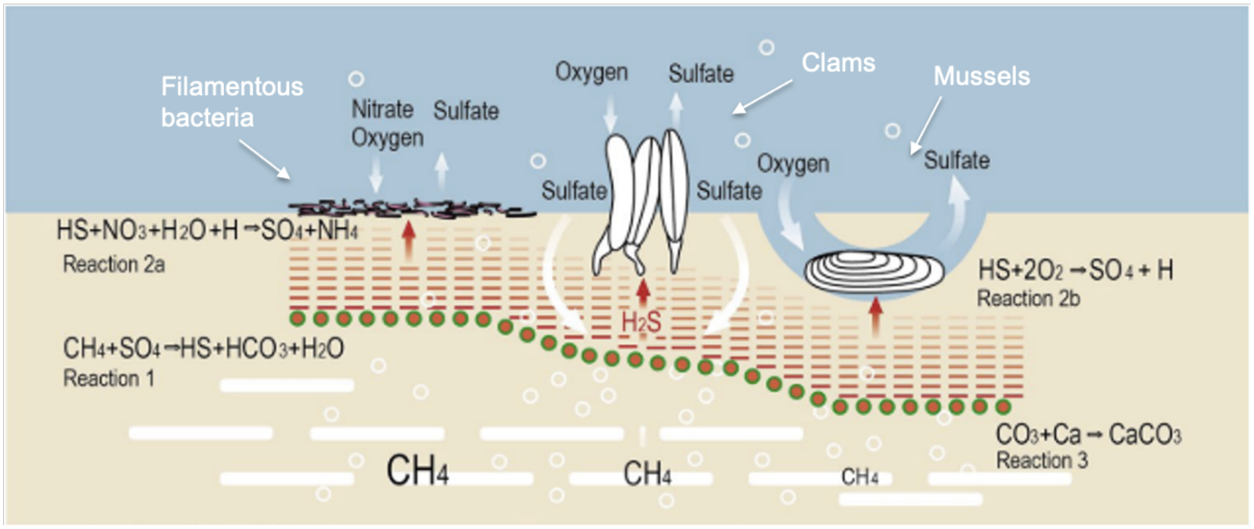

Figure 1.3. Dissolved and gaseous methane is advected to the seafloor in cold seep environments. AOM consortia, shown as red circles with green perimeter, catalyze the oxidation of dissolved methane and reduction of sulfate (Reaction 1). Bicarbonate produced from this reaction promotes in-situ formation of authigenic carbonate minerals which consumes Ca^{2+} from pore water (Reaction 3). Bisulfide (HS^-) produced from AOM diffuses or is advected to the surface where it is oxidized by filamentous bacterial mats, clams, mussels, or tubeworms (not shown) using oxygen or nitrate (Reaction 2a). Clams and mussels bioturbate the sediment to access reduced sulfur and in doing so pump oxygen into the sediment, thereby promoting the reoxidation of reduced sulfur to sulfate (Reaction 2b). *Figure modified from Suess, 2014.*

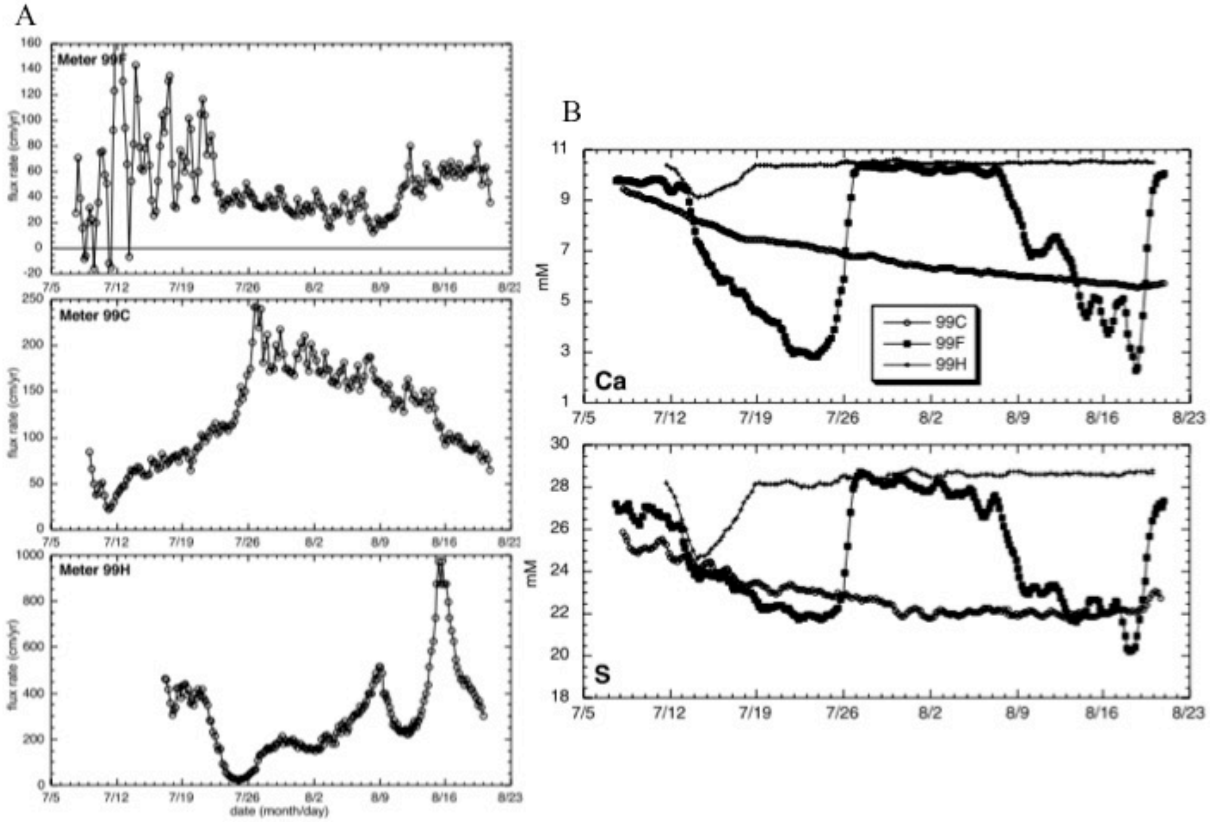

Figure 1.4. (A) Fluid flow rate measurements from CAT meters deployed in a bacterial mat at Southern Hydrate Ridge. (B) Time-series calcium and total sulfur fluid concentrations associated with flow rates for meters 99F, 99C, and 99H in (A). CAT 99H shows approximately seawater concentrations throughout most of the 45-day deployment, though the measured flow rates are upward the entire deployment period and are as high as 10 m yr^{-1}. *Figures taken from Tryon et al (2002)*.

Chapter 2.

Evaluating methane hydrate dissociation, mineral dehydration, and meteoric water as fluid sources for seeps along the upper slope of the Washington margin

Abstract

More than 30 years of bottom water temperature data from the upper continental slope of the Washington, USA margin show an increase in temperature at the predicted upper limit of gas hydrate stability. Simulations based on these records predict contemporary dissociation of this reservoir. To test whether there is contemporary methane hydrate dissociation along the Washington sector of the Cascadia margin, we conducted a systematic geophysical and geochemical survey of active seep sites along the upper edge of the gas hydrate stability zone (GHSZ) in October 2014. Pore water solutes and isotope ratios indicate a variety of fluid sources among the seeps. Pore water chloride concentrations decrease downcore at several seep sites, with measured values as low as 193 mM. Freshening at the more vigorous seep sites is mainly the result of clay mineral dehydration at depth and the input of meteoric water, whereas freshening at less vigorous sites appears to be from a combination of sources. We field-tested the use of noble gas ratios in vented fluid as a tracer of subsurface gas hydrate dissociation and found the tracer to be in good agreement with pore water geochemical data. Bottom water noble gas ratios clearly indicate active methane hydrate formation at a high-flux seep site just below the upper limit of stability. Noble gas ratios at seep sites slightly above the GHSZ do not show a clear signature of methane hydrate dissociation. While active seep sites are abundant on the WA margin at the expected upper limit of the GHSZ, none of the sites studied exhibit unequivocal geochemical evidence for modern methane hydrate dissociation as the main driver of fluid and gas discharge. It is likely that gas hydrates are buried deeper in the sediment column than the penetration depth of heat from a rise in modern bottom water temperatures.

2.1 Introduction

Continental margin sediments host large reservoirs of methane in dissolved, gaseous, and solid forms known as methane hydrate. Methane hydrate consists of a water ice cage-like lattice surrounding free methane gas, and forms under high pressure and low temperature conditions when the dissolved concentration of methane (CH_4) in pore water reaches saturation with respect to hydrate formation (Zatsepina and Buffett, 1998; Sloan, 1998). The quantity of carbon sequestered in the global methane hydrate reservoir is still poorly constrained (Ruppel & Kessler, 2017), but current estimates range from approximately 550 Gt of carbon (Piñero et al., 2013) to 1500 Gt C (Boswell and Collett, 2011). The release of this stored CH_4 into the ocean and atmosphere has been posited as a potential positive feedback to previous warming periods in Earth's history (e.g. Dickens et al., 1997; Kennett et al., 2003) and modern climate change (Zachos et al., 2008). The most climate sensitive portion of the marine hydrate reservoir is buried shallowly on upper continental slopes at the upper edge of hydrate stability (Ruppel and Kessler, 2017; Ruppel, 2011) which accounts for ~3.5% of the global hydrate reservoir (Ruppel, 2011). The methane hydrate stability zone (MHSZ) within marine sediments is thicker than 100 m at water depths greater than 1 km and progressively thins upslope pinching out at the "feather edge" of hydrate stability at ~500 meters below sea level (mbsl) on the Washington (WA) margin (Hautala et al., 2014). Upper continental slope deposits at the feather edge of the MHSZ are sensitive to transient bottom water temperatures and modeling studies suggest they can dissociate on relatively short timescales of decades to centuries of warming (e.g. Berndt et al., 2014; Hautala et al., 2014; Ruppel, 2011). Despite the acute climate-induced vulnerability of hydrates within these shallow environments, widespread CH_4 seepage at the feather edge of methane hydrate stability has so far only been recognized on the West Spitsbergen margin

(Westbrook et al., 2009), the western Atlantic margin (Skarke et al., 2014), and the Cascadia margin in the northeastern Pacific (Johnson et al., 2015, Riedel et al., 2018).

Widespread CH_4 release from the seafloor was first documented offshore western Svalbard in 2008 where predominantly CH_4 gas was sampled from plumes located at or above the present day upper edge of gas hydrate stability (Westbrook et al., 2009). Here, the source of CH_4 was hypothesized to be derived from actively dissociating gas hydrate in response to a 1°C rise in bottom water temperature associated with the West Spitsbergen Current since 1975 (Thatcher et al., 2013; Westbrook et al., 2009). Numerical model-based projections of the impact of continued Arctic bottom water warming (Biastoch et al., 2011) and simulations of the impact of warming on the hydrate inventory (Reagan et al., 2011) further demonstrated the plausibility of modern bottom water warming to induce gas hydrate dissociation in shallowly buried hydrate reservoirs. However, authigenic carbonates associated with these seeps have been forming for at least 3000 years (Berndt et al., 2014), pre-dating the onset of modern bottom water warming. Active gas hydrate dissociation in this region has since been confirmed by geochemical tracers (Wallmann et al., 2018). These results show modern hydrate dissociation is induced by isostatic rebound of the seafloor post-deglaciation of the Barents Sea ice sheet rather than contemporary bottom water warming (Wallmann et al., 2018).

Indeed, the influence of bottom water warming on gas hydrate reservoirs remains an active area of investigation. For example, regional hydroacoustic surveys documented widespread CH_4 emissions from seeps along the upper slope of the U.S. Atlantic margin (Skarke et al., 2014). The authors suggest that modern bottom water warming may be driving greater release of CH_4 from sediments at the sensitive upper limit of methane hydrate stability, which may contribute CO_2 to the dissolved inorganic carbon (DIC) pool through aerobic CH_4 oxidation in the water column (Skarke et al., 2014; Weinstein et al., 2016; Leonte et al., 2017). Thus, if widespread seepage is indeed related to gas hydrate destabilization, it is plausible that modern bottom water warming may cause an increase in CH_4 emissions at this and other mid-latitude margins and could be a significant source of carbon that is not accounted for in regional or global ocean DIC budgets.

Analysis of archive bottom water temperature data along the WA sector of the Cascadia margin collected between 1970 and 2013 from gliders, ARGO floats, and CTDs show a gradual warming trend at the upper limit of hydrate stability (Hautala et al., 2014). Thermal propagation simulations based on these bottom water records indicate that the MHSZ has retreated downslope by ~1–2 km (~40 m water depth) since the 1970s, and that the present upper limit of methane hydrate stability should be at ~500 mbsl (Hautala et al., 2014). Johnson et al (2015) showed that gas plumes were unusually clustered around 500-m isobaths along the WA margin. Riedel et al (2018) processed hydroacoustic data from 15 years of Cascadia margin cruises between 2001 and 2016 and concluded that, though the majority of known gas flares occur along the continental shelf at water depths <250 m, there is a strong cluster of gas plumes around the 500-m isobath when the data are normalized by bathymetry. The clustering of these gas plumes is more evident along the central WA margin between 47.5ºN and 48.25ºN where bottom water warming is most pronounced (Phrampus et al., 2017) compared to the rest of Cascadia.

Retreat of the MHSZ of the magnitude suggested by Hautala et al., (2014) has the potential to release a significant amount of CH_4 into the sediment column and possibly into the hydrosphere, but there is currently no direct evidence that methane hydrate dissociation is occurring. Studies using heat flow, subsurface imaging, and thermal modeling have inferred both the presence and absence of active hydrate dissociation feeding bubble plumes along the upper edge of hydrate stability (e.g. Berndt et al., 2014; Johnson et al., 2015; Thatcher et al., 2013). However, these studies lack evidence for hydrate occurrence that only geochemical fingerprinting of emitted fluids can provide.

This study examines if contemporary gas hydrate dissociation is occurring along the WA margin at the predicted upper limit of stability, and if not, what is supplying fluid and gas to these active venting sites. With global temperatures forecasted to continue to rise (Zachos et al., 2008), it is critical to understand the current response of the methane hydrate reservoir to bottom water warming at the sensitive upper limit of stability so that we may begin to understand the biogeochemical response to contemporary methane hydrate dissociation on this and other continental margins.

2.2 Geochemical Tracers of Gas Hydrate Dynamics and Diagenesis

Subseafloor reactions preferentially release and consume pore water solutes in predictable patterns. Here we use six geochemical tracers to elucidate fluid sources feeding seafloor seeps.

Chloride (Cl) is a conservative element in pore water and is a robust geochemical tracer of hydrate dynamics in low temperature environments (e.g. Ussler and Paull, 1995). Gas hydrates exclude salt during formation and incorporate only pure water and gas. Thus, methane hydrate formation leads to an increase in pore water Cl concentrations. Addition of fresh water from hydrate dissociation, clay mineral dehydration at depth, and deeper metamorphic reactions decrease the observed Cl concentration in pore water (Kastner et al., 1991; Kastner et al., 2014).

The oxygen and hydrogen isotopic signature of pore water combined with Cl deviations from seawater values can be used to distinguish the source of interstitial fluid freshening.

Methane hydrate dissociation causes an enrichment in pore water $\delta^{18}O$ and δD and a decrease in Cl concentrations. Fluids sourced from hydrous aluminosilicate dehydration are also fresh but are enriched in $\delta^{18}O$ and depleted in δD, thus can be distinguished from water released by methane hydrate dissociation. Meteoric water, which is depleted in $\delta^{18}O$ and δD compared to seawater, is an additional potential source of fluid freshening (Figure 2.1a, b).

Dissolved sulfate (SO_4^{2-}) is a major electron acceptor for the microbial oxidation of particulate organic carbon (POC) by bacterial communities in marine sediments (Claypool and Kaplan, 1974; Berner, 1980) (Equation 2.1).

$$CH_2O + SO_4^{2-} \rightarrow 2HCO_3^- + H_2S + H_2O \qquad \text{(Eqn. 2.1)}$$

Methane (CH_4) is microbially produced through the fermentation of POC coupled to the reduction of carbon dioxide (CO_2) during methanogenesis (Claypool and Kaplan, 1974) (Equations 2.2 and 2.3).

$$2(CH_2O) + 2H_2O \rightarrow 2CO_2 + 4H_2 \qquad \text{(Eqn. 2.2)}$$

$$CO_2 + 4H_2 \rightarrow CH_4 + 2H_2O \qquad \text{(Eqn. 2.3)}$$

This metabolic pathway is only energetically favorable in the absence of pore water sulfate (Claypool and Kaplan, 1974). The diffusion of CH_4 from below, and SO_4^{2-} from above, leads to a zone in marine sediments where these two chemical species coexist. At this depth, known as the Sulfate-Methane Transition Zone (SMTZ), a microbial consortium syntrophically oxidize CH_4 and reduce SO_4^{2-} during Anaerobic Oxidation of Methane (AOM), a low-energy yield process (e.g. Knittel and Boetius, 2009). Equation 2.4 shows the net reaction for AOM.

$$CH_4 + SO_4^{2-} \rightarrow HCO_3^- + HS^- + H_2O \qquad \text{(Eqn. 2.4)}$$

Pore water profiles of dissolved SO_4^{2-} concentrations can, therefore, reveal the depth at which CH_4 is produced.

The chemical reactions of AOM and POC-degradation produce bicarbonate (HCO_3^-). This HCO_3^- contributes to the alkalinity and DIC of the pore water and reacts with dissolved calcium and magnesium to produce authigenic carbonates. During methanogenesis, archaea preferentially consume ^{12}C, leaving the pore water enriched in ^{13}C. Thus, the $\delta^{13}C$-DIC of pore water tracks the evolution of methanogenesis over time.

The concentrations of major and minor elements within pore water track several *in situ* diagenetic reactions that commonly occur in margin settings, including ion exchange, volcanic ash alteration, microbial metabolic reactions, carbonate precipitation/dissolution, and silicate weathering as well as deep-sourced fluid production through clay dehydration.

The noble gas composition of water emitted from seeps at the seafloor may also be useful in constraining methane hydrate dynamics if the collected sample has undergone limited mixing with seawater. For example, laboratory experiments in the late-1960s showed that noble gases preferentially fractionate upon entering the hydrate structure (Barrer and Edge, 1967). Heavier noble gases, such as krypton and xenon, are incorporated into the structure while lighter gases, such as neon, are rejected. The incorporation or exclusion of argon within the crystal lattice is unbiased and, thus, may serve as a benchmark to normalize concentrations of those molecules impacted by hydrate dynamics. This relationship may distinguish hydrate-related release of CH_4 into the ocean from passive methane fluxes (e.g. Hunt et al., 2013). Field-based studies to examine the usefulness of this relationship on natural gas hydrate samples from Blake Ridge (Dickens and Kennedy, 2000) and Hydrate Ridge (Winckler et al., 2002) have been plagued by atmospheric contamination, among other issues. Here, we test the potential for noble gases to be used as a tracer of subsurface hydrate dynamics by measuring noble gas ratios in near-seep bottom water.

2.3 Materials & Methods

2.3.1 Sample Recovery and Preparation

All sampling occurred during a 10-day research expedition on the *R/V Thompson* (Expedition TN314) in October 2014. Along-margin multi-beam sonar surveys were conducted between 48ºN and 46ºN using a hull-mounted Kongsberg EM 302 and processed using QPS Fledermaus Midwater (version 7.3.0b). The survey focused on cataloguing bubble plumes between 475 and 520 mbsl and imaged 18 bubble plumes from 8 active seep sites within this predicted range of active hydrate dissociation (Figure 2.2). Twenty water column CTD hydrocasts were conducted above actively venting seep sites and background locations. Associated hydrocasts were taken from directly above each plume through the water column to near the sea surface. Hydrocasts were also employed up-stream and down-stream of principle current directions determined from real-time acoustic doppler current profiler (ADCP). Twenty-two gravity cores measuring between 1 and 3 m in length were collected at and around seep locations. Sediment plugs for porosity and CH_4 concentration measurements were taken every 5 to 10 cm and stored for shore-based analysis. Gravity cores were sectioned into 5 and 10 cm lengths and pore water was extruded using titanium squeezers under a hydraulic press. The pore water was then filtered through 0.2 µm syringe filters before being portioned into sampling vials and preserved for various post-cruise geochemical analyses.

2.3.2 Analytical Methods for Pore Water Geochemistry

Gran titration with 0.1 M HCl and optical refractometry were used to measure alkalinity and salinity shipboard, respectively, immediately following pore water recovery (Gieskes et al., 1991). All subsequent analyses were conducted onshore.

Chloride concentrations were evaluated via Mohr titration with silver nitrate (Gieskes et al., 1991) and sample concentrations reported are based on no fewer than duplicate analysis with an analytical precision of <0.2%. Concentrations were calculated by comparison to International Association of Physical Sciences of the Ocean (IAPSO) standard seawater. Pore water aliquots for sulfate analysis were portioned into centrifuge tubes and preserved with a zinc acetate solution shipboard and analyzed on a Metrohm 882 Compact Ion Chromatograph with a Metrosep A Supp 5–150/4.0 column at the University of Washington (UW). Sample concentrations were evaluated against dilutions of IAPSO and the analytical precision was <1.5%.

Samples for stable isotope ratio measurements of oxygen and hydrogen ($\delta^{18}O$ and δD) were preserved immediately on board in flame-sealed glass ampoules and later analyzed on a Picarro cavity ring-down spectrometer water analyzer at the UW. Results reported here are in standard delta (δ) notation relative to Vienna Standard Mean Ocean Water (VSMOW),

$$\delta(‰) = \left[\frac{R_{sample} - R_{standard}}{R_{standard}}\right] \times 1000$$

where R is the ratio of $^{18}O/^{16}O$. Precision of analysis was <0.05‰ for $\delta^{18}O$ and <0.5‰ for δD. Aliquots reserved for analysis of the stable carbon isotope ratio of dissolved inorganic carbon ($\delta^{13}C$-DIC) were first poisoned shipboard with mercuric chloride and analyzed via isotope-ratio mass spectrometry (IRMS) on a Delta V Mass Spectrometer/Gas Bench at Oregon State University (OSU). Data is reported here in the standard δ notation relative to Vienna Pee Dee Belemnite (VPDB); analytical precision was 0.05‰

Pore water samples for analysis of major and minor elements of seawater were pre-acidified shipboard with trace metal grade nitric acid. Major element samples were later prepared in a 1:101 dilution with a 1% HNO_3 solution and measured via inductively coupled plasma optical emission spectroscopy (ICP-OES) at the UW on a Perkin-Elmer 8300 ICP-OES with <2% precision. Minor element analysis was performed at OSU using a Leeman Labs Prodigy ICP-OES and samples were prepared in 1:20 and 1:100 dilutions using 1% HNO_3 solution. Precision of Li, B, and Sr were <3%, <3.3%, and <1.8%, respectively.

2.3.3 Analytical Methods for Water Column Geochemistry

Water column samples were collected for hydrocarbon analysis during CTD/hydrocast operations using a rosette of 24 Niskin bottles. Water from each depth interval was subsampled into glass vials and flushed with three volumes of seawater to expel any bubbles and were then sealed with butyl rubber septa and crimped with aluminum caps. Each sample was immediately spiked with a saturated solution of mercuric chloride and stored inverted to minimize diffusive gas exchange across the butyl rubber septa. Dissolved pore water hydrocarbon concentrations were measured in each sample using a gas chromatograph with flame ionization detector at UW.

At least two Niskin bottles were devoted to collecting water near the seafloor directly above each vent to capture the purest unaltered fluid for noble gas analysis. Water from these Niskin bottles was sub-sampled under vacuum and preserved in duplicate. Analysis of Ne, Ar, Kr, and Xe was conducted at the UW following the methods of Emerson et al (1999). Values presented here are percentages of *in situ* saturation for Ne, Kr, and Xe gas with respect to Ar. Percentages greater or less than atmospheric equilibrium were calculated according to the formula below, where Ne is used as an example:

$$\frac{Ne}{Ar}_{sat}(\%) = \left(\frac{\frac{Ne}{Ar}_{smp}}{\frac{in\ situ\ Ne_{atm}}{in\ situ\ Ar_{atm}}} - 1 \right) \times 100$$

Ne/Ar_{sat} is the percent saturation of the sample compared to the atmospheric ratio of Ne/Ar recalculated using *in situ* temperature, pressure, and salinity. Ne/Ar_{smp} is the measured Ne/Ar ratio and the subscript *atm* is the calculated noble gas concentration at *in situ* conditions.

2.4 Results

This study focuses on three of the eight studied seep sites (Figure 2.2; Table 2.1). The geochemistry of Site 6 (Section 2.4.1), the southernmost site where bubble plumes were detected along the walls of Astoria Canyon, is representative of typical geochemistry from all investigated seep sites except Sites 2 (Section 2.4.2) and 4 (Section 2.4.3) on the northern portion of the margin. Sites 2 and 4 display unique geochemistry indicating deeper-sourced fluid advection.

2.4.1 Site 6 – Astoria Canyon – GC31

Multiple bubble plumes were detected along the walls of Astoria Canyon at depths between 484 mbsl and 504 mbsl. These plumes are within the depth range of the predicted retreat of the GHSZ over the past 30 years. Gravity cores from this location contained disseminated authigenic carbonate. The pore water chemistry of these cores is representative of the majority of seeps studied. Here we present the geochemical results of GC31 (Figure 2.3) as the primary representative core.

Chloride concentrations vary little from modern seawater value with the largest deviation in concentration of 4.4% freshening from standard seawater (Figure 2.3). Sulfate concentrations decrease from 26 mM at the surface to less than 1 mM at 35 centimeters below the seafloor (cmbsf). The SO_4^{2-} concentrations are mirrored by an opposite trend in alkalinity. $\delta^{18}O$ and δD are relatively constant with depth. $\delta^{13}C$-DIC values of the pore water become lighter within the upper 15 cm to a minimum value of -9.56‰, then become heavier with depth to a maximum value of +18.99‰ at 215 cmbsf.

Pore water potassium (K) concentrations are slightly elevated compared to average seawater (10.5–12.7 mM). Magnesium concentrations are less than seawater at the surface of the core and decrease with depth to 40 mM. Calcium decreases from 8.9 mM at the top of the core to a minimum concentration of 2.2 mM at 50 cm before increasing slightly to 3.0 mM by 215 cmbsf. Boron and lithium concentrations decrease 31% and 71% from seawater values, respectively. Minimum strontium concentrations are 40% less than seawater value at depth (Figure 2.3).

2.4.2 Site 2 – Soft sediment mound – GC4 and GC5

Site 2 is the northernmost sampling location along our transect. This seep site had a strong bubble plume emanating from a soft-sediment mound within the predicted GHSZ at 520 mbsl (Figure 2.2b). Recovered gravity cores at this site captured chemosynthetic organisms and carbonate nodules at the sediment-water interface, indicating the location of active venting was surrounded by authigenic carbonates and chemosynthetic communities. Results from the two gravity cores closest to the venting area are discussed here (GC4 and GC5). The upper 15 cm of GC5 was fluid-dominated and displayed a mousse-like texture indicative of methane hydrate dissociation during core recovery. This shallow section of the core was not structurally stable and was subsequently lost upon core recovery.

Trends in the pore water chloride values of these two cores show significant freshening with depth. The freshest pore water fluid is diluted 65% from standard seawater in GC5 and 35% in GC4 (Figure 2.4). The SMTZ occurs at approximately 80 cmbsf. $\delta^{18}O$ values become 0.75‰ more positive than seawater value with depth for GC4 and 1.57‰ more positive for GC 5, while δD values become more negative by as much as 2.86‰ for GC4 and 5.65‰ for GC5. The top of GC4 was successfully recovered, as opposed to GC5, and $\delta^{18}O$ and δD values in this upper section are greater than +0.5‰ near the top of the core, and are sharply negative by 7.5 cmbsf. This isotopic shift preserves the signal of gas hydrate dissociation at the surface.

$\delta^{13}C$-DIC values in GC4 decrease to a minimum of -10.68‰ at the SMTZ, then increase to a maximum value of +21.52‰ at the base of the core. Due to the loss of the uppermost 15 cm of GC5, a potentially similar initial trend in $\delta^{13}C$-DIC is lost though the same positive increase in the carbon isotope ratio is present (Figure 2.4).

Chloride concentration is 65% less than seawater value and K and Mg are 78% and 95% less than seawater values, suggesting volcanic ash alteration along the fluid flow path (Kastner et al., 2014). Calcium concentrations in GC5 increase to 28.7 mM, approximately 2.7 times greater than average seawater despite both dilution and in situ removal in authigenic carbonates recovered in the core. Boron and lithium concentrations in GC5 increase with depth to values approximately 19 and 5.5 times greater than seawater values, respectively. Strontium concentrations increase with depth in both cores to concentrations as high as 4.8 times greater than seawater value.

2.4.3 Site 4 – Pockmark – GC16 and GC17

Multi-beam sonar imaging revealed three active bubble plumes emanating from depths between 473 and 489 mbsl. One plume at this location was venting from a pockmark measuring 120 m wide and 20 m deep. Acoustic imaging indicate this pockmark was bifurcated by extensional faults with authigenic carbonate scattered throughout the area. The tallest bubble plume extended from the pockmark to within 50 m of the sea surface, based on water column multi-beam survey data. Pore water data presented here are from two cores (GC16 and GC17) taken within the pockmark. GC17 showed considerable outgassing during core recovery with gas pockets in the core liner measuring 2–10 cm in length.

Trends in the pore water geochemistry data show that Cl concentrations in both cores are diluted between 34% and 56% from seawater value (Figure 2.5). The SMTZ depth for GC16 is approximately 80 cm, whereas SO_4^{2-} concentrations in GC17 decrease to <1 mM below 127 cm. This pattern is reflected in alkalinity data for GC17. Alkalinity data for GC16 are not reported for the entire core due to a shipboard analytical error, and as a result only the upper 20 cm of the core and five data points spanning the lower 130 cm are shown in Figure 2.5.

$\delta^{18}O$ and δD become lighter with depth in both cores, with δD becoming -7‰ lighter over the 2.6 m length of GC17. $\delta^{13}C$-DIC becomes lighter from 0–50 cmbsf to a minimum value of -17.40‰ then becomes heavier with depth to a maximum value of +32.56‰ at 257.5 cmbsf.

Potassium concentrations in GC16 show a decrease of 14% compared to seawater, and a 51% decrease in GC17, the latter approximately equal to the percent dilution seen in Cl concentrations. Magnesium decreases dramatically in both cores, by 63% in GC16 and 83% for GC17, each greater than the Cl dilution. Calcium concentrations decrease from near seawater values at the surface to <1 mM at depths below 116 cm in GC17. Strontium concentration decreases with depth to concentrations as low as 14 uM. Boron increases with depth to a concentration approximately 18 times greater than seawater, and Li concentrations remain at approximately seawater value with depth.

2.4.4 Water Column Noble Gas Ratios

Reported noble gas ratios are given as a percentage of *in situ* saturation for krypton (Kr), neon (Ne), and xenon (Xe) with respect to argon (Ar). The Ne/Ar value for Site 6 is less than background values, as seen in Figure 2.6. Kr/Ar and Xe/Ar values are elevated from background values, though the Xe/Ar ratio for this site is within the noise of the data. The Ne/Ar ratio at Site 2 is greater than background, whereas Kr/Ar and Xe/Ar values are both lower than background values. Site 4 noble gas ratio samples show Ne/Ar, Kr/Ar, and Xe/Ar ratios are all within the error of the measurement.

2.5 Discussion

Several geochemical tracers are used in concert to interpret subsurface gas hydrate dynamics below the seafloor. For example, dissociation of hydrate yields an enrichment in pore water ^{18}O, D (^{2}H), CH_4, Xe, and Kr, and a reduction in concentrations of Cl and Ne. We proceed by first discussing the source of fluid(s) at each seep site individually (Sections 2.5.1, 2.5.2, and 2.5.3) followed by the use of water column noble gas ratios as a tracer for gas hydrate dynamics (Section 2.5.4). We then discuss potential reasons for the observed lack of geochemical evidence of active hydrate dissociation (Section 2.5.5) and heterogeneity of seep fluid sources (Section 2.5.6).

2.5.1 Site 6 and majority of sampled seeps

The bubble plumes imaged and sampled at Site 6 were outside the GHSZ where hydrate is expected to have dissociated in response to bottom water warming over the past 30 years (Hautala et al., 2014). Pore water Cl concentrations do not exhibit the freshening signal that would be expected if active hydrate dissociation was indeed occurring and feeding the plumes. Rather, pore water profiles collected from Site 6 and the majority of seep sites sampled in this study indicate a fluid source with a chemical composition similar to seawater. $\delta^{18}O$ and δD in Site 6 pore water profiles are slightly offset in the negative direction from standard ocean water, but lack a clear indication of subsurface reactions that would release water and shift the $\delta^{18}O$ values in the negative direction. There is a pronounced 30‰ shift in $\delta^{13}C$-DIC values below the SMTZ and within the uppermost 50 cm of GC31. An extremely high rate of CH_4 production could produce this shift over the length of the gravity core, but this is unlikely. The combination of an advective SO_4^{2-} profile and positive shift in $\delta^{13}C$-DIC with depth indicates that there is strong upward advection of CH_4-rich water from depth with a source temperature lower than the onset of clay mineral dehydration at this site.

The decrease in Ca and Mg concentrations with depth indicates that these components are being consumed from the pore water as expected from authigenic carbonate formation. Authigenic carbonate is present within cores at this site as both nodules and disseminated. Assuming a geothermal gradient of 60ºC/km (Phrampus et al., 2017), fluids must be sourced from the upper kilometer of the sediment column because *in situ* smectite clay dehydration occurs at temperatures >60ºC and this reaction would decrease measured pore water Cl concentration and shift $\delta^{18}O$ and δD in the more negative and positive direction, respectively (e.g. Savin and Epstein, 1970; Pytte and Reynolds, 1989; Sheppard and Gilg, 1996). This fluid source depth is less than 1 km not only for Site 6, but Sites 3, 5, 8, and 9 as well. Fluid flow is likely driven by overpressure in the upper kilometer that is not associated with mineral dehydration reactions.

2.5.2 Deep-sourced fluid venting at Site 2

Site 2 is characterized by vigorous venting of fresh pore water and gas. The pore water stable isotope trends are characteristic of the signature expected from the dehydration of smectite clay to illite at depth (Figure 2.1) (Kastner et al., 2014; Kastner et al., 1991). The δ^{13}C-DIC profile for GC4 reaches a minimum value of -10.68‰ at the SMT, and values increase to +21.52‰ by 165 cm. The profile for GC5 shows similarly heavy δ^{13}C-DIC at depth with a minimum value of -9.72‰ measured at 17.5 cm depth, well above the SMT (Figure 2.4). These patterns of heavy δ^{13}C-DIC enrichment at depth require tapping of an evolved carbon source. The fluid advected to the surface must be sourced from a deep DIC reservoir that contains a large fraction of biogenic CH_4 produced from CO_2 reduction (Claypool and Kaplan, 1974; Pohlman et al., 2009).

Mg and K values are more depleted than can be accounted for by dilution from freshwater addition, and Ca in GC5 is nearly triple the concentration of standard seawater. This signal of Ca enrichment and Mg depletion is consistent with volcanic ash alteration/silicate mineral weathering to hydrous aluminosilicate minerals (Kastner et al., 2014). Potassium is also consumed during the production of illite (Kastner et al., 2014), which agrees with the increase in δ^{18}O and decrease in δD typical of clay dehydration at depth. Strontium concentrations are an order of magnitude greater than typical seawater concentrations; the high Sr concentrations at this site are unique compared to all other sites sampled and indicates higher temperature fluid-rock interaction at depth.

Smectite is a dominant mineral on the Cascadia margin (Underwood, 2007) and typically begins to dehydrate at approximately 60°C, with the majority of the dehydration complete by ~150°C (e.g. Pytte and Reynolds, 1989; Kastner et al., 2014). The formation temperature of the end-member dehydration fluid in Site 2 cores, therefore, must have been produced at temperatures of at least 60°C.

The temperature range and depth of fluid formation can be further constrained by applying well established chemical geothermometry relationships. The oxygen and hydrogen stable isotope relationships between seawater and smectite as a function of temperature are well defined (Capuano, 1992; Savin and Epstein, 1970; Sheppard and Gilg, 1996; Yeh, 1980) and can be used as a geothermometer to predict temperature of fluid formation assuming the formation fluid is in isotopic equilibrium with values for clay minerals and that temperature does not exceed 150°C (Sheppard and Gilg, 1996). Extrapolating Site 2 $\delta^{18}O$ and δD values to the fresh fluid end-member provides an estimate of the original isotopic ratios of the dehydration fluid before mixing during advection along the fluid flow path (Figure 2.7). $\delta^{18}O$ and δD of the Cl-depleted clay dehydration fluid were derived using a linear regression line for GC5 $\delta^{18}O$ and Cl (Figure 2.7a) and δD and Cl (Figure 2.7b) values. This extrapolation yields end-member values of +2.5‰ for $\delta^{18}O_{fluid}$ and -11.1‰ for δD_{fluid}. Using these results, the theoretical $\delta^{18}O$ and δD values for clay minerals at different temperatures (Figure 2.7c) were calculated. Theoretical equilibrium fractionation values were calculated for a range of temperature conditions using equations from Sheppard and Gilg (1996), Yeh (1980) and Capuano (1992), as previously done for seeps at the Costa Rica margin (Hensen et al., 2004). The natural $\delta^{18}O$ and δD variability of marine clays must then be known in order to constrain the temperatures and to define a range of possible fluid formation temperatures. An isotopic field of marine clays ranging from +11.5‰ to

+28.5‰ $\delta^{18}O$ (Savin and Epstein, 1970) and approximately -32‰ to -56‰ δD (Capuano, 1992) constrains the theoretical fluid formation temperature between 50-130ºC (Figure 2.7).

Empirical relationships between cation concentration and temperature have been explored for Mg and Li (Kharaka and Mariner, 1989) and Na and Li (Fouillac and Michard, 1981). The Mg/Li geothermometer is a field-based relationship developed for sedimentary basins where temperature is less than 350ºC (Kharaka and Mariner, 1989). The Na/Li relationship was developed for use in rivers, brines, and geothermal springs where temperature does not exceed 300ºC. Use of these two chemical relationships to further constrain the temperature of fluid yields minimum values between 71°C and 74°C. However, the measured cation concentrations used for these calculations were sampled after mixing and reacting along the fluid flow path (e.g. Mg is consumed in authigenic carbonate minerals at the SMTZ). Thus, the Mg, Na, and Li data indicate the dehydration reactions occurred at temperatures ≥71°C.

Laboratory experiments have shown that alteration of marine sediment releases Li and B at temperatures >50°C (James et al., 2003; Lui-Heung et al., 1994; You et al., 1996). Both B and Li are enriched in sampled pore water at Site 2, and B enrichment is greater than Li. B is desorbed from clay surfaces at increasing temperature and is largely desorbed by approximately 100ºC–150°C (You et al., 1995b; You and Gieskes, 2001); at temperatures >150° Li is preferentially enriched in pore water over B (You et al., 1995a; You and Gieskes, 2001). Hydrothermal experiments with Cascadia Basin sediments and seawater predict that the maximum Li concentration measured in Site 2 pore water (151 μM) should correlate to an upper temperature of approximately 150ºC (James et al., 2003; Wei, 2007). The lack of propane and butane in the pore water at Site 2 supports that temperature of fluid formation is unlikely to have been higher than ~150°C (Table A-1) (Kastner et al., 2014).

Based on these geothermometers, the fluid at Site 2 represents mixing of mineral dehydration fluid that originated at temperatures between 70–150°C. Assuming the geothermal gradient at this distance from the deformation front (~60.1 km landward) is approximately 60°C/km (Phrampus et al., 2017), then fluid feeding this seep may be sourced from up to 2.5 km below the seafloor.

There is also evidence of gas hydrate formation in the shallow sediment section at Site 2. The increase in Ne/Ar and decrease in Kr/Ar and Xe/Ar ratios within the Site 2 samples indicate that methane hydrate may be forming at this location. Indeed, the upper 15 cm of GC5 had a mousse-like texture and the shallowest 7.5 cm of nearly GC4 yielded positive pore water $\delta^{18}O$ and δD values indicative of methane hydrate dissociation during core recovery, further indicating active methane hydrate formation near the seafloor. Based on bottom water temperature and the geothermal gradient, the upper few meters of the sediment column are within the MHSZ. As such, a fraction of the upward advecting methane is sequestered in methane hydrate at this site.

2.5.3 Mixed input at Site 4

Site 4 chloride concentrations are 59% diluted from standard seawater (Cl = 230 mM at 257 cm depth), indicating mixture with at least one fresh fluid source at depth. $\delta^{18}O$ and δD values become lighter with depth in both GC16 and GC17, which, coupled with a decrease in Cl concentration, is indicative of meteoric water (MW) input. However, a 59% dilution of seawater with meteoric water, constrained using the local meteoric water line (LMWL) for groundwater within the nearby Olympic Peninsula Elwha watershed (Sidle and Cvetic, 2011), would produce isotope values that are much more negative than those measured. This suggests that at least one more fresh fluid end-member must be contributing ^{18}O and D to shift the isotope ratios in the positive direction to counterbalance the isotopically light meteoric water. Additionally, B concentrations in the pore water are high with respect to seawater, indicating that there may be clay dehydration at depth, though Li concentrations should also be higher in this scenario.

Given the lack of a clearly distinct admixture of fluid sources, we explore four potential scenarios of mixing that could account for these results. Each scenario utilizes either measured or assumed fractionation factors (Appendix A Table A2) to represent different fluid sources.

Scenario 1: Seawater and Meteoric Water

We applied the average $\delta^{18}O$ value ($\delta^{18}O = 12.7‰$) measured from groundwater springs in the Elwha watershed on the nearby Olympic Peninsula were applied (n=158) (Sidle and Cvetic, 2011) to calculate the fraction of meteoric water required to recreate the measured isotopic values in GC17. Of the springs sampled, 56% were recharged within the last 1,000 years and 13% were recharged more than 5,000 years ago (Sidle and Cvetic, 2011). The calculated fraction of MW necessary to recreate measured $\delta^{18}O$ values in GC17 is no more than 12.5%, yet pore water in the core is diluted 59% from seawater. However, all of the springs sampled were recharged during the Holocene and springs in this high altitude, inland watershed may not be the most reasonable analogue of MW outcropping offshore (Sidle and Cvetic, 2011). MW discharged on the upper continental slope could be relict groundwater from the last glacial maximum. In this scenario, a recharge zone would be closer to the coast on the modern continental shelf, which was sub-aerial during the Pleistocene. The theoretical $\delta^{18}O$ value of precipitation at Forks, WA (47.9022º, -124.624º, 3 m elevation above sea level) is -8.5‰ with a 95% confidence interval of 0.2‰ (Bowen, 2020). Using this coastal value as the MW end-member fluid, the maximum fraction of MW contributing to measured $\delta^{18}O$ in GC 17 is 18.6% (Figure A-2) (see Appendix A for more detail).

There must be another source of fresh water with a more positive isotopic signature contributing to the seep fluid at Site 4. Additionally, the relationship between $\delta^{18}O$ and Cl data for Site 4 cores does not fall on a linear mixing line between these two fluid sources (Figure A-1a). There must be at least one other end-member fluid contributing Cl-depleted water that has heavier ^{18}O than local MW.

Scenario 2: Seawater, Meteoric Water, and Clay Dehydration

The mixture of buried seawater, MW, and clay dehydration would require a 20% contribution of meteoric water and 39% from a deep-sourced fluid with similar composition to the fluid at nearby Site 2 (Figure A-1b). However, the measured pore water geochemical tracers do not exhibit patterns expected from clay dehydration, such as Li enrichment greater than seawater, although B is greatly enriched from background seawater and K decreases with depth, as would be expected from the smectite-illite transition.

Scenario 3: Seawater, Meteoric Water, and Gas Hydrate Dissociation

The mixing of fluids derived from buried seawater, MW input, and gas hydrate dissociation is possible because Site 4 is within the predicted depth range of GHSZ retreat. This scenario would require the same proportions of fluid input as Scenario 2 and hence cannot be distinguished because the $\delta^{18}O$ value of gas hydrate is similar to the $\delta^{18}O$ value used for the clay dehydration based on Site 2 fluid compositions (Figure A-1c).

Scenario 4: Seawater, Clay Dehydration, and Clay Formation

The mixing of buried seawater with advected fluid derived from clay dehydration and clay formation at depth is a qualitatively plausible scenario for fluids feeding the Site 4 seep. Both clay dehydration and clay formation are common processes in sediments of active margins (Kastner et al., 2014). In this scenario, clay dehydration releases water enriched in B and Li and K and Li are consumed by clay formation. However, the data from Site 4 gravity cores does not show enriched Li concentrations with depth and the K profile is not as depleted as would be expected from this process. Little clay formation would be necessary to shift the $\delta^{18}O$ of pore water in the negative direction. This scenario would negate the need for MW input, however we cannot quantify mixing. In the previous scenarios we applied measured Cl and $\delta^{18}O$ values to a series of equations to quantify mixing ratios assuming that both parameters act as conservative tracers of water masses (see Appendix A for detailed information). We cannot reasonably predict what the increased Cl concentration of pore water would be if clay formation was occurring. Therefore, we lack a second conservative parameter to calculate the fraction of clay formation needed to account for measured values.

There is a lack of clear evidence of a deep-sourced fluid similar to Site 2. Scenarios 2 and 3 require groundwater discharge to drive observed fluid freshening, however the authors are not aware of any published observations of groundwater discharge on the upper slope of other mid-latitude margins. While Scenarios 2 through 4 are all plausible, our strongest hypothesis based on the pore water geochemistry is a fluid source mixture of seawater, meteoric water, and gas hydrate dissociation (Scenario 3). The pore water profiles show no large increases in Ca, Li, and Sr, as seen at Site 2, and no evidence of thermogenic gas. The downcore changes in Mg and Li indicate clay formation is indeed occurring at depth, but the system requires an influx of freshwater likely from a discharge of meteoric water. This potential meteoric water could be sourced from modern subterranean groundwater or relict groundwater from the last glacial maximum. Despite our efforts, the evidence gathered remains unequivocal in determining the sources of fluid feeding Site 4 plumes.

2.5.4 Noble gases as potential gas hydrate tracer

We collected water column samples directly above actively venting seeps and measured noble gas ratios and CH_4 concentrations to determine if gas release was predominantly CH_4 and whether this CH_4 was associated with gas hydrates or another reservoir. The relative shift in noble gas ratios compared to atmospheric equilibrium is theoretically a useful tracer, but field-based measurements have been plagued with difficulties (Dickens and Kennedy, 2000; Winckler et al., 2002). The water samples analyzed in this study do not show signs of contamination, and show variations across the sites sampled. Analyses of water collected from Site 2 shows clear evidence of Xe and Kr depletion compared to atmospheric equilibrium, indicating active gas hydrate formation at this site (Figure 2.1). Analyses of all other sites yielded Xe/Ar and Kr/Ar ratios indistinct from background. It is likely that a clear signal of gas hydrate dynamics is lost within the noise of the data at most sites due to mixing with background seawater, except at the site with the strongest upward advection of fluid (Site 2). Pore water $\delta^{18}O$ and δD from Site 2 corroborates this signal of shallow gas hydrate formation, whereas pore water geochemistry from other sites do not convincingly indicate gas hydrate formation or dissociation.

The distinct Xe and Kr values Site 2 highlight the potential that noble gas ratios can be used as another tracer of *in situ* gas hydrate dynamics. This is not the first study to use noble gas ratios to investigate the presence of gas hydrates (Dickens and Kennedy, 2000; Hunt et al., 2013; Winckler et al., 2002), however, this is the first study, to our knowledge, to show that noble gas ratios of Ne, Kr, and Xe in the fluid efflux from marine seep sites can be used as a tracer of gas hydrate dynamics. This geochemical tracer can be improved upon in the future with more direct fluid sampling strategies, for example the use of ROV-assisted gastight sampling (Baumberger et al., 2018).

2.5.5 Potential reasons for lack of geochemical evidence of widespread hydrate dissociation

Gas seepage occurs along the entire WA margin at the predicted upper limit of hydrate stability (Riedel et al., 2018), however, most of the seeps sampled in this study are long-lived features characterized by carbonate pavements or subsurface nodules and chemosynthetic communities, as evidenced by either retrieval of nodules or seep organisms within gravity cores and the inability for some gravity cores to penetrate the sediment. We would expect that active hydrate dissociation in response to modern bottom water warming would produce young, emergent seeps. The pore water geochemistry does not provide clear evidence of gas hydrate dissociation at any of the sites sampled during this study.

Several potential reasons exist for the lack of a geochemical signal of hydrate dissociation at active seep sites. It is possible that the signal of gas hydrate dissociation may be diluted by other fluid sources and is, therefore, undetectable with our methods. For example, pore water Cl dilution through fresh water addition is evident at two seep sites discussed above, but profiles of $\delta^{18}O$ and δD do not trend in the direction expected if hydrate dissociation was the sole cause of pore water freshening. This lack of isotopic signal could possibly be due to dampening of the gas hydrate dissociation signal by other fluid source(s). The signal of hydrate dissociation could have been advected out of the sediments by the time we conducted our sampling survey. Additionally, our sampling plan targeted only actively venting seeps along the 500-m contour, which generated a small sample size that could have biased our results by missing seeps that vent only sporadically.

At background locations or emergent seeps, it is likely that pore water CH_4 concentrations do not reach saturation with respect to methane hydrate at shallow sediment depths that would be impacted by contemporary bottom water warming. This illuminates the discrepancy between the gas hydrate stability zone (GHSZ) and the gas hydrate occurrence zone (GHOZ). The GHOZ is the region within the GHSZ where CH_4 concentrations meet or exceed the necessary threshold to be in saturation with respect to methane hydrate. At long-lived seep sites, the depth of the GHOZ is pushed shallower as the rate of upward advection is greater than the rate of diffusion. This shoaling of the GHOZ and strong upward advection of geochemical tracers of hydrate dissociation may be why the signal of hydrate dissociation was no longer present at the long-lived seep systems we studied.

However, model- and field-based studies suggest that CH_4 commonly does not reach saturation with respect to hydrate shallower than 30–60 mbsf outside of active, longer-lived seep sites on continental margins (Wallmann et al., 2012). Figure 2.8 illustrates a conceptual framework of how a deeper GHOZ would be impacted by modern bottom water warming. Before the onset of bottom water warming (t_0), the GHOZ is buried 30–60 mbsf on a continental margin (Figure 2.8a). After the onset of bottom water warming (t_1), the upper limit of hydrate stability retreats downslope and warming penetrates the upper few meters of sediment but does not impact the deeper GHOZ (Figure 2.8b). Assuming the GHOZ on the upper slope of the WA margin is buried at least 30 mbsf and bottom water warming has only persisted for decades

(Hautala et al., 2014), seeps along the 500-m isobath of the Cascadia margin could not be fueled by shallow hydrate dissociation. Long-lived seeps with shallowly buried hydrates would be impacted by modern bottom water warming; for example, the shallowly buried hydrates at Site 2 will likely be pushed out of the GHSZ in the coming decades if warming continues. Decades from now, as bottom water warming continues (t_2), the upper limit of the GHSZ will retreat further downslope (Figure 2.8c). Heat from a century or more of continued bottom water warming will propagate deeper into the sediment column over time and begin to impact gas hydrate in the GHOZ. It is important to remember, however, that these upper slope hydrates account for a very small portion of the global hydrate reservoir (Ruppel, 2011).

In this conceptual framework, the threat of hydrate dissociation due to prolonged bottom water warming is a real issue decades from now. However, the amount of CH_4 that reaches the water column from hydrate dissociation will likely be small due to the anaerobic oxidation of methane in the sediment column (e.g. Regnier et al., 2011). The main impact of hydrate dissociation may be the loss of the permeability barrier it provides, thus allowing passive CH_4 emissions to the seafloor (Thatcher et al., 2013; You et al., 2019).

2.5.6 Heterogeneity of seep fluid sources at the upper slope

There is widespread venting of fluids along the WA margin, with various fluid sources and ratios of fluid mixing. Deeply-sourced fluid was found to be contributing to surface fluid and gas expulsion at Site 2 and possibly Site 4. The patterns in Li and B concentrations in Site 2 gravity cores align with what we expect to see from clay dehydration at depth. Indeed, it is common practice within the marine geochemistry community to use Li and B as tracers of high-temperature, deep-sourced fluids because Li and B are both desorbed from clay surfaces as temperature increases. Pore water Li and B concentrations seen in Site 4 gravity cores demonstrates the risk of using only one of these two elements as indicators of deep-sourced fluid. In Site 4 cores, Li remains at approximately seawater value with depth while B concentrations increase more than 18 times greater than seawater. The interpretation of clay dehydration at depth should be based on enrichments in both elements, not just one. This difference in pore water enrichment suggests a different mechanism for pore water B enrichment at Site 4 than at Site 2.

The diversity of fluid sources along the margin is especially apparent when comparing fresh fluid end-member values of Li and B at Sites 2, 4, and 6 to end-member values at two better known Cascadia margin cold seeps: Bullseye Vent offshore Vancouver Island (IODP Expedition 311, Site U1328) and the summit of Southern Hydrate Ridge offshore central Oregon (Figure A-3) (Tréhu et al., 2003). These latter two locations are located on the mid-slope of the Cascadia margin, as opposed to the upper slope sites sampled in this study. The end-member fluid composition illustrates the significant B enrichment in fluids venting at Sites 2 and 4 as well as the substantial Li component at Site 2.

Pore water chemistry collected from Site 4 gravity cores is likely a mixture of multiple fluid sources at depth. Our efforts to define these fluid sources and their percent contribution to the fluid efflux yielded little conclusion to multiple potential mixing scenarios. Two of the posited scenarios require some volume of meteoric water input to drive pore water freshening and push both $\delta^{18}O$ and δD in the negative direction, yet we are unaware of other observations of meteoric groundwater discharge this far downslope on an active continental margin.

Pore water geochemistry from Site 2 showed the most obvious markers of high temperature fluid-rock interaction. This mineral dehydration fluid is derived from ≤2.5 km below the seafloor based on the chemical geothermometers and regional geothermal gradients discussed above. There is 3.0 km of accreted sediment in this region of the margin. Therefore, these mineral dehydration reactions are occurring within the wedge and not within the underthrust sediments (Phrampus et al., 2017). It is possible that the observation of deeply-sourced clay dehydration along the upper slope is due to continued thickening of the accretionary wedge on the WA sector of the margin. The Juan de Fuca plate is a young tectonic plate close to the North American continent. High sedimentation out to the spreading center insulates the young plate and the thickening of the sediment column buries the warm down-going plate with cold sediments at thermal equilibrium with overlying bottom water. This burial reduces the geothermal gradient near the surface and clay minerals in the majority of the sediment column remain outside the lower thermal boundary of clay dehydration. Continued accretion of sediments during ongoing subduction drives thickening of wedge sediments, however the geothermal gradient in the upper sediment column is set by the temperature of cold bottom water and not the residual heat of the Juan de Fuca plate. Only with continued accretion and thickening of the wedge are these colder sediments buried to a depth where temperatures are high enough to begin the dehydration of smectite to illite clay. This would happen fairly late in subduction only when the wedge is thick enough to push these sediments to a warmer geothermal regime, so that pore fluid production occurs in sediments that are already compacted and pore fluid pressure increases.

This proposed mechanism is similar to the results of the Hyndman et al., (1993) study of the effects of sediment thickening and fluid expulsion on the thermal regime of the northernmost Cascadia accretionary prism offshore Vancouver Island. The results of this investigation suggest that rapid thickening of the accretionary prism yields a drastically under-consolidated and highly porous sediment section driven by rapid, tectonically-induced horizontal shortening and vertical thickening of the section. Reconsolidation of the accreted material occurs slowly over time so that peak pore fluid pressure and fluid expulsion occurs much more landward of the deformation front when the sediment section is in the mid-slope region (Hyndman et al., 1993). We suggest that similar late-stage porosity reduction and fluid expulsion could be occurring on the upper slope of the WA sector of the Cascadia margin driven by rapid thickening of the accretionary wedge.

This mechanism, however, does not explain observations of the majority of seeps studied where fluid is escaping from shallow depths. These areas of shallowly sourced fluid expulsion indicate that there must be pockets of shallow, localized overpressure along the margin that increases pore fluid pressure and leads to the expulsion of shallow, minimally altered pore fluid. In the absence of geophysical data, we can only hypothesize what may drive this localized shallow overpressure. One potential explanation to describe this scenario once again finds its source in continued rapid thickening of the wedge. Hyndman et al., (1993) modeled the thermal effects of sediment thickening and fluid expulsion in the northern Cascadia accretionary prism offshore Vancouver Island, Canada. The results of their investigation suggest that rapid thickening of the accretionary prism yields a drastically under-consolidated and highly porous sediment section driven by rapid horizontal shortening and vertical thickening of the sediment column. Reconsolidation of the accreted material occurs slowly over time so the peak pore fluid pressure and fluid expulsion occurs much more landward of the deformation front when the sediment section is in the mid-slope or even upper slope region (Hyndman et al., 1993). It is possible that a similar late-stage porosity reduction and fluid expulsion could be occurring on the upper slope of the WA sector of the Cascadia margin driven by rapid thickening of the accretionary wedge.

2.6 Conclusion

The results of this study yield no geochemical evidence for widespread contemporary methane hydrate dissociation hypothesized as a result of modern bottom water warming. All seeps sampled are long-lived and emitted fluids are fed from a variety of sources and migration is likely controlled by local margin structure. A unique observation from this study is the potential for meteoric water output on the upper slope of an active margin: we are not yet aware of such an observation along the upper slope of an active margin.

To explain the lack of geochemical evidence of gas hydrate dissociation fueling fluid discharge from the upper slope, we invoked a conceptual framework distinguishing the thermodynamically-defined GHSZ from the GHOZ, which is defined as the region where pressure, temperature, and pore water CH_4 concentration are conducive to hydrate formation. It is important to remember gas hydrate occurrence will only manifest in marine sediments when all three parameters are met. On the WA sector of the Cascadia margin, it is likely that the GHOZ is several tens of meters below the seafloor and, therefore, the threat of prolonged modern bottom water warming will likely only be an issue in the latter half of the 21st century.

Finally, in this study we field-tested the practicality of analyzing noble gas ratios in vented fluid as a tracer of subsurface gas hydrate dissociation and showed our results to be in good agreement with the pore water geochemical data. This geochemical tracer can be further improved upon in future field-based studies by utilizing more direct fluid sampling strategies, such as ROV-assisted gastight sampling.

2.7. References

Barrer, R.M., Edge, A.V.J., 1967. Selective Clathration during the Formation of Gas Hydrates. Sep. Sci. 2, 145–154.

Baumberger, T., Embley, R.W., Merle, S.G., Lilley, M.D., Raineault, N.A., Lupton, J.E., 2018. Mantle-Derived Helium and Multiple Methane Sources in Gas Bubbles of Cold Seeps Along the Cascadia Continental Margin. Geochemistry, Geophys. Geosystems 19, 4476–4486. https://doi.org/10.1029/2018GC007859

Berndt, C., Feseker, T., Treude, T., Krastel, S., Liebetrau, V., Niemann, H., Bertics, V.J., Dumke, I., Dünnbier, K., Ferré, B., Graves, C., Gross, F., Hissmann, K., Hühnerbach, V., Krause, S., Lieser, K., Schauer, J., Steinle, L., 2014. Temporal Constraints on Hydrate-Controlled Methane Seepage off Svalbard. Science (80-.). 343, 284–287. https://doi.org/10.1126/science.1246298

Berner, R.A., 1980. Early diagenesis: A theoretical approach: Princeton, New Jersey, Princeton Universtiy Press, 241 p.

Biastoch, A., Treude, T., Rpke, L.H., Riebesell, U., Roth, C., Burwicz, E.B., Park, W., Latif, M., Böning, C.W., Madec, G., Wallmann, K., 2011. Rising Arctic Ocean temperatures cause gas hydrate destabilization and ocean acidification. Geophys. Res. Lett. 38, 1–5. https://doi.org/10.1029/2011GL047222

Boswell, R., Collett, T.S., 2011. Current perspectives on gas hydrate resources. Energy Environ. Sci. 4, 1206. https://doi.org/10.1039/c0ee00203h

Bowen, G.J. and Revenaugh, J. (2003) Interpolating the isotopic composition of modern meteoric precipitation. *Water Resources Research* **39**(10): 1299. doi:10/129/2003WR002086.

Bowen, G.J. (2020) The Online Isotopes in Precipitation Calculator, version 3.1. http://www.waterisotopes.org

Capuano, R.M., 1992. The temperature dependence of hydrogen isotope fractionation between clay minerals and water: evidence from a geopressurized system. Geochim. Cosmochim. Acta 56, 2547–2554.

Claypool, G.E., Kaplan, I.R., 1974. The Origin and Distribution of Methane in Marine Sediments. Nat. Gases Mar. Sediments 99–139.

Dickens, G.R., Castillo, M.M., Walker, J.C.G., 1997. A Blast of Gas in the Latest Paleocene. Geology 25, 259–262.

Dickens, G.R., Kennedy, B.M., 2000. Noble Gases in Methane Hydrate From the Blake Ridge. Proc. Ocean Drill. Program, Sci. Results 164, 165–170.

Fouillac, C., Michard, G., 1981. Sodium/lithium ratio in water applied to geothermometry of geothermal reservoirs. Geothermics 10, 55–70. https://doi.org/10.1016/0375-6505(81)90025-0

Hautala, S.L., Solomon, E.A., Johnson, H.P., Harris, R.N., Miller, U.K., 2014. Dissociation of Cascadia margin gas hydrates in response to contemporary ocean warming. Geophys. Res. Lett. 41, 799–804. https://doi.org/10.1002/2013GL058954.Received

Hensen, C., Wallmann, K., Schmidt, M., Ranero, C.R., Suess, E., 2004. Fluid expulsion related to mud extrusion off Costa Rica - A window to the subducting slab. Geology 32, 201–204. https://doi.org/10.1130/G20119.1

Hunt, A.G., Stern, L., Pohlman, J.W., Ruppel, C., Moscati, R.J., Landis, G.P., 2013. Mass fractionation of noble gases in synthetic methane hydrate: Implications for naturally occurring gas hydrate dissociation. Chem. Geol. 339, 242–250. https://doi.org/10.1016/j.chemgeo.2012.09.033

Hyndman, R.D., Wang, K., Yuan, T., Spence, G.D., 1993. Tectonic Sediment Thickening, Fluid Expulsion, and the Thermal Regime of Subduction Zone Accretionary Prisms: The Cascadia Margin off Vancouver Island. J. Geophys. Res. 98, 21865–21876. https://doi.org/10.1029/93JB02391

IAEA/WMO (2015). Global Network of Isotopes in Precipitation. The GNIP Database. Accessible at: https://nucleus.iaea.org/wiser.

James, R.H., Allen, D.E., Seyfried, J.W.E., 2003. An experimental study of alteration of oceanic crust and terrigenous sediments at moderate temperatures (51 to 350??C): Insights as to chemical processes in near-shore ridge-flank hydrothermal systems. Geochim. Cosmochim. Acta 67, 681–691. https://doi.org/10.1016/S0016-7037(02)01113-4

Johnson, H.P., Miller, U.K., Salmi, M.S., Solomon, E.A., 2015. Analysis of bubble plume distributions to evaluate methane hydrate decomposition on the continental slope. Geochemistry Geophys. Geosystems 1541–1576. https://doi.org/10.1002/2014GC005684.Key

Kastner, M., Elderfield, H., Martin, J.B., 1991. Fluids in convergent margins: what do we know about their composition, origin, role in diagenesis and importance for oceanic chemical fluxes? Philos. Trans. R. Soc. London 335, 243–259.

Kastner, M., Solomon, E.A., Harris, R.N., Torres, M.E., 2014. Fluid Origins, Thermal Regimes, and Fluid and Solute Fluxes in the Forearc of Subduction Zones, in: Developments in Marine Geology. pp. 671–733.

Kennett, J.P., Cannariato, K.G., Hendy, I.L., Gehl, R.J., 2003. Methane hydrates in Quaternary climate change, in: Methane Hydrates in Quaternary Climate Change. American Geophysical Union, pp. 1–9.

Kharaka, Y.K., Mariner, R.H., 1989. Chemical Geothermometers and Their Application to Formation Waters from Sedimentary Basins, in: Naeser, N.D., McCulloh, T.H. (Eds.), Thermal History of Sedimentary Basins: Methods and Case Histories. Springer-Verlag, pp. 99–117.

Leonte, M., Kessler, J.D., Kellermann, M.Y., Arrington, E.C., Valentine, D.L., Sylva, S.P., 2017. Rapid rates of aerobic methane oxidation at the feather edge of gas hydrate stability in the waters of Hudson Canyon, US Atlantic Margin. Geochim. Cosmochim. Acta 204, 375–387. https://doi.org/10.1016/j.gca.2017.01.009

Lui-Heung, C., Gieskes, J.M., Chen-Feng, Y., Edmond, J.M., 1994. Lithium isotope geochemistry of sediments and hydrothermal fluids of the Guaymas Basin, Gulf of California. Geochim. Cosmochim. Acta 58, 4443–4454. https://doi.org/10.1016/0016-7037(94)90346-8

Maekawa, T. and Imani, N., 2000. Hydrogen and oxygen isotope fractionation in water during gas hydrate formation. Annals of the New York Academy of Sciences 912, 452-459. https://doi.org/10.1111/j.1749-6632.2000.tb06800

Phrampus, B.J., Harris, R.N., Trehu, A.M., 2017. Heat flow bounds over the Cascadia margin derived from bottom simulating reflectors and implications for thermal models of subduction. Geochemistry, Geophysics, Geosystems 18, 3309–3326. https://doi.org/10.1002/2017GC007077

Piñero, E., Marquardt, M., Hensen, C., Haeckel, M., Wallmann, K., 2013. Estimation of the global inventory of methane hydrates in marine sediments using transfer functions.

Biogeosciences 10, 959–975. https://doi.org/10.5194/bg-10-959-2013

Pohlman, J.W., Kaneko, M., Heuer, V.B., Coffin, R.B., Whiticar, M., 2009. Methane sources and production in the northern Cascadia margin gas hydrate system. Earth Planet. Sci. Lett. 287, 504–512. https://doi.org/10.1016/j.epsl.2009.08.037

Pytte, A.M., Reynolds, R.C., 1989. The Thermal Transformation of Smectite to Illite, in: Naeser, N.D., McCulloh, T.H. (Eds.), Thermal History of Sedimentary Basins: Methods and Case Histories. Springer-Verlag, pp. 133–140.

Reagan, M.T., Moridis, G.J., Elliott, S.M., Maltrud, M., 2011. Contribution of oceanic gas hydrate dissociation to the formation of Arctic Ocean methane plumes. J. Geophys. Res. Ocean. 116, 1–11. https://doi.org/10.1029/2011JC007189

Regnier, P., Dale, A.W., Arndt, S., LaRowe, D.E., Mogollón, J., Van Cappellen, P., 2011. Quantitative analysis of anaerobic oxidation of methane (AOM) in marine sediments: A modeling perspective. Earth-Science Reviews 106, 105-130. https://doi.org/10.1016/j.earscirev.2011.01.002

Expedition 311 Scientists, 2006. Site U1328. *In* Riedel, M., Collett, T.S., Malone, M.J., and the Expedition 311 Scientists, *Proc. IODP,* 311: Washington, DC (Integrated Ocean Drilling Program Management International, Inc.). doi:10.2204/iodp.proc.311.106.2006

Ruppel, C., Kessler, J.D., 2017. The Interaction of Climate Change and Methane Hydrates. Rev. Geophys. 55, 1–43. https://doi.org/10.1002/2016RG000534

Ruppel, C.D., 2011. Methane Hydrate and Contemporary Climate Change. Nat. Educ. Knowl. 3, 1–7.

Savin, S.M., Epstein, S., 1970. The oxygen and hydrogen isotope geochemistry of ocean sediments and shales. Geochim. Cosmochim. Acta 34, 43–63. https://doi.org/10.1016/0016-7037(70)90150-x

Sheppard, S.M.F., Gilg, H.A., 1996. Stable isotope geochemistry of clay minerals. Clay Miner. 31, 1–24.

Shipboard Scientific Party, 2003. Site 1249. *In* Tréhu, A.M., Bohrmann, G., Rack, F.R., Torres, M.E., et al., *Proc ODP, Init. Repts.*, 204: College Station, TX (Ocean Drilling Program), 1-98. doi:10.2973/odp.proc.ir.204.108.2003

Skarke, A., Ruppel, C., Kodis, M., Brothers, D., Lobecker, E., 2014. Widespread methane leakage from the sea floor on the northern US Atlantic margin. Nat. Geosci. 7, 1–5. https://doi.org/10.1038/ngeo2232

Thatcher, K.E., Westbrook, G.K., Sarkar, S., Minshull, T. a., 2013. Methane release from warming-induced hydrate dissociation in the West Svalbard continental margin: Timing, rates, and geological controls. J. Geophys. Res. Solid Earth 118, 22–38. https://doi.org/10.1029/2012JB009605

Tréhu, A.M., Bohrmann, G., Rack, F.R., Torres, M.E., et al., 2003. *Proceedings of the Ocean Drilling Program, Initial reports* Volume 204.

Wallmann, K., Pinero, E., Burwicz, E., Haeckel, M., Hensen, C., Dale, A., Ruepke, L., 2012. The global inventory of methane hydrate in marine sediments: A theoretical approach. Energies 5, 2449–2498. https://doi.org/10.3390/en5072449

Wallmann, K., Riedel, M., Hong, W.L., Patton, H., Hubbard, A., Pape, T., Hsu, C.W., Schmidt, C., Johnson, J.E., Torres, M.E., Andreassen, K., Berndt, C., Bohrmann, G., 2018. Gas hydrate dissociation off Svalbard induced by isostatic rebound rather than global warming. Nat. Commun. 9. https://doi.org/10.1038/s41467-017-02550-9

Wei, W., 2007. Fluid Origins, Paths, and Fluid-Rock Reactions at Convertgent Margins, Using

Halogens, Cl Stable Isotopes, and Alkali Metals as Geochemical Tracers. University of Califronia, San Diego.

Weinstein, A., Navarrete, L., Ruppel, C., Weber, T.C., Leonte, M., Kellermann, M.Y., Arrington, E.C., Valentine, D.L., Scranton, M.I., Kessler, J.D., 2016. Determining the flux of methane into Hudson Canyon at the edge of methane clathrate hydrate stability. Geochemistry, Geophys. Geosystems 17, 3882–3892. https://doi.org/10.1002/2014GC005514.

Westbrook, G.K., Thatcher, K.E., Rohling, E.J., Piotrowski, A.M., Pälike, H., Osborne, A.H., Nisbet, E.G., Minshull, T. a., Lanoisellé, M., James, R.H., Hühnerbach, V., Green, D., Fisher, R.E., Crocker, A.J., Chabert, A., Bolton, C., Beszczynska-Möller, A., Berndt, C., Aquilina, A., 2009. Escape of methane gas from the seabed along the West Spitsbergen continental margin. Geophys. Res. Lett. 36, 1–5. https://doi.org/10.1029/2009GL039191

Winckler, G., Aeschbach-hertig, W., Holocher, J., Kipfer, R., Levin, I., Poss, C., Rehder, G., Suess, E., Schlosser, P., 2002. Noble gases and radiocarbon in natural gas hydrates. Geophys. Res. Lett. 29, 1–4. https://doi.org/http://dx.doi.org/10.1029/2001GL014013; doi:10.1029/2001GL014013

Yeh, H.-W., 1980. D H Ratios and late-stage dehydration of shales during burial. Geochim. Cosmochim. Acta 44, 341–352. https://doi.org/10.1016/0016-7037(80)90142-8

You, C.F., Castillo, P.R., Gieskes, J.M., Chan, L.H., Spivack, A.J., 1996. Trace element behavior in hydrothermal experiments: Implications for fluid processes at shallow depths in subduction zones. Earth Planet. Sci. Lett. 140, 41–52. https://doi.org/10.1016/0012-821X(96)00049-0

You, C.F., Chan, L.H., Spivack, A.J., Gieskes, J.M., 1995a. Lithium, boron, and their isotopes in sediments and pore waters of Ocean Drilling Program site 808, Nankai Trough: implications for fluid expulsion in accretionary prisms. Geology 23, 37–40. https://doi.org/10.1130/0091-7613(1995)023<0037:LBATII>2.3.CO;2

You, C.F., Gieskes, J.M., 2001. Hydrothermal alteration of hemi-pelagic sediments: Experimental evaluation of geochemical processes in shallow subduction zones. Appl. Geochemistry 16, 1055–1066. https://doi.org/10.1016/S0883-2927(01)00024-5

You, C.F., Spivack, A.J., Gieskes, J.M., Rosenbauer, R., Bischoff, J.L., 1995b. Experimental study of boron geochemistry: implications for fluid processes in subduction zones. Geochim. Cosmochim. Acta 59, 2435–2442. https://doi.org/10.1016/0016-7037(95)00137-9

You, K., Flemings, P.B., Malinverno, A., Collett, T.S., Darnell, K., 2019. Mechanisms of Methane Hydrate Formation in Geological Systems. Rev. Geophys. 57, 1146–1196. https://doi.org/10.1029/2018RG000638

Zachos, J.C., Dickens, G.R., Zeebe, R.E., 2008. An early Cenozoic perspective on greenhouse warming and carbon-cycle dynamics. Nature 451, 279–283. https://doi.org/10.1038/nature06588

Zatsepina, O.Y., Buffett, B.A., 1998. Thermodynamic conditions for the stability of gas hydrate in the seafloor. J. Geophys. Res. Solid Earth 103, 24127–24139. https://doi.org/10.1029/98jb02137

Acknowledgments:
We graciously thank the Captain and crew of the R/V *Thompson* during cruise TN314 in October 2014; we thank Rob Harris, H. Paul Johnson, and all other science crew who helped during the TN314 cruise. We additionally thank Steven Emerson and Mark Haught for their help and support with noble gas sampling and analyses. This project was supported by U.S. Department of Energy Award DE-FE0013998 to E.A.S and the University of Washington School of Oceanography that provided financial assistance to T.L.W.

2.8 Figures and Tables

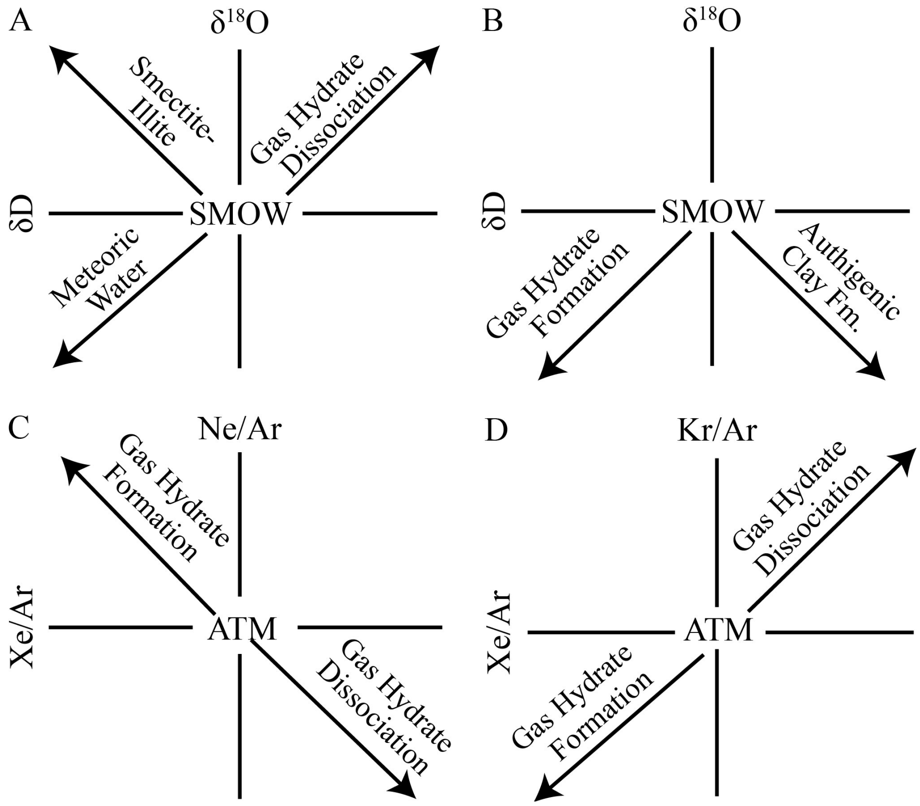

Figure 2.1. Schematic diagrams of expected pore water trends in $\delta^{18}O$ and δD with respect to Vienna standard mean ocean water (VSMOW) when chloride concentrations decrease (A) and increase (B). Pore water noble gas ratios will also change with respect to seawater in equilibrium with atmospheric (ATM) values. Ne/Ar ratios increase and Xe/Ar ratios decrease with respect to ATM during gas hydrate formation (C), and the opposite trend is true during gas hydrate dissociation. The Kr/Ar ratio of pore water also increases with respect to ATM during gas hydrate dissociation (D).

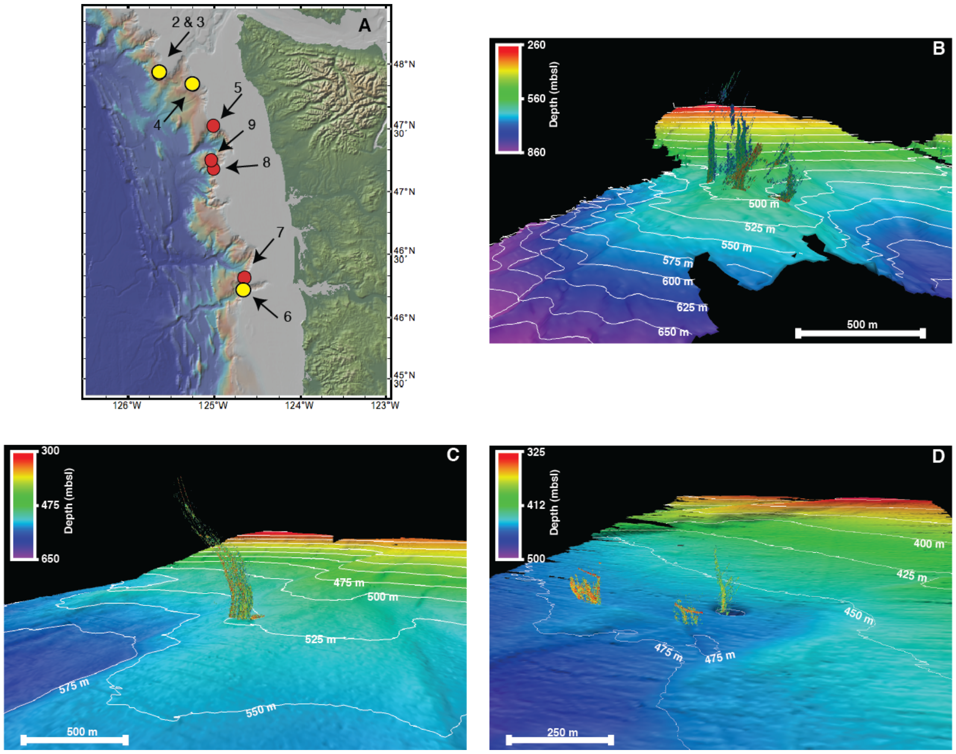

Figure 2.2. (A) The WA margin is located in the northern portion of the Cascadia margin, northeastern Pacific (inset). Eight actively venting seep sites were discovered between depths of 470 and 520 meters below seafloor (mbsl) using multi-beam sonar. This paper focuses on Sites 2, 4, and 6 highlighted with yellow circles. Site 6 at Astoria Canyon (B) was the southernmost site where plumes were detected; Sites 2 (C) and 4 (D) are located at the northern portion of the margin. All plume images are vertically exaggerated 2x.

Table 2.1. Locations and water depth for each core discussed in this study.

Site	Core	Core Length (cm)	Latitude	Longitude	Water Depth (m)
2	GC4	170	47.9299	-125.6406	521
2	GC5	105	47.92961	-125.64022	519
4	GC16	178	47.84547	-125.24331	488
4	GC17	262	47.8455	-125.24335	489
6	GC31	215	46.22261	-124.65494	489

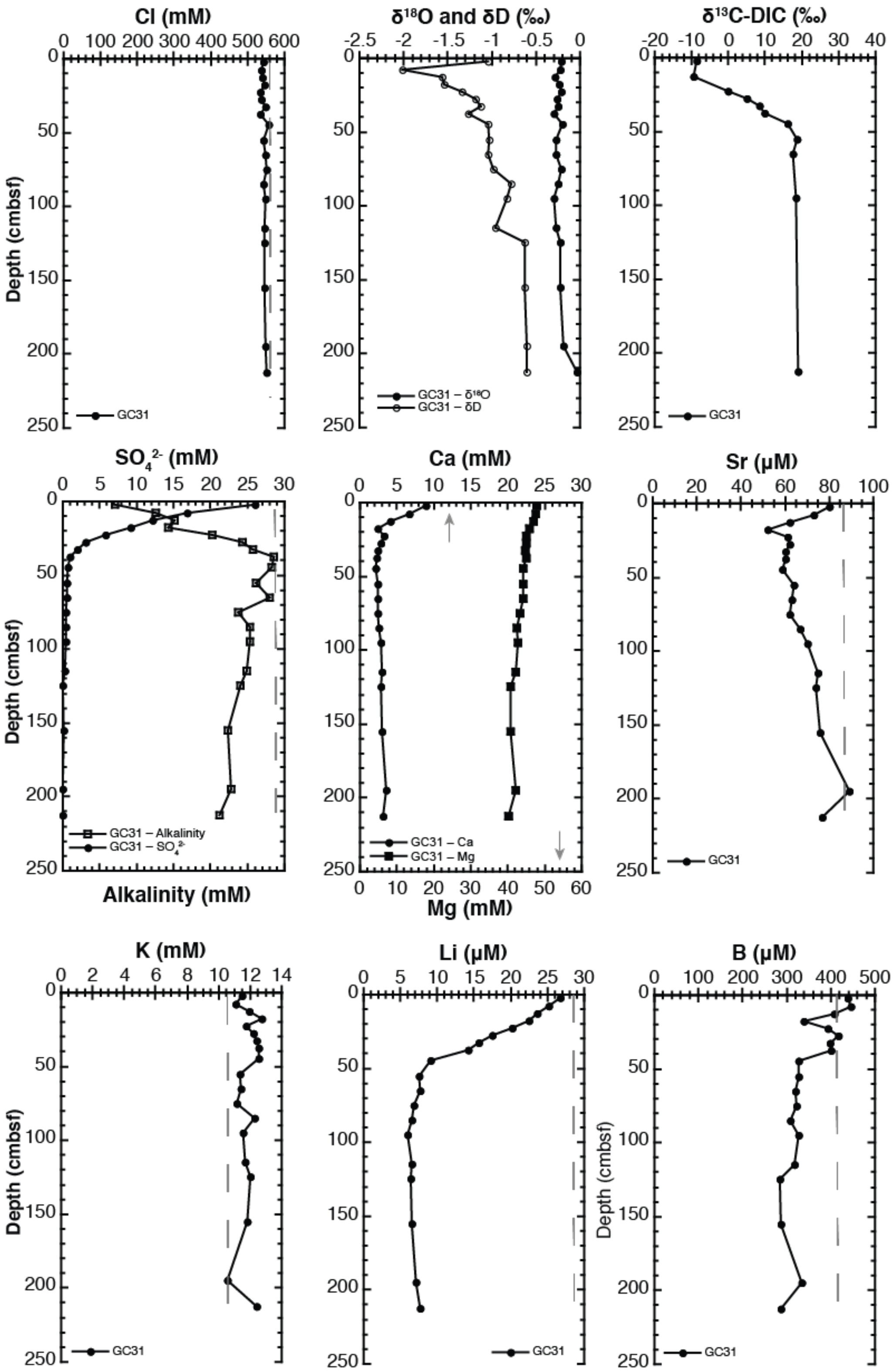

Figure 2.3. Pore water geochemical profiles for GC31, Site 6. Dashed lines and arrows indicate typical seawater values.

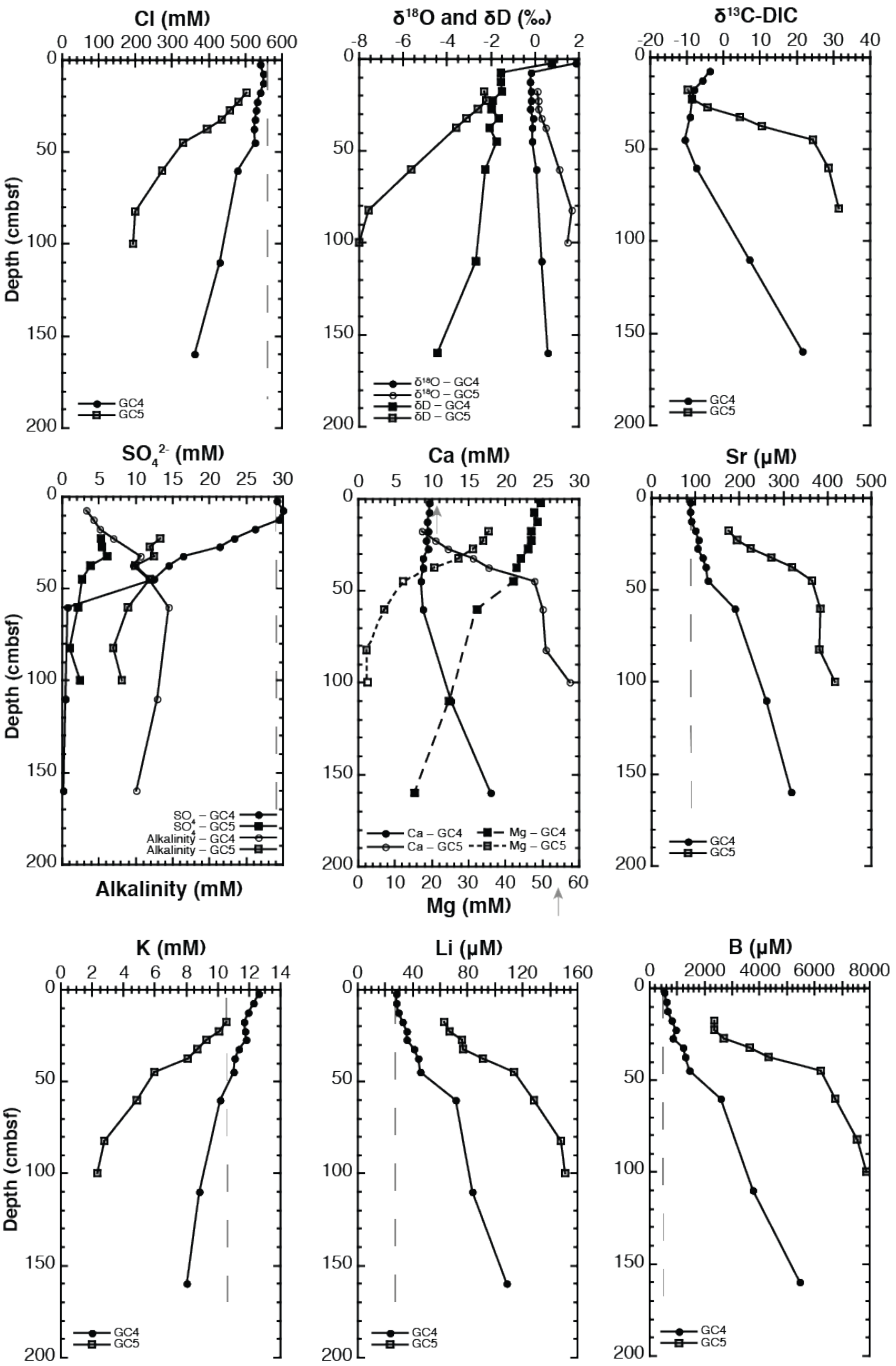

Figure 2.4. Pore water geochemical profiles for GC4 and GC5, Site 2. Gray dashed lines and arrows indicate typical seawater values.

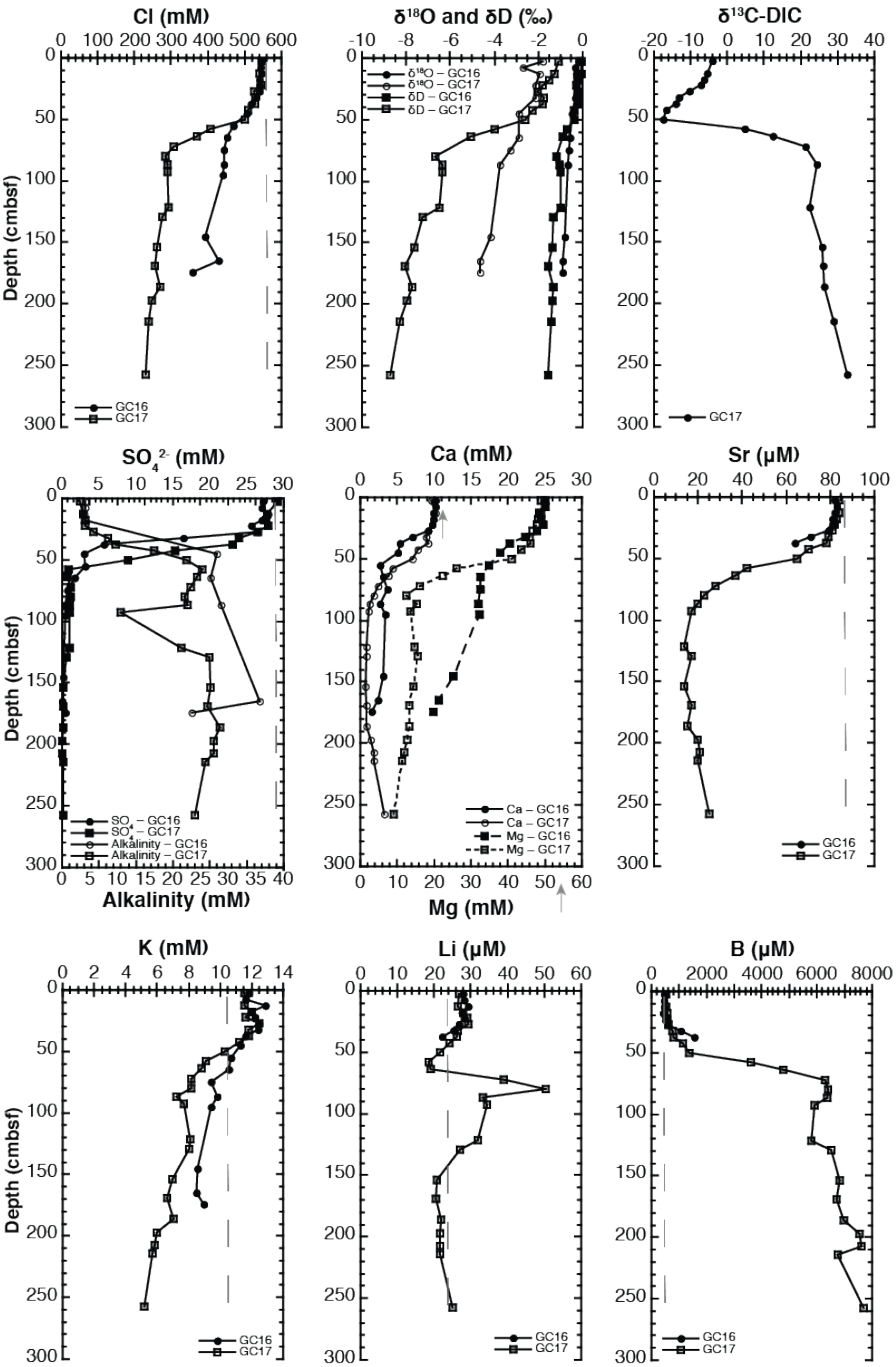

Figure 2.5. Pore water geochemical profiles for GC16 and GC17, Site 4. Gray dashed lines and arrows indicate typical seawater values.

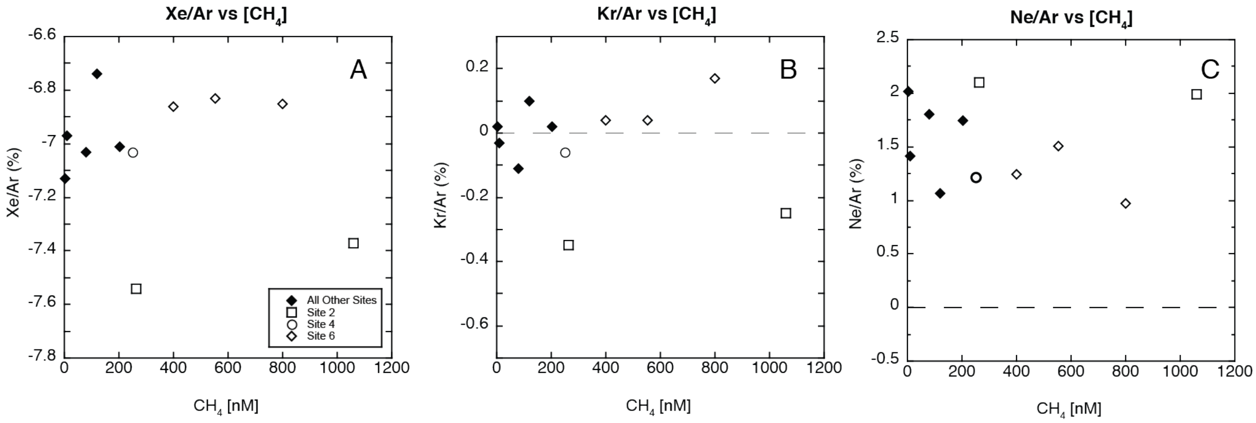

Figure 2.6. Plotted noble gas ratios represent the percent *in situ* saturation of Xe/Ar, Kr/Ar, and Ne/Ar. The dashed lines at 0% saturation indicate *in situ* equilibrium with atmospheric noble gas ratios. The 0% saturation line has been removed from (A) to enhance data visualization. Site 2 samples are plotted as open squares, open circles represent Site 4, and open diamonds designate Site 6 samples. Filled diamonds represent all other sites sampled.

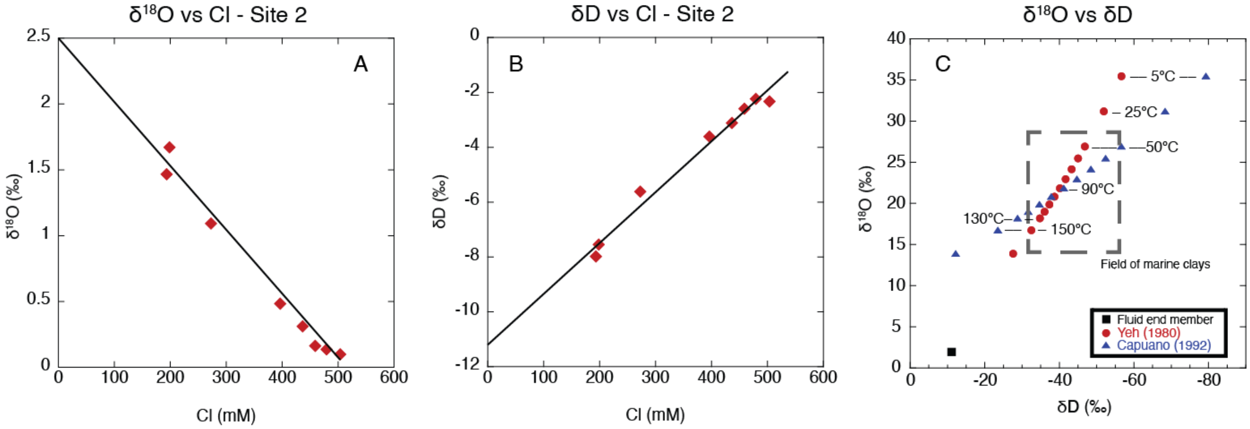

Figure 2.7. Plots of (A) Cl vs. $\delta^{18}O$ and (B) Cl vs δD in pore water from GC5, Site 2. Extrapolation of data trend to fresh end-member yields an estimation of the isotopic composition of the original dehydration fluid. These dehydration fluid values were then used to calculate the theoretical temperatures of fluid formation assuming equilibrium fractionation between the pore water and clay minerals (after Hensen et al., 2004). Theoretical isotope values of clays were calculated after Sheppard and Gilg (1996), Yeh (1980) (red circles), and Capuano (1992) (blue triangles). Gray arrows indicate the difference between the fresh fluid end-member and the calculated values.

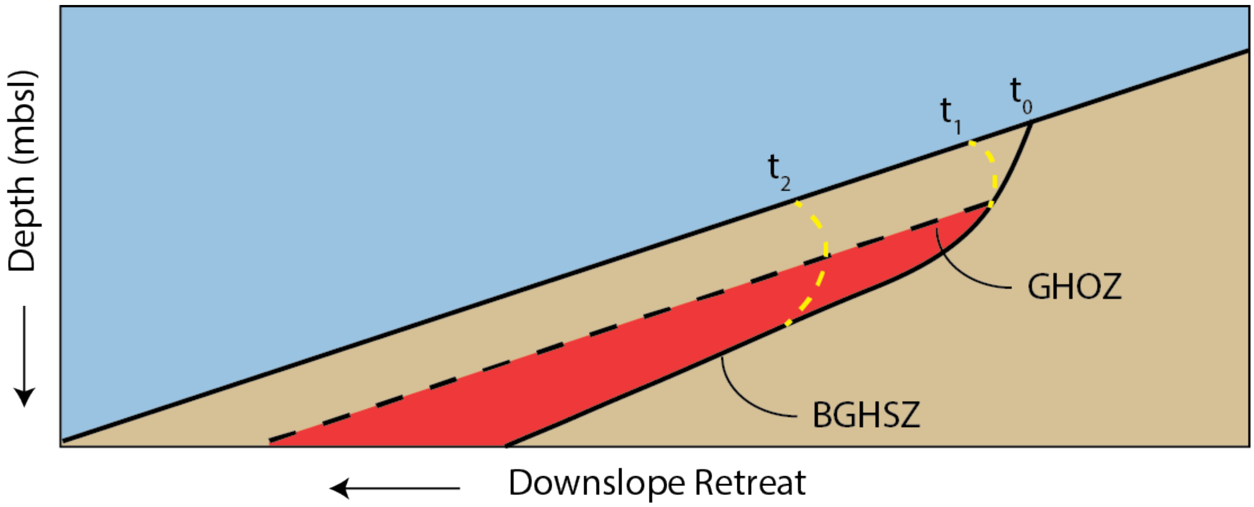

Figure 2.8. Conceptual schematic of the change in gas hydrate stability zone (GHSZ) depth and impact of continued bottom water warming on the gas hydrate occurrence zone (GHOZ) with time. The GHSZ encompasses the volume of sediment above the base of the GHSZ (BGHSZ). Gas hydrates are buried approximately 30 m below seafloor in the area highlighted in red. The GHSZ outcrops at the sediment/water interface on the upper slope at t_0. The heat from continued bottom water warming propagates further into the sediment over decades and leads to the downslope retreat of the upper limit of hydrate stability (t_1). This warming still does not propagate deeply enough to encounter the GHOZ, thus methane hydrates remain insulated from warming. The GHOZ will only be impacted if warming continues for decades to centuries longer (t_2).

Chapter 3.

Biogeochemical implications of persistent downward flow of seawater beneath *Beggiatoa* mat communities at cold seeps

Abstract

Subseafloor biogeochemical reactions in cold seep environments have a profound impact on benthic biological communities and chemical exchange with the ocean. Conventional wisdom dictates that chemosynthetic seep organisms depend on the upward flux of reduced fluid to drive metabolism and growth yet expansive benthic communities have been observed in regions where net fluid flow is downward into the sediment. To further study this phenomenon, continuous measurements of fluid flow rate and time-series depth profiles of pore fluid chemistry were made across a *Beggiatoa* bacterial mat community at Hydrate Ridge using two types of fluid flow meters from 2013–2018. This time-series data shows that seafloor bacterial mats persist in a highly variable flow regime and thrive in areas of both downward and upward flow of seawater. This shallow circulation of seawater drives enhanced rates of microbial reactions across seep sites and increases the consumption of O_2, NO_3^-, SO_4^{2-}, and Ca^{2+} and the production of alkalinity, thus amplifying the role of seeps in marine biogeochemical cycles.

3.1 Introduction

Anoxic continental margin sediments host large reservoirs of methane (CH_4) as dissolved gas, free gas, or solid gas hydrate (Wallmann et al., 2012; Boetius & Wenzhöfer, 2013). Faulting and overpressure driven by tectonic forcing and rapid sediment accumulation are among a host of mechanisms that create pathways for CH_4 to rise toward the sediment-water interface and enter the water column. These areas of seepage, termed "cold seeps", are defined by low temperature and high concentrations of reduced gases such as CH_4 and bisulfide (HS^-). These systems are found along all continental margins and are locations where subseafloor biogeochemical reactions have a profound impact on benthic communities and chemical exchange with seawater. A key subsurface reaction of global importance is the anaerobic oxidation of methane (AOM) whereby a consortium of bacteria and archaea syntrophically oxidize CH_4 and reduce sulfate (SO_4^{2-}) to fuel metabolic processes (Equation 3.1):

$$CH_4 + SO_4^{2-} \rightarrow HCO_3^- + HS^- + H_2O \qquad \text{(Eqn. 3.1)}$$

The bisulfide produced through AOM is a critical nutrient for overlying macro- and microorganisms. Thiotrophic bacteria, chemoautotrophic vesicomyid clams, solemyid bivalves, and polychaete tube worms are examples of endemic cold seep organisms (Sahling et al., 2002), each requiring reduced sulfur for survival. Although vesicomyid clams and solemyid bivalves are capable of digging into marine sediment in order to acquire reduced sulfur for their metabolisms, small filamentous bacteria such as *Beggiatoa*, ubiquitous at cold seeps worldwide, are incapable of digging for sulfur (Hensen et al., 2006) and must rely on the upward diffusion or advection of this reactant. *Beggiatoa* therefore tend to colonize areas of high upward flux of sulfide from cold seep sediments (Suess, 2014; Sahling et al., 2002) where the HS^-/O_2 interface exists within the uppermost few millimeters of the sediment. Indeed, presence of filamentous thiotrophic bacteria such as *Beggiatoa* are often used as visual indicators of cold seep systems, and at least one study has tested whether the presence or absence of typical seep organisms can be used as visual proxies to estimate fluid flow rates at seep and non-seep settings (Tryon et al., 2002).

Given that cold seeps are known for upward advection of fluid and gas, and that *Beggiatoa* communities are ubiquitous at cold seeps and require high gradients of HS^- and O_2 for survival, it is often assumed that these bacteria require the upward advection of HS-rich fluid in order to survive. Our understanding of seep-related fluid regimes is largely based on temporal snapshots from shallow sediment core pore water solute profiles, short-term (~30-day) benthic fluid flux meter deployments, or shallow temperature profiles (e.g. Torres et al., 2002; Tryon et al., 2002; Henry et al., 1992), and long-term fluid flow variability is largely unknown. It is this long-term fluid and gas flux that ultimately controls the health and population of *Beggiatoa* mats by bringing sulfide-rich fluid to the surface.

Short core modeling studies and short-term deployments of benthic fluid flux chambers may not fully capture the long-term state of advection and gas expulsion in these dynamic seep systems (Suess & Whiticar, 1989; Carson et al., 1990; Torres et al., 2002; Tryon et al., 2002). Two studies of fluid flow within bacterial mats at cold seeps have previously uncovered discrepancies in our understanding of bacterial mat nutrient acquisition and fluid flow. Three benthic fluid flow meters (Chemical Aqueous Transport meters, CAT) were placed within bacterial mats at Southern Hydrate Ridge (SHR), a well-characterized seep area known for hosting methane-rich fluid and gas, for 30- and 45-days and revealed highly variable rates of fluid flow with frequent polarity reversals on the order of days (Tryon et al., 2002). Flow rates varied between -20 cm yr^{-1} to +1000 cm yr^{-1} depending on location and day, where negative flow direction is into the sediment and positive flow direction is out of the sediment. Curiously, the instrument with the highest upward flux rates showed seawater concentration of both Ca and total sulfur ($S_{total} = SO_4^{2-} + H_2S + HS^- + S^{2-}$) during much of the deployment. This is unexpected since the pore water composition in this region is significantly modified from seawater at 10 m depth (Tréhu et al., 2003; Tomaru et al., 2006) and seawater-type fluid would not have sufficient concentration of HS^- to fuel the bacterial mat population.

Another study at the Bush Hill seep in the Gulf of Mexico deployed a Mosquito benthic fluid flow meter within a bacterial mat for ~400 days. The flow meter measured variable flow direction and magnitude, but net flow in the bacterial mat was downward into the sediment and associated fluid chemistry for the duration of the deployment showed seawater values of Cl, Ca^{2+}, and SO_4^{2-} (Solomon et al., 2008). Yet again, the bacterial mat community appeared healthy and vibrant before instrument deployment and upon recovery. Though these are just two studies, the data presents two questions of importance: (1) is upward advection of seawater required to sustain bacterial mat communities or do they persist within a variable flow regime where net flow may be downward over long periods of time; and (2) how are thiotrophic bacterial mats surviving in SO_4^{2-}-rich environments when they require HS^- to fuel metabolism and growth?

To address these questions, we collected and analyzed data from two benthic fluid flow meters deployed within a *Beggiatoa* mat in a seep area known as Einstein's Grotto at Southern Hydrate Ridge (SHR) (Figure 3.1). These instruments are deployed and maintained as part of the Ocean Observatories Initiative Regional Cabled Array (OOI-RCA). SHR is one of the most studied and best characterized seep locations globally. It has been the focus of dozens of hydrologic, geochemical, biological, and geophysical studies since its discovery, including two

Ocean Drilling Program legs (Westbrook et al., 1994; Tréhu et al., 2003), and has been a cabled instrument location of the OOI-RCA since 2013 (Trowbridge et al., 2019).

3.2 Southern Hydrate Ridge

Southern Hydrate Ridge (SHR) is a hummocky patch of seafloor known for hosting seepage of methane-rich fluid and gas. It is located approximately 90 km offshore Oregon, United States, on the second accretionary ridge of the Cascadia subduction zone (Figure 3.1) at 780 m below sea level. The hummocky terrain is likely the product of periodic eruptions of trapped gas buried shallowly beneath the seafloor. This area is dominated by episodic gas expulsion and dynamic aqueous fluid flow, lush chemosynthetic communities, and massive near-surface gas hydrates.

Regionally, SHR is a broad location of upward fluid advection. Continued disequilibrium compaction and mineral dehydration related to subduction of the Juan de Fuca plate leads to dewatering of the sediments and the upward flux of pore water and gas. Seeps are the seafloor manifestation of fluids originating from depth and flowing along permeable conduits such as fault zones and dipping high-permeability stratigraphic horizons. All seeps are locations of upward fluid flow; yet the transport of fluid (i.e. liquid and gas) differs among seeps. In locations like SHR, CH_4 is primarily transported as free gas (Torres et al., 2004; Lieu and Flemings, 2007; Bangs et al., 2011). As this gas migrates upward it partially dissolves if the pore water is undersaturated with respect to methane. Rates of water and gas flow are controlled by the relative permeability of the sediments and/or fractures to each of the phases. When gas saturations are high, the relative permeability to gas is much greater than for water, favoring gas transport over water transport (Ingebritsen et al., 2006; Liu and Flemings, 2007). In a gas column, water is overpressured if conditions exceed hydrostatic pressure, yet gas follows a static pressure gradient. This is due to gas displacing the water upward through the gas column where the permeability to water is small. Capillary pressure increases with decreasing depth (i.e. towards the seafloor) and forces gas into smaller and smaller pore spaces, thus causing an increase in gas saturation and eventually causing the gas column to reach overburden stress and fractures will dilate to allow further upward gas migration (Liu and Flemings, 2007). In this way, high gas saturations favor gas transport over liquid transport during two-phase flow. This has been modeled (Liu and Flemings, 2007; Daigle and Dugan, 2010) and interpreted for Hydrate Ridge (Tréhu et al., 2004).

Two types of flow meters are deployed annually as part of the Hydrate Ridge focus site of the OOI-RCA, the Mosquito (Solomon et al., 2008) and the CAT meter (Tryon et al., 2001). Each Mosquito and CAT instrument continuously samples fluid and measures fluid flow rates using non-reactive tracer solutions. Instruments are recovered and redeployed annually during OOI maintenance cruises, and the flow meters were always placed in a region of the healthy bacterial mat. This multiyear record of long-term fluid flow and pore water chemistry represents a one-of-a-kind dataset that can be used to explore temporal fluctuations in seep fluid and chemical fluxes. Additional complementary qualitative data include repeat seafloor surveys that document changes in seafloor communities that can be related to changes in flow regime. Here we assess and interpret 5 years of continuous fluid flow rate measurements and fluid chemistry from these instruments between 2013 and 2018 to understand the biogeochemical impacts of regional hydrogeology on *Beggiatoa* mat communities.

3.3 Materials & Methods

3.3.1 – Mosquito Fluid Flow Meter

The Mosquito uses osmotic pumps and addition of a fluorescein tracer to continuously measure fluid flow rates and solute fluxes at multiple depths below the seafloor (Solomon et al., 2008). Five titanium capillary needles are inserted into the sediment at depths >10 cm in order to bypass the zone of bioturbation. These needles are set at different sampling depths between 10 and 35 cm below seafloor (Figure 3.2). The second deepest needle is the tracer Injection Needle. The sampling needles are connected to Teflon sample coils pre-filled with ultrapure water, which are connected to OsmoSampler (OS) pumps (Jannasch et al., 2004). Each OS uses a salinity gradient to drive flow of fresh water across two osmotic membranes over time, thereby also pulling fresh water from the sample coils into the osmotic pump, which pulls pore water from the respective needle in the sediment.

The Mosquito frame is initially placed on the seafloor with the needles in the "up" position. A pull pin triggers a pulley system that pushes the Ti needles into the sediment at the pre-determined depths. The Injection Needle is positioned in the center of the needle array approximately 5 cm above the deepest sampling needle (Needle 4) and is used to inject a point source of fluorescein tracer solution density-matched to SHR bottom water. The tracer concentration time-series at each depth is used to quantify fluid flow rates at approximately 4-day time resolution.

Time-series tracer concentrations at each sampling depth are modeled using Fick's Second Law of Diffusion (Equation 3.2):

$$\frac{\partial C}{\partial t} = D_s \cdot \frac{\partial^2 C}{\partial x^2} - \frac{v \partial C}{\partial x} \qquad \text{(Eqn. 3.2)}$$

where C is concentration, t is time, D_s is the sediment diffusion coefficient, x is vertical distance, and v is the fluid velocity. The fluorescein tracer is injected into the sediment as a point source of mass *M* at a single depth at the initial time of deployment. This mass then diffuses and advects through the sediment. The concentration (*C*) of fluorescein is zero in the sediment in all planes (x, y, z) at time zero. With these initial conditions and no other sources or sinks of fluorescein, and assuming fluorescein adsorption onto sediment particles is negligible (e.g. Sabatini and Austin, 1991; Sabatini, 2000), the concentration can be modeled in space and time using the analytical solution of Baetsle (1969) (Equation 3.3):

$$C(x,y,z,t) = \frac{M}{8(\pi t)^{3/2}\sqrt{D_{xx}D_{yy}D_{zz}}} \times exp\left(-\frac{X^2}{4D_{xx}t} - \frac{Y^2}{4D_{yy}t} - \frac{Z^2}{4D_{zz}t}\right) \qquad \text{(Eqn. 3.3)}$$

where X, Y, and Z are the coordinates following the center of mass of fluorescein which are defined as:

$$X = x - v_x t$$

$$Y = y - v_y t$$

$$Z = z - v_z t$$

The flow velocity (v) can be solved for numerically. Fluid flow rates are resolved by matching the time-series tracer concentrations to forward model simulations.

The molecular diffusion coefficient of fluorescein (D_m) was estimated following the Wilke and Chang (1955) method using average measured bottom water temperature and dynamic viscosity of seawater at this temperature, salinity, and depth (Solomon et al., 2008). The sediment tortuosity (Equation 3.4) was estimated from the average measured sediment porosity (ϕ = 0.63–0.70 depending on year and location) using Boudreau's Law (Boudreau, 1996). The sediment diffusion coefficient (D_s) is inversely proportional to the tortuosity and was calculated using Equation 3.5.

$$\theta^2 = 1 - ln(\varphi^2) \qquad \text{(Eqn. 3.4)}$$

$$D_s = \frac{D_m}{\theta^2} \qquad \text{(Eqn. 3.5)}$$

Modeled flow rates are sensitive to changes in the sediment diffusion coefficient used. An increase of 10%, 33%, and 100% in D_s would increase calculated flow rates by 23%, 45%, and 81%, respectively (Solomon et al., 2008).

The net fluid flow rate for each instrument is calculated by first multiplying the rate of fluid flow by the duration of that rate and summing the total distance over the deployment period to yield the net distance traveled. The net distance traveled (cm) divided by the total time each instrument was deployed (yr) yields the net flow rate over the sampling period.

3.3.2 – Chemical Aqueous Transport (CAT) meter

The CAT meter is designed to measure both upward and downward flow of water out of and into the sediment (Tryon et al., 2001) (Figure 3.3). Sample collection is driven by an osmotic pump that sits within a PVC housing. Two freshwater chambers are separated from a larger saltwater chamber by semi-permeable osmotic membranes. The osmotic gradient and membrane surface area determine osmotic pump rate. A bag of RbCl tracer density-matched to SHR bottom water sits within the saltwater chamber and dispenses tracer into a sample inlet/outlet tube at the same rate that sample is withdrawn (Figure 3.3). Two sample coils pre-filled with ultrapure water (18.2 MΩ) connect the inlet/outlet tube to the freshwater chambers of the osmotic pump.

The pattern of Rb concentrations within each of the two sample coils gives a timeseries of flow direction and flow rate. Only one sample coil will typically contain a mixture of pore water/seawater and tracer and the other coil will contain either no tracer or all tracer. Fluid flow rate is determined from the pump rate (P) of either the upstream (P_x) or downstream (P_y) osmotic pump and the volumetric flow rate (q), defined as the flux rate multiplied by the area of the collection chamber. If $q < P_x$, then the upstream coil is a mixture of tracer and pore water/seawater and the downstream coil contains only tracer. If $q > P_x$, then the upstream coil is entirely pore water/seawater and the downstream coil contains a mixture of tracer and pore water/seawater. The flux rate, Q, q/A, where A is the cross-sectional area of the collection chamber, can then be calculated using these relationships and the fraction of tracer measured in the sample. These calculations are described in Equations 3.6 and 3.7 below,

$$\text{if } q < P_x,\ \ f_y = 1,\ \ f_x = 1 - \frac{q}{P_x} \qquad \text{(Eqn. 3.6a)}$$

$$\text{or}\ \ Q = \frac{P_x}{A}(1 - f_x), \qquad \text{(Eqn. 3.6b)}$$

$$\text{if } q > P_x,\ \ f_x = 0,\ \ f_y = \frac{P_x + P_y}{q + P_y} \qquad \text{(Eqn. 3.7a)}$$

$$\text{or}\ \ Q = \frac{1}{A}\left(\frac{P_x}{f_y} + \frac{P_y}{f_y} - P_y\right) \qquad \text{(Eqn. 3.7b)}$$

where f is the fraction of Rb in a sample (C_{sample}/C_{tracer}, where C is the concentration of Rb in the sample and tracer solution, respectively). For further reading, see Tryon et al (2001).

The CAT meter is housed in a titanium frame with a 0.37 m^2 footprint collection chamber that seals off a portion of the seafloor and channels water into the inlet/outlet tube, amplifying flow so that low flow rates can be quantified.

3.3.3 – Instrument Sampling & Chemical Analyses

Each Mosquito and CAT meter was deployed and recovered each year at SHR using either Remotely Operated Vehicle (ROV) *ROPOS* or ROV *Jason*.

After recovery, each Mosquito sample coil was sectioned into 45 cm segments representing approximately 4 days of *in situ* sampling. Mosquito samples were subsampled into aliquots upon coil sectioning and stored appropriately for particular chemical analyses. All chemical analyses for the Mosquito samples were conducted at the University of Washington.

Every sample was analyzed for fluorescein concentration. Fluorescein samples were analyzed on a Cary Eclipse Fluorescein Spectrophotometer. This analysis is most precise in the range of $5x10^{-7}$ and 10^{-4}, thus all samples were diluted to this range. Calibration was achieved using six standards spanning this concentration range. Precision was typically <3%.

Every other sample was additionally analyzed for sulfate concentration, chloride concentration, and the major components of seawater (Ca, Mg, K, Na, S). Sulfate samples were diluted 1:101 with 0.49 mM zinc acetate solution and analyzed on a Metrohm 882 Compact Ion Chromatograph (IC) Plus with precision <2%. Due to an issue with sub-sampling, we were unable to measure sulfate concentrations via IC from Mosquitos deployed in 2016 and 2017, and instead total sulfur was measured using an inductively coupled plasma optical emission spectrometer (ICP-OES). Total sulfur (S_{total}) is the sum of all sulfur species in the pore fluid including sulfate. Aliquots for chloride concentration were analyzed using potentiometric titration with $AgNO_3$ (Gieskes et al., 1991) with precision of <0.3%. Major element samples were diluted 1:101 with 1% HNO_3 solution and analyzed using a Perkin Elmer 8300 ICP-OES at the University of Washington (UW). Major element concentrations were calibrated against IAPSO standard seawater.

Upon recovery of the CAT meter, each sample coil was sectioned into 34 cm segments with each segment representing approximately 1.5–2 days of sampling. Every third sample was analyzed for major (Ca, Mg, K, Na, and S) and minor (B, Ba, Li, Sr, Fe, and Mn) components of seawater plus Rb tracer concentration via ICP-OES at UW for CATs deployed between 2015 and 2018. Since every third sample was analyzed, the time between each data point in the time series presented in this paper is approximately 4.5–6 days. Instruments deployed between 2013 and 2014 were analyzed by Michael Tryon at SIO. Every fourth sample was analyzed for Cl concentration via titration with silver nitrate for instruments deployed in 2013 and 2014 whereas Cl was measured in every tenth sample for CATs deployed in 2015 and beyond.

Major element and minor element samples analyzed at UW (from both Mosquitos and CAT meters) were diluted 1:101 and 1:26, respectively, with 1% HNO_3 solution. Major element concentrations were calibrated against dilutions of IAPSO standard seawater. Minor element concentrations were calibrated against dilutions of an in-house mixture of SPEX CertiPrep single element standards. Analytical precision varies per element and ranges from < 2%–4%.

3.3.4 – Push Core Pore Water

Pore water was extracted from two push cores at 2 cm depth resolution with Rhizon fluid samples in 2018. Hydrogen sulfide and sulfate samples were immediately diluted 1:21 with 0.49 mM zinc acetate solution. Hydrogen sulfide concentrations, here referred to as ΣH_2S ($\Sigma H_2S = H_2S + HS^- + S^{2-}$), were analyzed colorimetrically using an adaptation of the Cline method (Cline, 1969).

3.3.5 – Push Core Porosity

Push cores were collected within and adjacent to Mosquito placement each year upon instrument recovery to measure average surface sediment porosity. Sediment plugs of known volume were collected from each push core at approximately 2 cm depth resolution and placed in empty, pre-weighed glass bottles. The mass of each sample bottle was measured then placed in an oven at $60^{\circ}C$ for 24 hours to evaporate pore water and weighed again. The differences in mass and pore water salinity were used to calculate pore water volume, wet and dry bulk density and grain density which were then used to calculate porosity.

3.3.6 – Reaction-Transport Modeling of Pore Water Profiles from Push Cores

A finite element model was used to calculate net sulfate reduction rates and simulate pore water bisulfide profiles using various initial conditions. A full description of this model is explained by Berg (2020). Briefly, the model assumes steady state conditions and considers pore water advection, burial rate, and chemical reactions. Inputs to the model include sedimentation rate of 20 cm kyr^{-1}, constant porosity with depth of 0.7, bottom water temperature of 4ºC, and an increasing temperature gradient within the sediment of 0.1ºC m^{-1}. The model domain includes 0 cm to 50 cm sediment depth with 50 depth intervals, and a timestep of 0.001 yr. Validation runs confirmed that 3.0x10^{4} timesteps was sufficient to achieve steady state.

3.3.7 – Diffusive Flux Calculations

The diffusive sulfide flux to the seafloor was calculated from the push core pore water sulfide profiles collected in 2016 using Fick's first law of diffusion:

$$F = \varphi D_{sed} \frac{\partial C}{\partial z}$$

where F is the diffusive flux, φ is porosity, D_{sed} is the sediment diffusion coefficient, C is concentration of sulfide and z is depth. Porosity is known from shallow push cores taken each year and D_{sed} is calculated according to Equation 3.5. Diffusive sulfide flux calculations were applied to pore water concentrations within collected push cores.

3.4 Results

Fluid flow rates from the OOI-RCA instrumentation at SHR comprise the longest continuous record of subseafloor fluid flow rates at a seep site to date. In contrast to previous short-term flow meter deployments, the OOI-RCA fluid flow rate data show extended pulses of upward (positive flow rate values) and downward flow (negative flow rate values) over time within the same bacterial mat.

3.4.1 – 2013–2014 Deployment

During the period from summer 2013 to summer 2014, Mosquito flow meters located in the southeastern and western portions of the mat each recorded predominantly downward fluid flow during the deployment period with a net flow of -4.9 cm yr^{-1} (M2013) and -13.8 cm yr^{-1} (M-2), respectively (Table 3.1; Figure 3.4). M2013, deployed in the southeastern region of the mat, measured reversals in fluid flow direction over time with upward flow mainly occurring during the last 140 days of the deployment. Rates of downward flow were much higher than the rates of upward flow. M-2 recorded mainly downward flow with two short pulses of upward flow lasting 22 days. CAT2013, located adjacent to M2013, did not detect fluid flow over the deployment period (data not plotted but is available through OOI). The chemical composition of fluid was not analyzed for these instruments.

3.4.2 – 2014–2015 Deployment

M2014 and CAT2014 flow meters were placed next to each other in the southwestern portion of the mat, which had expanded and increased in thickness between 2013 and 2014 (Figure 3.4). Needles 1 and 2 of Mosquito M2014, penetrating 13.2 cm and 18.2 cm, respectively, recorded predominantly downward flow of seawater over the deployment period with an average net flow of -11.4 cm yr^{-1} (Figure 3.4). Mosquito M2014 fluid samples were strongly depleted in Ca and SO_4^{2-}, with Ca concentrations <3mM and SO_4^{2-} concentrations

<1mM throughout the deployment period (Figure 3.6), though Mg, K, and Na concentrations were constant at seawater values (Figure B-1).

CAT2014 showed upward flow of varying magnitude over the deployment period (Figure 3.5) with net flow of +1.7 cm yr^{-1}. Ca concentrations in the CAT2014 record began near seawater value and slowly decreased over time to a consistent concentration of 3–6 mM (Figure 3.7). This slow change in Ca from seawater value to constant concentration is due to the time required for fluid discharging from the sediments to flush the collection chamber of bottom water entrapped during initial deployment. Total sulfur (S_{total}), Mg, Na, and K concentrations were constant over the deployment period at seawater values (Figure B-2).

3.4.3 – 2015–2016 Deployment

From 2015 to 2016, the Mosquito (M2015) measured persistent downward flow punctuated by periods of upward flow, however net flow for the year was -2.75 cm yr^{-1}. The pore fluid Mg, K, and Na concentrations were again constant at seawater values over the deployment, but Ca and S_{total} concentrations were strongly depleted with respect to seawater concentrations.

CAT2015 was located next to M2015 and recorded fluid flow rates greater than the upper detection limit of the instrument deployed (7.5 cm/yr). The fluid discharging from the sediment once again showed seawater concentrations of Mg, K, and Na but Ca remained between 2–3 mM for most of the deployment period and S_{total} concentrations were <15 mM (Figure 3.7).

3.4.4 – 2016–2017 Deployment

Mosquito M2016 was positioned on a southern lobe of the mat. Net flow was downward at a rate of -16.1 cm yr^{-1}. Cl, Mg, K, and Na concentrations were constant over the deployment at seawater values. Calcium concentrations were between 2 and 5 mM over the deployment period, whereas total sulfur concentrations fluctuated greatly during the length of the deployment, spanning concentrations as low as 1.4 mM and as high as 61.7 mM. Sulfur concentrations were elevated above seawater value for a total of 105 days between April and July 2017. The elevated sulfur concentrations occurred during a period when flow was downward into the sediment with no reversal in flow direction.

Fluid flow rates at CAT2016 were above the upper detection limit of the instrument of >4 cm/yr for the duration of the deployment. Fluid chemistry was once again identical to seawater for all major elements except Ca and S_{total}, which ranged from 3–6.5 mM and 7.5–21 mM, respectively.

3.4.5 – 2017–2018 Deployment

Between 2017 and 2018 the instruments were deployed in the northwestern portion of the mat and suggest a change in the system. For M2017, fluorescein tracer was detected at the Needle 3 sampling depth (19.4 cm) but was not detected at Needle 2 only 5 cm shallower than Needle 3. The net fluid flow rate recorded in Needle 3 was -6.5 cm yr^{-1}. The modeled flow rate history for Needle 3 predicts the arrival of tracer at the Needle 2 depth at 44 days after deployment, yet fluorescein concentration at this depth remained undetectable for the entire record (Figure B-3). This result suggests decoupling of the flow regime between 14.4 and 19.4 cm.

Calcium concentrations remain lower than 4 mM for the duration of the deployment at both Needle 2 and Needle 3 depths. S_{total} at Needle 3 remains between 5 and 10 mM for the first 135 days of the sampling record and then fluctuates broadly between 5 and 40 mM for the rest of the deployment. S_{total} values at Needle 2 also vary from 5–40 mM over the course of the deployment period but show no trend over time.

CAT2017 recorded high rates of upward fluid flow over the first 300 days before flow direction switched to downward into the sediment. Net flow for the year was upward at a rate of +20.5 cm yr^{-1}. S_{total} concentrations were less than 5 mM before trending upward to a maximum of ~25 mM at the time of the flow reversal. Calcium concentrations remained less than seawater value while all other major elements were at seawater values.

3.4.6 – Push Core Pore Water Profiles

Two push cores were collected using ROV *Jason* during the recovery of M2017 in 2018 to evaluate sulfur speciation in the upper 10 cm of the sediment column that Mosquito meters do not sample (the shallowest sampling needle is positioned at 12 cmbsf). PC-1 was collected within the footprint of the Mosquito where the titanium needles were sampling pore water, and PC-2 was taken just outside of the Mosquito footprint in a patch of thick bacterial mat. Sulfate concentrations in PC-1 are approximately seawater value in the upper 3 cm and then decrease to 10 mM by 6 cm depth (Figure 3.8). At 12 cm depth, the concentration increases to 43.9 mM. Replicate analysis of this sample confirmed the value. ΣH_2S concentrations are 6.4 mM just below the seafloor at 1 cm depth and then increase sharply to 13.4 mM at 6 cm depth and remain elevated. Though SO_4^{2-} and ΣH_2S concentrations are also high in PC-2, the profiles look starkly different. Sulfate in PC-2 is between 44 and 50 mM for the upper 9 cm and then decreases to 25 mM by 11 cm and remains between 23 and 29 mM until 19 cm depth. Sulfide concentrations at 3 cm are 11 mM and reach a maximum of 13.5 mM by 9 cm and remain relatively constant below this depth. Chloride concentrations throughout both cores are seawater value.

3.5 Discussion

Two distinct observations can be made from the flow rate and chemistry data. The first observation is that there is perennial net downward transport of seawater into the sediment underlying filamentous bacterial mats at SHR. This observation is highly unexpected given the presence of the healthy *Beggiatoa* bacterial mat community that rely on the upward flux of reduced sulfur. Though the spatial extent of *Beggiatoa* changes between annual flow meter deployments, each instrument is initially placed within healthy portions of the mat. In a predominantly downward flow regime, downward advection would be combatting the upward diffusion of HS^- to fuel *Beggiatoa* metabolism. Yet, these bacteria persist from year to year.

3.5.1 – Potential mechanisms of shallow seawater circulation

Each year, Mosquitos and CATs document advection of fluid into and out of the sediment in different regions of the *Beggiatoa* mat. Most areas of the mat are regions of net downward transport of fluid with discrete portions of the mat dominated by upward fluid advection. This is consistent with shallow circulation of seawater below the mat where regions of downward advection can be thought of as recharge zones and regions of upward advection are discharge zones.

Shallow seawater circulation has been observed previously on other margins. On the lower slope of the eastern Nankai accretionary wedge, Henry et al (1992) noted that the anomalous thermal structure of sediment within and on the perimeter of clam colonies could only be explained by the presence of shallow seawater convection whereby seawater downflow must occur outside of the clam colony to a depth of 1–2 meters, much deeper than the depth that is pumped by the clams themselves. They examined both temperature gradients and salinity differences between the bottom seawater and seep fluid as drivers of seawater circulation and found that salinity differences of just 5‰ between seawater and seep fluid could drive salinity-induced convection cells. Modeling showed that salinity and permeability of the sediment/conduit are the most important factors that control the velocity of fluid venting. In contrast, salinity measurements between seawater and pore water at Einstein's Grotto are not significantly different and range between 34‰ and 35‰. Therefore, density-driven convection is not driving seawater circulation at SHR.

Fracturing of sediment by gas transport could be one mechanism for greatly increasing sediment permeability (Boudreau et al., 2005) and open a more direct pathway to the seafloor. A fracture reaching the sediment surface could entrain seawater as rising gas bubbles move toward the seafloor, thereby bringing seawater deeper into the seafloor sediment. Haeckel et al (2007) modeled bubble-induced pore water mixing to explain why pore water solute profiles from an active seep in the Sea of Okhotsk are concave-up with approximately seawater chemical values in the upper 200–300 cm. However, this mechanism of bubble irrigation would produce no measurable net flow in the flow meter records. Each year, the flow meters recorded downward flow of seawater into the sediments, which would also produce pore water solute profiles that are concave-up. Additionally, bubble irrigation cannot explain the observation of upward fluid advection in discharge regions of the mat. In this regard, though bubble irrigation may occur at SHR, the area sampled in this time series is likely dominated by fluid circulation.

It is likely that the broad-scale process inducing downward flow of seawater into the sampled bacterial mat is the expansion and contraction of very shallow subsurface gas reservoirs. Overpressure of this subsurface gas reservoir can build until new conduits are forced open venting the trapped gas to the seafloor (Torres et al., 2002). Previous studies (Torres et al., 2002) and unpublished qualitative observations made during annual OOI-RCA maintenance cruises support the presence of shallowly buried pockets of free gas within the upper ~10-20 cm at SHR, as well as at other seeps along portions of the Cascadia (Philip et al., *submitted*) and Hikurangi margins (Aylward et al., 2020). Streams of gas bubbles are often seen bursting from the seafloor sediment upon insertion of a probe or push core, requiring that there be shallow reservoirs of free gas. In the proposed scenario, once there is no longer gas within the shallow reservoir, and assuming there is not an instantaneous replenishment of this gas, water must be cycled back into the sediment to satisfy the conservation of mass. It should be noted that in this scenario the gas reservoir must be constrained laterally so that gas can only vent upward.

A smaller-scale process likely inducing downward flow of seawater is the dissolution of rising CH_4-rich gas bubbles. In a downward flow regime, gas bubbles rise toward the surface via permeable conduits while seawater downwells. As the gas bubbles rise above the SMT they intersect a zone where the CH_4 concentration outside of the bubbles is lower than the concentration inside the bubbles and, therefore, CH_4 gas diffuses out of the bubble and into the pore water. The diffusional loss of CH_4 causes rising bubbles to shrink (McGinnis et al., 2006) and bubble shrinkage induces drawdown of seawater into the sediment (Haeckel et al., 2004).

3.5.2 – Biogeochemical implications of seawater circulation

Below the bacterial mat investigated in this study, SO_4^{2-} is strongly depleted with respect to seawater at shallow depths though seawater is transported into the system. In an upward flow regime, the SO_4^{2-} flux from overlying bottom water into the sediment must be diffusional and in the opposite direction of the upward flow of reduced fluid. The Mosquito results show that SO_4^{2-}

at SHR is advected into the sediment but is strongly reduced by the time the fluid reaches the shallowest sampling needles at ~10 cm depth. Complete reduction of seawater SO_4^{2-} requires the sulfate-methane transition (SMT) to be shallower than 12 cm depth and the rate of AOM to be far greater than in an upward flow regime.

A finite element model, run to steady state from seawater values, was used to understand the difference in sulfate reduction rates (SRR) in an upward and downward flow regime. The model assumes the SMT is located at 10 cm depth and that SO_4^{2-} is only consumed via AOM. Ocean Drilling Program (ODP) temperature vs. depth profiles at SHR show no curvature over the upper 100 m of the sediment column, indicating little-to-no upward advection of water from depth, and thus little-to-no upward advection of heat. Curvature in the temperature profile would be observed if upward advection of fluid exceeded +10 cm yr^{-1} (Tréhu et al., 2006). In an upward flow regime where fluid velocity is equal to a maximum of +10 cm yr^{-1}, the SRR would equal 128 mol m^{-3} yr^{-1} (Figure 3.9). Switching the flow direction from upward to downward at -10 cm yr^{-1} increases the SRR to 330 mol m^{-3} yr^{-1-}, or more than double the rate in an upward flow regime. At a downward flow rate of 15 cm/yr, similar to what was seen at Einstein's Grotto between 2013–2014 and 2016–2017, the SRR at 10 cm depth increases to 400 mol m^{-3} yr^{-1-}, or more than triple the rate that is modeled in an upward flow regime. We have no direct constraints on the SMT depth except that it is shallower than 10 cm, which is the shallowest depth sampled by the Mosquito. If the SMT is shallower than 10 cm, then the SRR increases significantly (Table 3.2).

Enhanced rates of AOM in a downward flow regime should also yield enhanced rates of HS^- and HCO_3^- production (Equation 3.1). Enhanced production of HCO_3^- increases alkalinity in the pore water. A portion of HCO_3^- is sequestered in authigenic carbonates formed *in situ*, thus also enhancing the consumption of Ca^{2+} from pore water. Higher rates of HS^- production from AOM should create a stronger gradient of HS^- to the sediment surface to fuel benthic organisms including *Beggiatoa* and clams. *Beggiatoa* and other thiotrophic bacterial mats require HS^- and NO_3^- to fuel metabolism and growth (Equation 3.8).

$$HS^- + NO_3^- + H_2O + H^+ \rightarrow SO_4^{2-} + NH_4^+ \qquad \text{(Eqn. 3.8)}$$

Enhanced delivery of HS^- to the seafloor bacterial mat community should drive enhanced consumption of NO_3^- from bottom water as well as enhanced drawdown of O_2 via aerobic oxidation of HS^- (Equation 3.9).

$$HS^- + 2O_2 \rightarrow SO_4^{2-} + H^+ \qquad \text{(Eqn. 3.9)}$$

Since the rate of AOM is enhanced in a downward fluid flow regime compared to an upward flow regime, the consumption of nitrate, oxygen, and calcium and the production of alkalinity are also enhanced.

In a net downward flow regime, HS^- produced via AOM must diffuse upward toward the *Beggiatoa* against the flow. Shallow push core concentrations of ΣH_2S beneath the mat are similar to what has previously been reported beneath bacterial mats at SHR (Glass et al., 2014; Sahling et al., 2002). High rates of AOM in the shallow surface yield millimolar concentrations of ΣH_2S that create a strong diffusional gradient to the *Beggiatoa* above. The diffusive flux of ΣH_2S in the upper 3 cm of PC-2 yields a diffusive gradient of 6.62 mol $m^{-2}\,yr^{-1}$ to the overlying bacterial mat community. Yet, the cycling of sulfur is not straightforward. ΣH_2S concentrations in each push core remain constant rather than increasing with depth, as would be expected if ΣH_2S was diffusing from a clearly defined SMT, and SO_4^{2-} concentrations are greater than seawater value in the upper 10 cm of PC-2. One way that SO_4^{2-} concentrations can increase to such values is if the system is not closed, not in steady state, and if upward diffusing HS^- was reoxidized to SO_4^{2-} at shallow depth. This scenario is plausible, indeed likely, in a downward flow regime where the mixing of oxygen-rich water would drive the oxidation of reduced sulfur in the uppermost sediment column.

Additionally, diffusion of CH_4 across the bubble surface contributes to an increase in dissolved CH_4 above the SMTZ. This adds dissolved CH_4 above the SMT where there is a strong downward advection of SO_4^{2-} that is utilized to sustain high rates of AOM near the seafloor directly below the bacterial mat community and enables the coexistence of relatively high concentrations of both SO_4^{2-} and HS^-. There is evidence of this process in a previously published study of pore water beneath a cold seep at Formosa Ridge in the South China Sea where Zhang et al. (2017) show near-seawater SO_4^{2-} and elevated total sulfide concentrations above and below the SMTZ (Zhang et al., 2017), as well as in our dataset at Einstein's Grotto discussed below.

The question remains whether the shallow gradient of HS^- is large enough to produce a diffusional gradient to the surface that could support *Beggiatoa* metabolism. We used a finite difference model to produce HS^- profiles in steady state assuming initial seawater concentrations of 28.9 mM SO_4^{2-} and 0 mM HS^-. We ran the model using two different bottom boundary conditions representing the minimum and maximum possible HS^- concentrations at depth. In one scenario, we set SO_4^{2-} and HS^- equal to 0 mM and assume that all HS^- in the 50 cm depth domain is precipitated in iron sulfide minerals and, therefore, all HS^- is consumed from pore water at depth (Figure 3.10 a, b). In another scenario, we set HS^- equal to 28.9 mM at depth and assume that there is no sink for HS^- in the sediment column (Figure 3.10 c, d). In each scenario we assume that SO_4^{2-} is only consumed through AOM and the ratio of SO_4^{2-} reduced and HS^- produced is 1:1. We ran the model simulation assuming upward fluid flow at 10 cm yr^{-1} and downward fluid flow at 15 cm yr^{-1} with the SMT depth set at either 2 cm or 10 cm. The rates of sulfate reduction used in each scenario are given in Table 3.2. In the scenario where HS^- is depleted at depth, the diffusional flux of HS^- to the surface *Beggiatoa* is greater in the downward advection regime than in an upward advection regime (Figure 3.10a, b). Regardless of bottom boundary condition, the diffusional flux of HS^- in a setting dominated by strong downward advection of seawater is either greater than or equal to the diffusional flux in an upward advection setting. Thus, *Beggiatoa* and other surface dwelling thiotrophic cold seep organisms do not need the upward advection of sulfide-rich fluid in order to thrive. Indeed, inhabiting areas dominated by the shallow circulation of O_2^- and SO_4^{2-}-rich fluid is more beneficial to the *Beggiatoa* community than colonizing areas dominated by the upward advection of reduced fluid.

3.6 Conclusion

The data from the long-term OOI-RCA instruments indicate that drawdown of seawater rich in SO_4^{2-} coupled with high concentrations of dissolved CH_4 boosts the rate of AOM and therefore the production of HS^- and drives a steep, shallow diffusional flux of reduced sulfur to the bacterial mat community at the seafloor. Shallow seawater circulation is potentially pervasive at active seepage sites globally. This phenomenon has been observed offshore Barbados (Henry et al., 1996), Nankai (Le Pichon et al., 1992), the Gulf of Mexico (Solomon et al., 2008), in push cores taken from another seepage location offshore Oregon called Pythia's Oasis (Philip et al., *submitted*), and at seep sites along the Hikurangi margin offshore New Zealand (Aylward et al., 2020). There are several mechanisms that can drive shallow seawater circulation at seep sites including density-driven circulation, expansion and contraction of gas pockets, and bubble dissolution. Shallow seawater circulation at each individual seep location may be driven by a combination of these mechanisms. Regardless of the exact mechanism driving seawater circulation at Einstein's Grotto, our study shows that a downward flow regime enhances rates of microbial reactions, specifically the rate of AOM, and that the production of alkalinity and consumption of O_2, NO_3, and SO_4^{2-} and Ca are much greater in a downward flow regime. If this process is observed to occur in seep environments globally, and considering that seeps are ubiquitous along continental margins, the impact for marine biogeochemical cycling would be profound.

The OOI-RCA offers an unparalleled opportunity to study real-time and long-term biogeochemistry at a dynamic, well-characterized seep system. More long-term monitoring of fluid flow rates and associated chemistry will only improve our understanding of fluid exchange with the ocean and the impacts of cold seep hydrogeology on benthic communities. Repeated, long-term monitoring of fluid and chemical exchange between the ocean and seafloor at other dynamic cold seep settings will vastly improve our understanding of surface and subsurface cold seep ecosystems and the role of seeps in global geochemical cycles.

3.7 References

Aylward, I.E., Solomon, E.A., Torres, M.E., Whorley, T.L., Harris, R.N., Hillman, J., Philip, B.T. (2020) Geochemical Constraints on the Hikurangi Margin Hydrogeologic System – Results from the SAFFRONZ Expedition. *American Geophysical Union Fall Meeting*.

Baetsle, L.H., (1969) Migration of radionuclides in porous media. In: Duhamel, A.M.F. (Ed.), Progress in Nuclear Energy XII, Health Physics. Pelargonium Press, Elmsford, N.Y., pp. 707-730.

Bangs, N.L.B., Hornbach, M.J., and C. Berndt (2011) The mechanics of intermittent methane venting at South Hydrate Ridge inferred from 4D seismic surveying. *Earth and Planetary Science Letters* **310**(1-2): 105-112.

Berg, R.D. (2020) Quantifying the deep: The importance of diagenetic reactions to marine geochemical cycles (Publication No. 10977010). [Doctoral dissertation, University of Washington]. ProQuest Dissertations Publishing.

Boetius, A. and Wenzhöfer, F. (2013). Seafloor oxygen consumption fuelled by methane from cold seeps. *Nature Geoscience* **6**(9) 725-734.

Boudreau, B.P. (1996) The diffusive tortuosity of fine-grained unlithified sediments. *Geochimica et Cosmochimica Acta* **60**(16): 3139-3142.

Boudreau, B.P., Algar, C., Johnson, B.D., Croudace, I., Reed, A., Furukawa, Y., Dorgan, K.M, Jumars, P.A., Grader, A.S. (2005) Bubble growth and rise in soft sediments. *Geology* **33**(6): 517-520.

Carson, B., Suess, E., Strasser, J.C. (1990) Fluid flow and mass flux determinations at vent sites on the Cascadia margin accretionary prism. *Journal of Geophysical Research* **95**(B6): 8891-8897.

Cline, J.D. (1969) Spectrophotometric determination of hydrogen sulfide in natural waters. *Limnology and Oceanography* **14**: 454-458.

Daigle, H. and B. Dugan (2010) Effects of multiphase methane supply on hydrate accumulation and fracture generation. *Geophysical Research Letters* **37**(20): 1-5. doi:10.1029/2010GL044970

Gieskes, J.M., Gamo, T., Brumsack, H. (1991) Chemical methods for interstitial water analysis aboard "*Joides Resolution", Ocean Drilling Program Texas A&M University*.

Glass, J.B., Yu, H., Steele, J.A., Dawson, K.S., Sun, S., Chourey, K., Pan, C., Hettich, R.L., Orphan, V.J. (2014) Geochemical, metagenomic and metaproteomic insights into trace metal utilization by methane-oxidizing microbial consortia in sulphidic marine sediments. *Environmental Microbiology* **16**(6): 1592-1611.

Haeckel, M., Boudreau, B.P., Wallmann, K. (2007) Bubble-induced porewater mixing: A 3-D model for deep porewater irrigation. *Geochimica et Cosmochimica Acta* **71**(21): 5135-5154.

Henry, P., Foucher, J-P., Le Pichon, X., Sibuet, M., Kobayashi, K., Tarits, P., Chamot-Rooke, N., Furuta, T., Schultheiss, P. (1992) Interpretation of temperature measurements from the Kaiko-Nankai cruise: Modeling of fluid flow in clam colonies. *Earth and Planetary Science Letters* **109**: 355-371.

Henry, P., Le Pichon, X., Lallemant, S., Lance, S., Martin, J.B., Foucher, J-P., Fiala-Médioni, A., Rostek, F., Guilhaumou, N., Pranal, V., Castrec, M. (1996) Fluid flow in and around a mud volcano field seaward of the Barbados accretionary wedge: Results from Manon cruise. *Journal of Geophysical Research* **101**(96): 297-323.

Hensen, C., Zabel, M., Schulz, H.N. (2006) Benthic Cycling of Oxygen, Nitrogen and Phosphorus. In: *Marine Geochemistry, 2nd Edn.* p. 207-240.

Ingebritsen, S.E., Sanford, W.E., Neuzil, C.E. (2006) Groundwater in Geologic Processes, 2nd Edn., 562 pp. New York: Cambridge University Press.

Jannasch, H.W., Wheat, C.G., Plant, J., Kastner, M., Stakes, D. (2004) Continuous chemical monitoring with osmotically pumped water samples: OsmoSampler design and applications. *Limnology and Oceanography Methods* **2**:102-113.

Le Pichon, X., Kobayashi, K., and Kako-Nankai Scientific Crew (1992) Fluid venting activity within the eastern Nankai Trough accretionary wedge: A summary of the 1989 Kaiko-Nankai results. *Earth and Planetary Science Letters* **109**: 303-319.

Liu, X. and Flemings, P.B. (2007) Dynamic multiphase flow model of hydrate formation in marine sediments. *Journal of Geophysical Resesarch* **122:** B03101.

McGinnis, D., Greinert, J., Artemov, Y., Beaubien, S.E., Wüest, A. (2006) Fate of rising methane bubbles in stratified waters: how much methane reaches the atmosphere? *Journal of Geophysical Research* **111**(C9)

Philip, B.T., Solomon, E.A., Kelley, D.S., Whorley, T.L., Roland, E., Tréhu, A.M., Tominaga, M., Collier, R.W. (2021) Fluid sources and oberpressures within the central Cascadia subduction zone revealed by a warm, high-flux seafloor seep. Manuscript submitted for publication.

Sabatini, D.A. and Austin, T.A. (1991) Characteristics of rhodamine WT and fluorescein as adsorbing ground-water tracers. *Ground Water* **29**: 341-349.

Sabatini, D.A. (2000) Sorption and intraparticle diffusion of fluorescent dyes with consolidated aquifer media. *Ground Water* **38**: 651-656.

Sahling, H., Rickert, D., Lee, R.W., Linke, P., Suess, E. (2002) Macrofaunal community structure and sulfide flux at gas hydrate deposits from the Cascadia convergent margin, NE Pacific. *Marine Ecology Progress Series* **231**: 121-138.

Solomon, E.A., Kastner, M., Jannash, H., Robertson, G., Weinstein, Y. (2008) Dynamic fluid flow and chemical fluxes associated with a seafloor gas hydrate deposit on the northern Gulf of Mexico slope. *Earth and Planetary Science Letters* **270**: 95-105.

Suess, E. and Whiticar, M.J. (1989) Methane derived CO_2 in pore fluids expelled from the Oregon subduction complex. *Paleogeography, Paleoclimatology, Paleoecology* **71**: 119-136.

Suess, E. (2014) Marine cold seeps and their manifestations: geological controls, biogeochemical criteria and environmental conditions. *International Journal of Earth Sciences* **103**: 1889-1916.

Tomaru, H., Matsumoto, R., Torres, M.E., Borowski, W.S. (2006) Geological and geochemical constraints on the isotopic composition of interstitial waters from the Hydrate Ridge region, Cascadia Margin. In: Tréhu, A.M., Bohrmann, G., Torres, M.E., Colwell, F.S. (Eds.), *Proceedings of the ODP Scientific Results, Leg 204*: College Station, TX (Ocean Drilling Program), 1-20.

Torres, M.E., McManus, J., Hammond, D.E., de Angelis, M.A., Heeschen, K.U., Colbert, S.L., Tryon, M.D., Brown, K.M., Suess, E. (2002) Fluid and chemical flux in and out of sediments hosting methane hydrate deposits on Hydrate Ridge, OR, I: Hydrological provinces. *Earth and Planetary Science Letters* **201**: 525-540.

Torres, M.E., Wallmann, K., Tréhu, A.M., Bohrmann, G., Borowski, ,W.S., Tomaru, H. (2004)

Gas hydrate growth, methane transport, and chloride enrichment at the southern summit of Hydrate Ridge, Cascadia margin off Oregon. *Earth and Planetary Science Letters* **226**: 225-241.

Tréhu et al. (2003) Leg 204 summary. *In* Tréhu, A.M., Bohrmann, G., Rack, F.R., Torres, M.E., et al., *Proceedings fo the Ocean Drilling Program, Initial Reports*, 204: College Station, TX (Ocean Drilling Program), 1-75. doi:10.2973/odp.proc.ir.204.101.2003.

Tréhu, A.M., Flemings, P.B., Bangs, N.L., Chevallier, J., Gràcia, E., Johnson, J.E., Liu, C.-S., Liu, X., Riedel, M., Torres, M.E. (2004) Feeding methane vents and gas hydrate deposits at south Hydrate Ridge. *Geophysical Research Letters* **31**: L23310.

Tréhu, A.M., Bohrmann, G., Torres, M.E., and Colwell, F.S. (2006) Leg 204 synthesis: gas hydrate distribution and dynamics in the central Cascadia accretionary complex. *In* Tréhu, A.M., Bohrmann, G., Torres, M.E., and Colwell, F.S. (Eds.), *Proceedings of the Ocean drilling Program, Scientific Results*, 204: College Station, TX (Ocean Drilling Program), 1–40.

Trowbridge, J., Weller, R., Kelley, D., Dever, E., Plueddemann, A., Barth, J.A., Kawka, O. (2019) The Ocean Observatories Initiative. *Frontiers in Marine Science* **6**: 74.

Tryon, M., Brown, K., Dorman, L., Sauter, A. (2001) A new benthic aqueous flux meter for very low to moderate discharge rates. *Deep-Sea Research Part 1* **48**: 2121-2146.

Tryon, M.D., Brown, K.M., Torres, M.E. (2002) Fluid and chemical flux in and out of sediments hosting methane hydrate deposits on Hydrate Ridge, OR, II: Hydrological processes. *Earth and Planetary Science* **201**: 541-557.

Wallman, K., Pinero, E., Burwicz, E., Haeckel, M., Hensen, C., Dale, A., Ruepke, L. (2012) The Global Inventory of Methane Hydrate in Marine Sediments: A Theoretical Approach. *Energies* **5**: 2449-2498.

Westbrook, G.K., Carson, B., Musgrave, R.S., et al. (1994) *Proceedings of the Ocean Drilling Program, Initial Report,* Vol. 146 (Part 1)

Wilke, C.R. and P. Chang (1955) Correlation of diffusion coefficients in dilute solutions. *American Institute of Chemical Engineers Journal* **1**(2): 264-270.

Zhang, X., Du, Z., Zheng, R., Luan, Z., Qi, F., Cheng, K., Wang, B., Ye, W., Liu, X., Lian, C., Chen, C., Guo, J., Li, Y., Yan, J. (2007) Development of a new deep-sea hybrid Raman insertion probe and its application to the geochemistry of hydrothermal vent and cold seep fluids. *Deep-Sea Research I* **123**: 1-12.

3.8 Figures and Tables

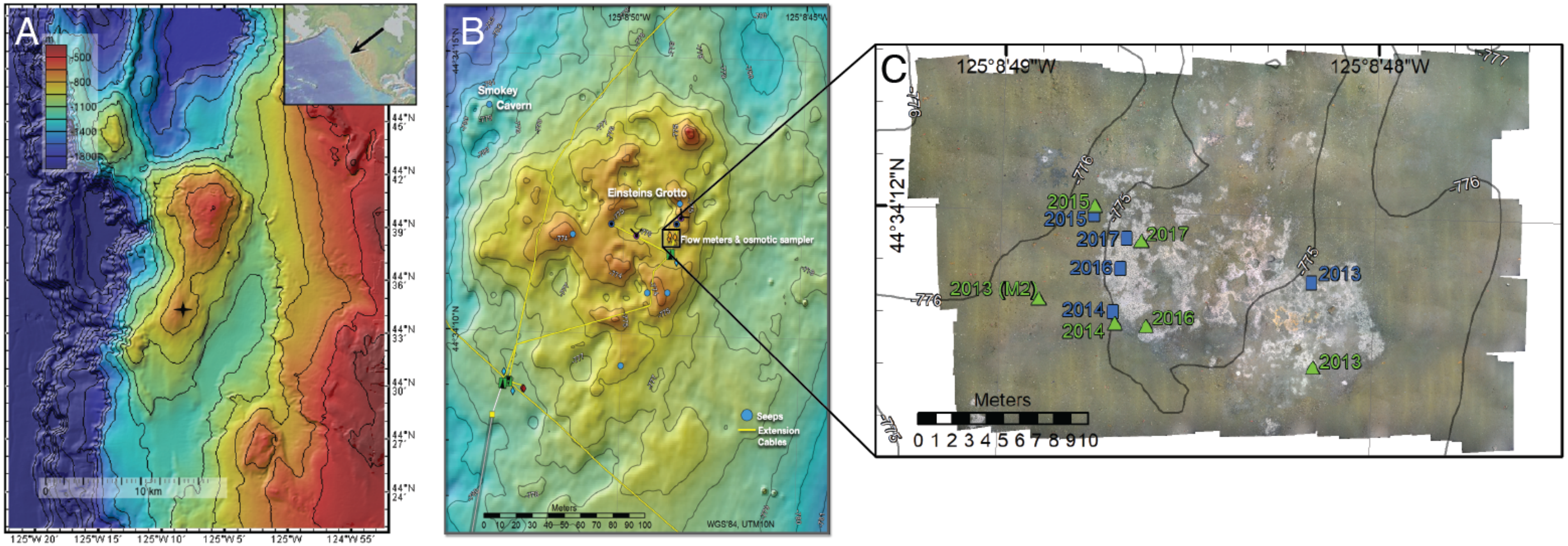

Figure 3.1. Southern Hydrate Ridge is located on the second accretionary ridge of the Cascadia margin (inset) at ~780 m below sea level (A) and is a cabled research site of the Ocean Observatories Initiative Regional Cabled Array (OOI-RCA). (B) The fluid flow meters discussed in this paper (orange diamonds) are part of a suite of instruments deployed to record a range of spatiotemporal changes in active fluid seepage at Einstein's Grotto *(Image credit: D.S. Kelley, University of Washington)*. (C) Photomosaic of Einstein's Grotto compiled from images captured in 2012. The *Beggiatoa* mat appears white and orange. The spatial extent and thickness of the bacterial mat changes over time. All instruments were placed in a healthy portion of the mat at the time of deployment. CAT meters are shown as blue squares and Mosquito instruments are shown as green triangles. *Photomosaic: M. Elend, University of Washington*.

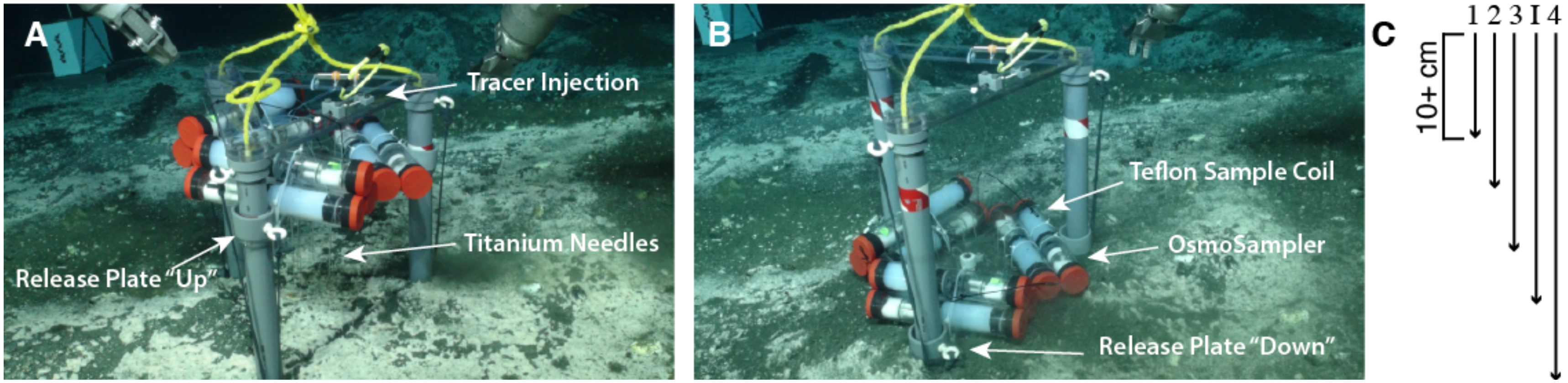

Figure 3.2. Photographs of the Mosquito fluid flow meter. (A) The titanium needles are secured into a plexiglass release plate that is kept in the "up" position to keep the needles from touching the seafloor during initial placement of the Mosquito. The release plate is then triggered into the "down" position pushing the needles to predetermined depths below the seafloor. (B) so that the needles penetrate the sediment at pre-determined depths. (C) Schematic of titanium needle penetration in each Mosquito flow meter. The top of Needles 1, 2, 3, and 4 are connected to Teflon sample coils and OsmoSampler pumps. A slotted hole ~1 cm from the tip of each needle is open to pore water. The Injection Needle (I) penetrates deeper than Needle 3 and shallower than Needle 4. The Needles are positioned in an array in the center of the Mosquito frame with the Injection Needle situated in the center of the array. *Photos modified from UW; NSF-OOI; CSSF*.

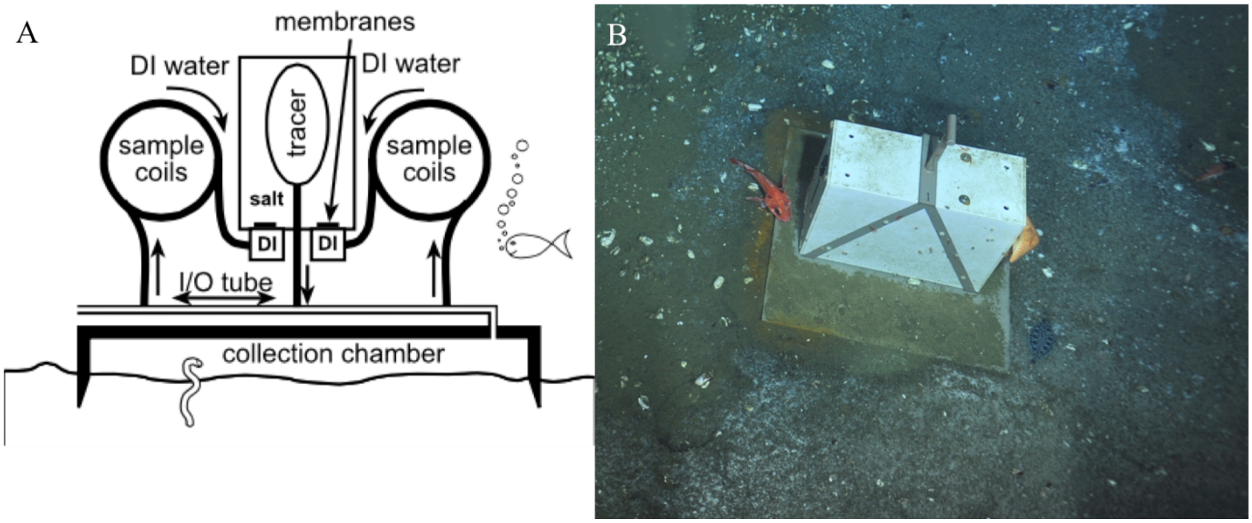

Figure 3.3. (A) Schematic of the CAT meter (Tryon et al., 2001). (B) CAT meter on the seafloor at Einstein's Grotto upon recovery in 2014 after one year of deployment. *Photo credit: NSF-OOI/UW/CSSF, Dive R1750, V14*. *Photo credit: NSF-OOI/UW/CSSF, Dive R1750, V14*.

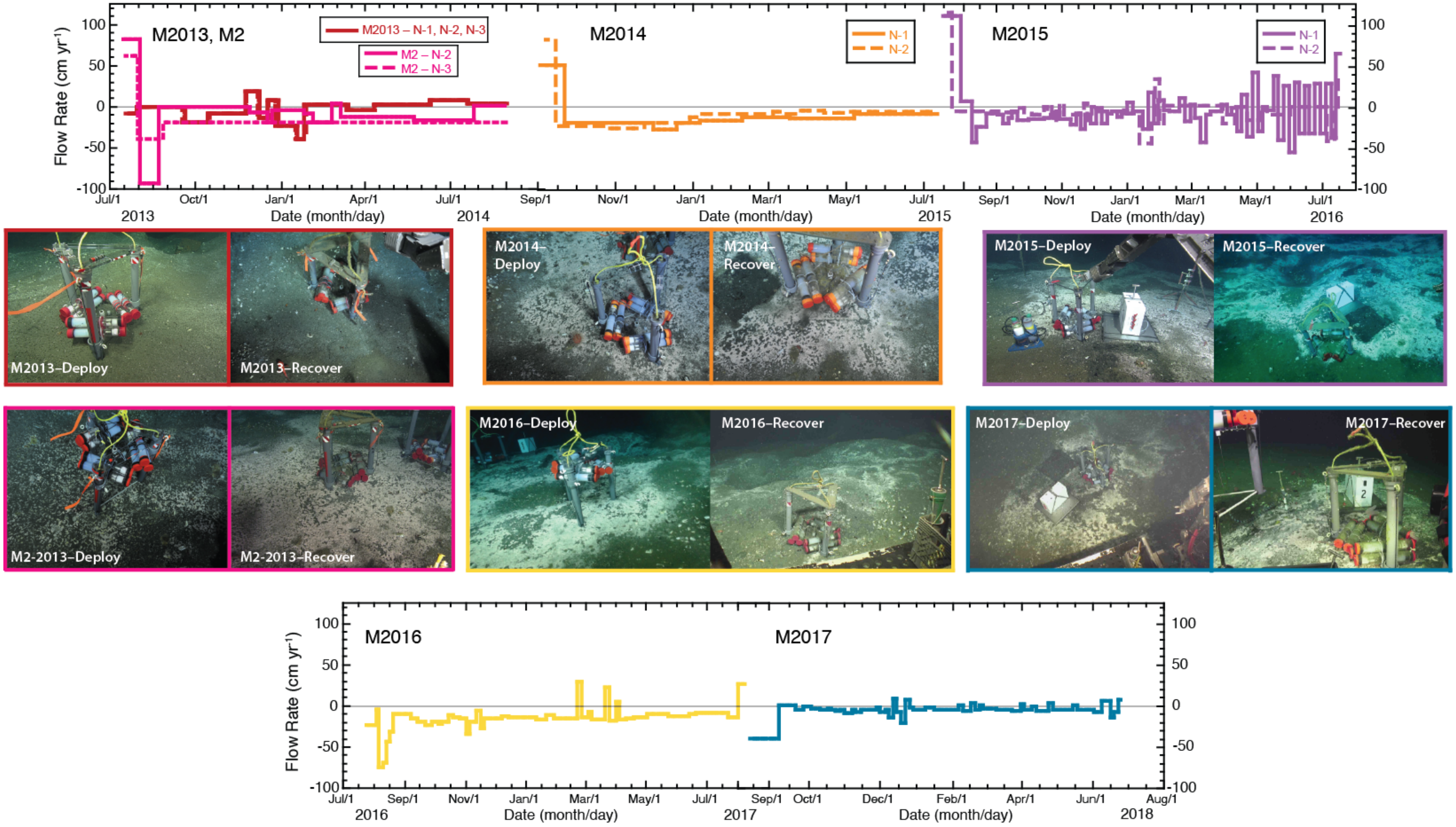

Figure 3.4. Fluid flow rates from Mosquitos deployed between Summer 2013 and Summer 2017. Modeled fluid flow rates were matched to measured fluorescein concentrations for all instruments. Flow rate plots are color matched to corresponding photos of each Mosquito and the bacterial mat at the time of instrument deployment and instrument recovery. Images are courtesy of OOI-RCA. The gray line in each plot marks zero flow. *ROV images from 2013–2015: UW; NSF-OOI; CSSF. ROV images from 2016–2018: UW/NSF-OOI/WHOI.*

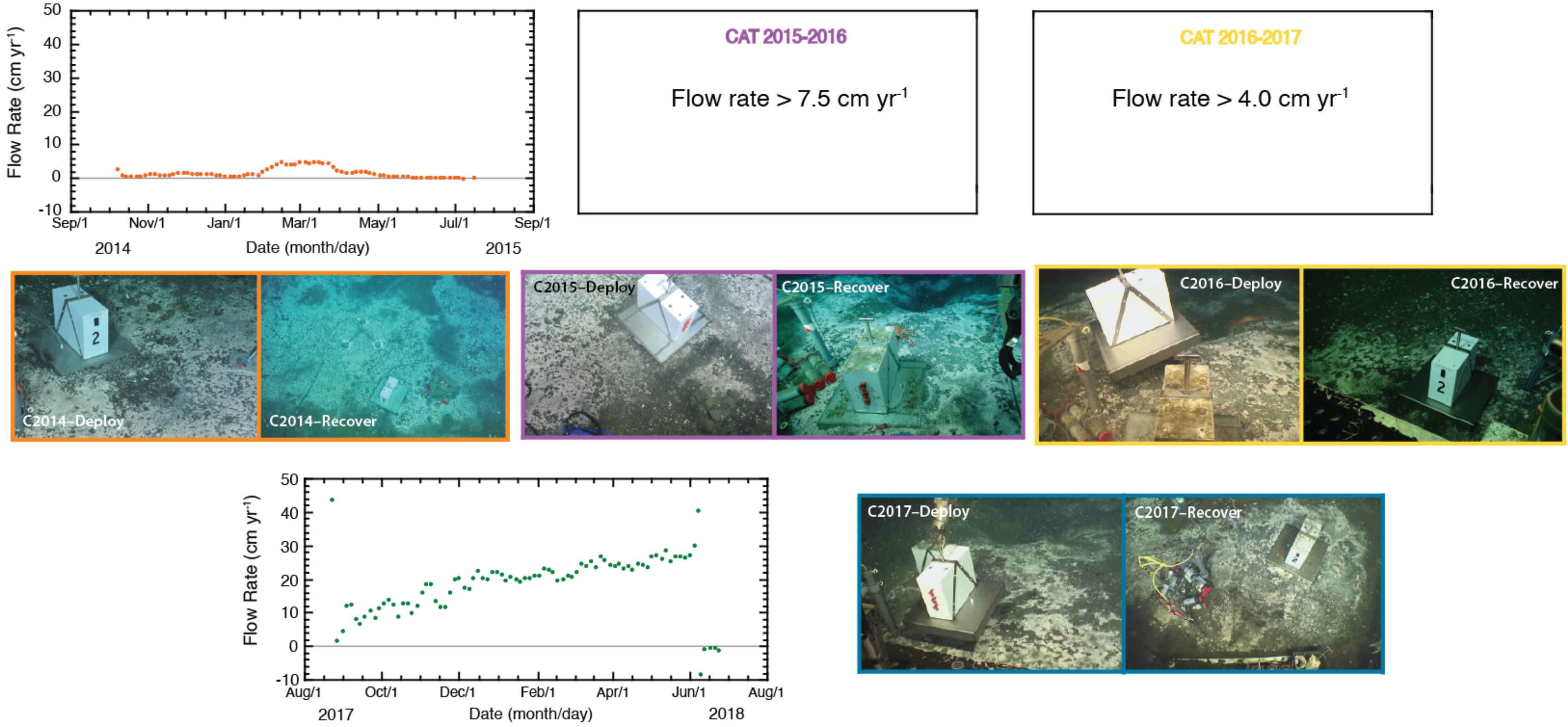

Figure 3.5. Fluid flow rates for all CAT meters deployed between Summer 2014 and Summer 2017. Flow rate plots are color matched to corresponding photos of each CAT and the bacterial mat at the time of instrument deployment and instrument recovery. Images are courtesy of OOI-RCA. The gray line in each plot marks zero flow. *ROV images from 2013–2015: UW; NSF-OOI; CSSF. ROV images from 2016–2018: UW/NSF-OOI/WHOI.*

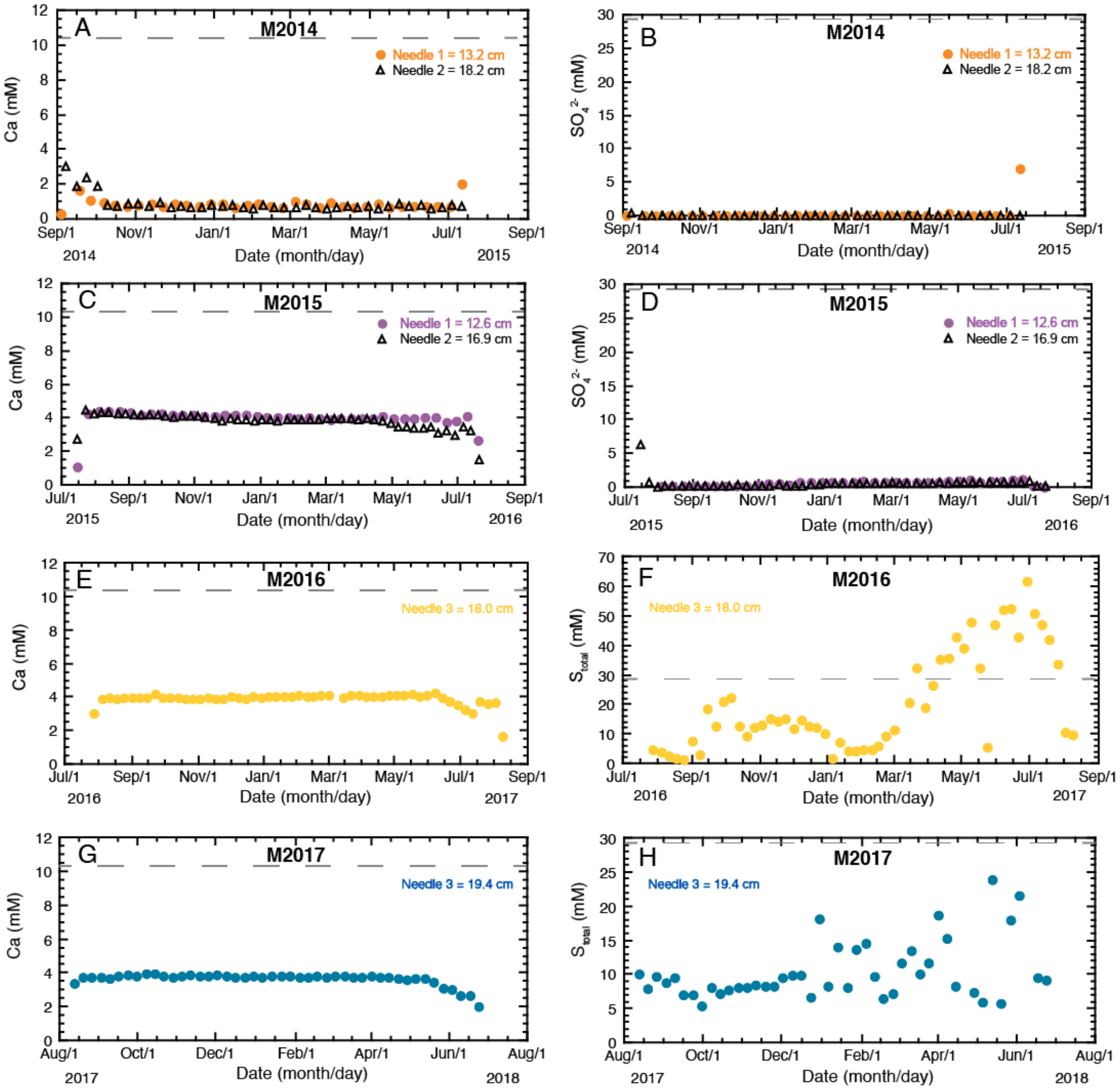

Figure 3.6. Measured calcium and sulfur for Mosquitos deployed in 2014 through 2017. (A, C, E, G) show calcium concentrations during each deployment. (B, D, F, H) show sulfate (SO_4^{2-}) or total sulfur (S_{total}) concentrations during each deployment. S_{total} is the sum of all sulfur species in the pore water ($S_{total} = SO_4^{2-} + H_2S + HS^- + S^{2-}$). Concentrations of Cl, Mg, Na, and K remained at seawater values for the duration of each instrument deployment and are shown in Figure B-2. The gray dashed line in each plot indicates seawater concentration.

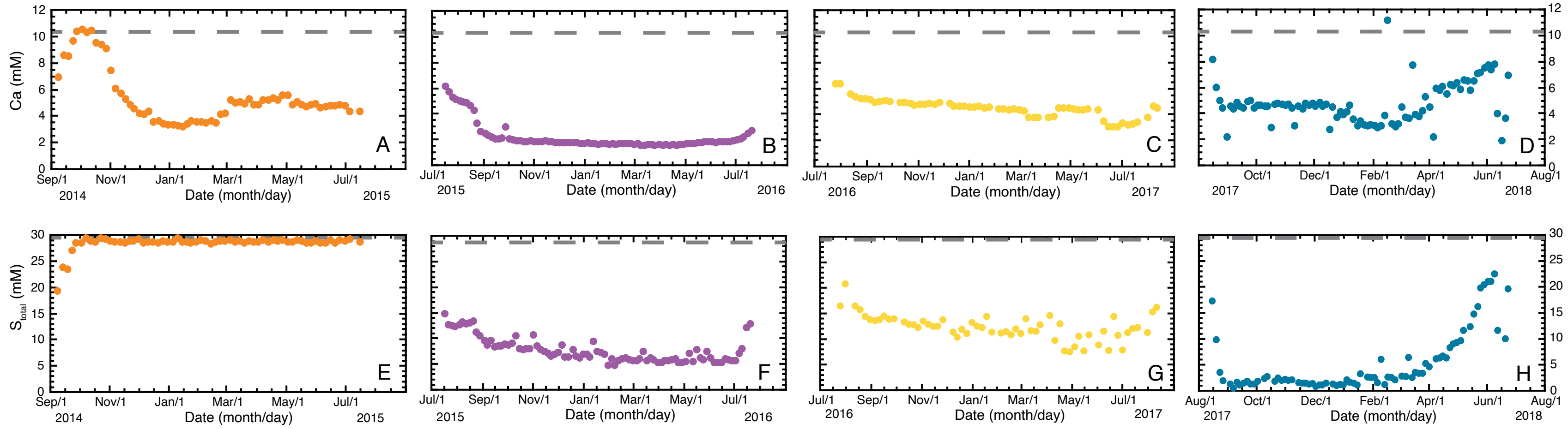

Figure 3.7. Measured calcium (A–D) and total sulfur (E–H) concentrations for CAT meters deployed in between 2014 and 2017.

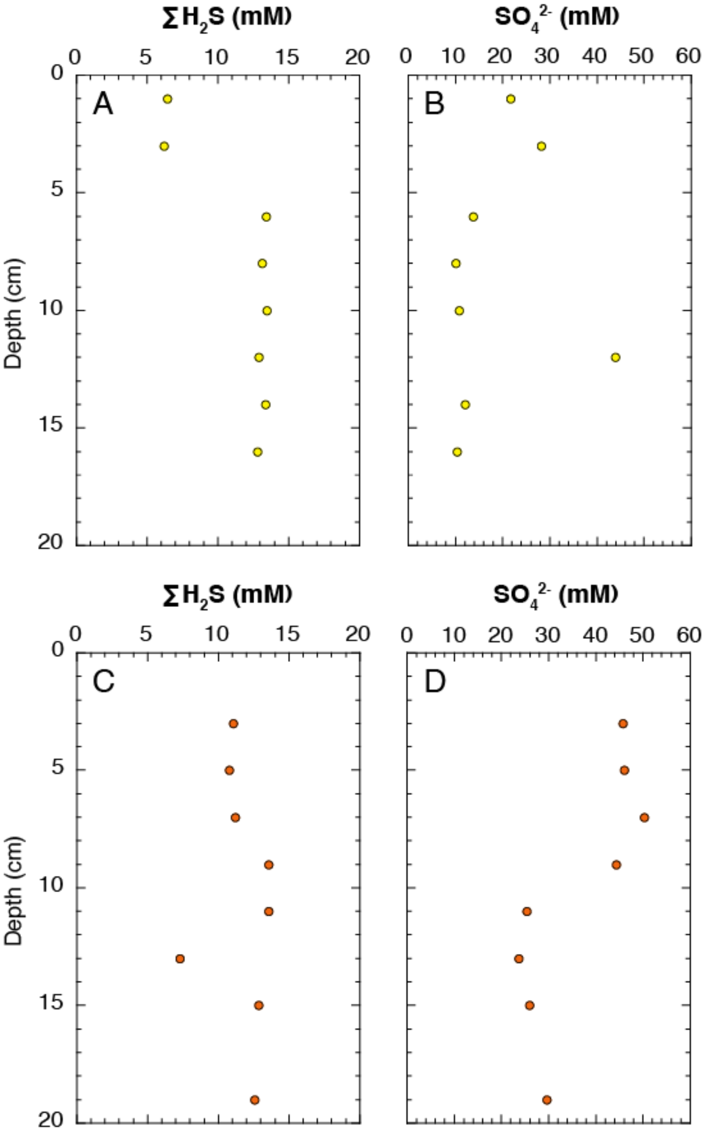

Figure 3.8. Pore water profiles of ΣH_2S and SO_4^{2-} collected from PC-1 within the footprint of Mosquito M2017 (A, B) and from PC-2 within the bacterial mat adjacent to M2017 (C, D).

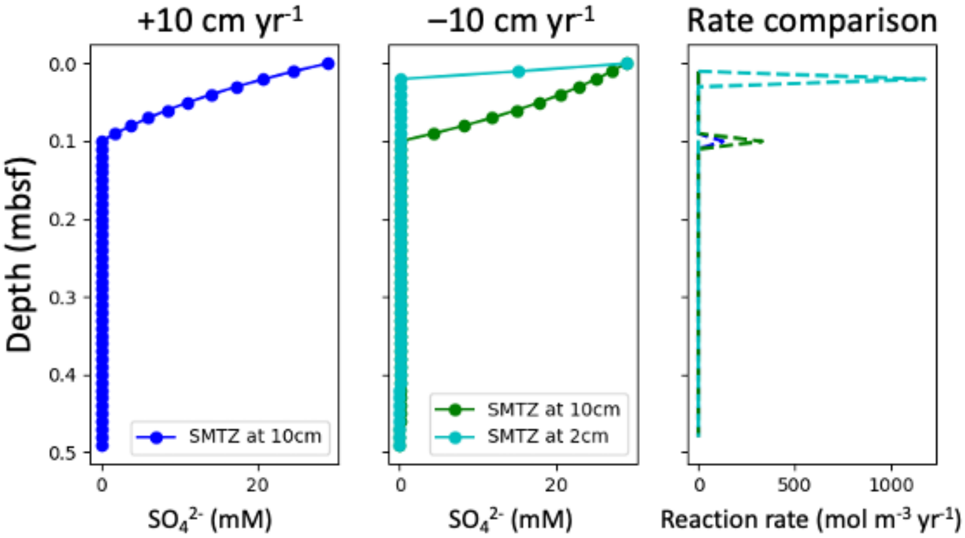

Figure 3.9. Finite element model run to steady state from seawater values assuming the SMT = 10 cm, porosity remains at a constant value of 0.7, SO_4^{2-} is only consumed by AOM and is consumed at the SMT, and the sedimentation rate is equal to 20 cm kyr^{-1}. Upward fluid flow at a rate of +10 cm yr^{-1} would result in a sulfate reduction rate (SRR) of 128 mol m^{-3} yr^{-1} (A). Downward flow of seawater at a rate of -10 cm yr^{-1} would yield a SRR of 330 mol m^{-3} yr^{-1} (B). If the SMTZ is located at 2 cm, the SRR would increase to 1171 mol m^{-3} yr^{-1} in a downward flow regime (B, C).

Year	Instrument	Net Flow Rate (cm yr^{-1})
2013-2014	M2013	-4.9
	M-2	-13.8
	CAT2013	0
2014-2015	M2014	-11.4
	CAT2014	+1.9
2015-2016	M2015	-2.75
	CAT2015	> +7.5
2016-2017	M2016	-16.1
	CAT2016	> +4.0
2017-2018	M2017	-6.5
	CAT2017	+20.5

Table 3.1. Net flow rates for each instrument deployment. Positive flow rates indicate upward flow and negative flow rates indicate downward flow.

SMT Depth	Downward Advection			Upward Advection		
	5 cm yr^{-1}	10 cm yr^{-1}	15 cm yr^{-1}	5 cm yr^{-1}	10 cm yr^{-1}	15 cm yr^{-1}
2 cm	1119	1171	1225	N/A	969	N/A
10 cm	268	330	400	167	128	96

Table 3.2. Modeled Sulfate Reduction Rates (SRR) at 5 cm yr^{-1}, 10 cm yr^{-1}, and 15 cm yr^{-1} fluid advection assuming constant porosity of 0.7, SO_4^{2-} consumption via AOM, and a constant sedimentation rate of 20 cm kyr^{-1}. SRR are presented in units of mol m^{-3} yr^{-1}.

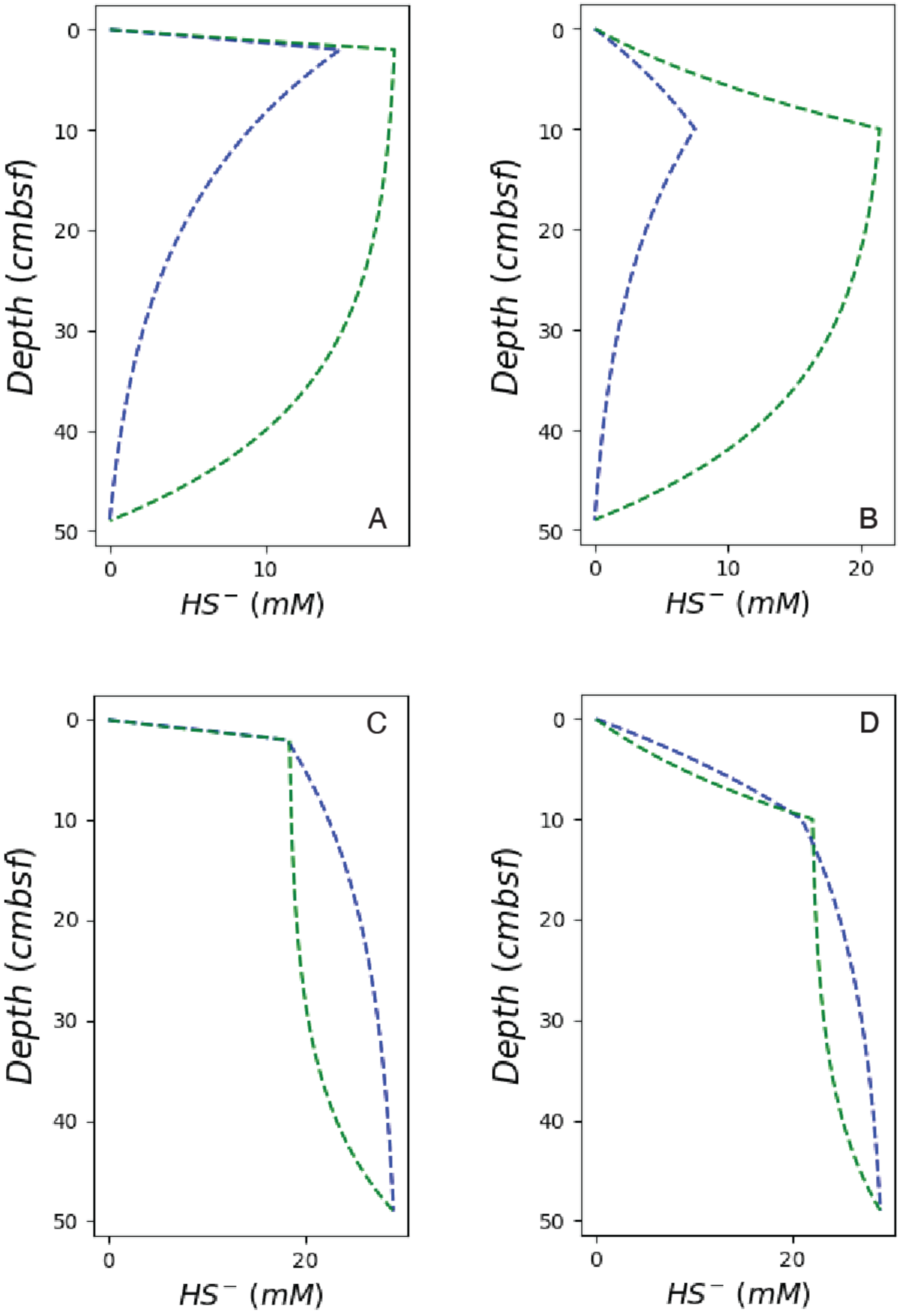

Figure 3.10. Modeled profiles of HS^- concentration assuming 10 cm yr^{-1} upward advection (blue lines) and 15 cm yr^{-1} downward advection (green lines). Profiles (A) and (B) assume that HS^- is equal to 0 mM at 50 cm with the SMT present at either 2 cm (A) or 10 cm (B). Profiles (C) and (D) assume that HS^- is equal to 28.9 mM at 50 cm with the SMT at either 2 cm (C) or 10 cm (D). Each modeled profile is set with the upper boundary as typical seawater, i.e. assuming SO_4^{2-} is equal to 28.9 mM and HS^- is 0 mM. Rates of sulfate reduction are set at the rates in Table 3.2.

Chapter 4.

Nickel bioavailability to cold seep methanotrophic communities

4.1 Introduction

Methane within continental margin sediments is produced by the fermentation of organic matter coupled to microbial reduction of CO_2 with H_2 (Equation 4.1), acetate fermentation (Equation 4.2), or the thermogenic breakdown of organic matter. The first two processes are carried out by methanogenic archaea at sediment depths below the zone of sulfate (SO_4^{2-}) reduction.

$$CO_2 + 4H_2 \rightarrow CH_4 + 2H_2O \qquad \text{(Eqn. 4.1)}$$

$$CH_3COOH \rightarrow CH_4 + CO_2 \qquad \text{(Eqn. 4.2)}$$

The microbial reduction of CO_2 is the most common methanogenic pathway in marine sediments, but acetate fermentation has been shown to occur (e.g. Heuer et al., 2009). Dissolved methane diffuses upward along a descending concentration gradient until it reaches the Sulfate-Methane Transition (SMT), where the AOM consortium of sulfate-reducing bacteria (SRB) and anaerobic methanotrophic archaea (ANME) syntrophically oxidize methane (CH_4) and reduce sulfate (SO_4^{2-}) (Equation 4.3) (Knittel and Boetius, 2009).

$$CH_4 + SO_4^{2-} \rightarrow HCO_3^- + HS^- + H_2O \qquad \text{(Eqn 4.3)}$$

Thus, the methane produced through methanogenesis below the SMT sustains shallower microbiological communities (ANME and SRB) at the SMT and the sulfidic byproduct of AOM is a critical nutrient for overlying macro- and microorganisms. Methane that escapes burial, sequestration within methane hydrate, and is not consumed via AOM is ultimately oxidized to CO_2 in the water column by aerobic methanotrophs or released to the atmosphere (Valentine et al., 2001; Mau et al., 2013).

It has traditionally been assumed that the process of AOM is efficient in oxidizing >90% of CH_4 before it reaches the water column (Knittel and Boetius, 2009), however AOM efficiency may be more variable at cold seep locations. Cold seeps are locations on the seafloor characterized by the upward advection of water and gas. A recent study by Boetius and Wenzhöfer (2013) calculated AOM filter efficiency from 41 individual locations associated with 13 cold seep regions globally and showed that filter efficiency varies from 4–100% among seep systems. Low fluid flow systems (~ <0.5 m yr^{-1}) tend to have ~80% CH_4 filter efficiency whereas systems with intermediate (approximately 0.5 m yr^{-1} – 5 m yr^{-1}) to high fluid flow rates (~ >5 m yr^{-1}) have approximately 20% efficiency (Boetius and Wenzhöfer, 2013). The authors of this study proposed that the high fluid flow rate may be a primary reason for areas of high CH_4 escape to the water column (i.e. low AOM filter efficiency). Yet fluid flow rate is a bulk umbrella underneath which may lie a more specific reason for such drastic differences in filter efficiencies. Though the AOM community at seeps is not macronutrient limited (i.e. CH_4 and SO_4^{2-}) a potential reason for this disparity may be ANME trace nutrient limitation.

ANME that couple with SRB to perform AOM are a novel type of archaea that have not been isolated in pure culture but are most closely related to *Methanomicrobiales* and *Methanosarcinales*, two methanogenic archaeal groups (Hinrichs et al., 1999; Boetius et al., 2000; Orphan et al., 2001). The archaeal taxa *Methanosarcinales* and *Methanomicrobiales* have been identified at the order level in a recent study of 26 globally distributed methane seeps, with the vast majority of *Methanosarcinales* genetic sequences associated with ANME clades (Ruff et al., 2015). There are three distinct clades of ANME that are divided into ANME-1, ANME-2, and ANME-3 clusters. ANME-1 are most closely related to *Methanomicrobiales* and ANME-2 and ANME-3 are most closely related to *Methanosarcinales*. ANME are believed to be able to share the same metabolic pathway as methanogenic archaea that generally convert CO_2 and H_2 into CH_4, though ANME perform this pathway in reverse to oxidize CH_4 into CO_2 (Kruger et al., 2003; Scheller et al., 2010; Thauer et al., 2010). However, distinct methanogenic archaea are capable of utilizing a variety of substrates in addition to CO_2 and H_2. *Methanomicrobiales* (Class II methanogens) utilize CO_2/H_2 or CO_2/formate as substrates for methanogenesis (Anderson et al., 2009), while Class III methanogens, including the *Methanosarcinales* order, are capable of metabolizing a wider range of substrates including methanol, methylamines, methyl sulfides, acetate, and CO_2/H_2 (Glass & Orphan, 2012). There are three metabolic pathways of methanogenesis depending on the substrate used: the aceticlasic pathway, the CO_2/H_2 pathway, and the methylotrophic pathway (Glass & Orphan, 2012). Given that the metabolic pathways of methanotrophy in these different ANME are the same pathways as other methanogens, it is assumed that the metabolic requirements for ANME are identical to the requirements for other methanogens. This includes similar cellular demands for trace metals in hydrogenases and cofactors for key enzymes that are essential for the performance of basic metabolic processes.

Several different metals including Fe, Ni, Co, Zn, W, and Mo are required in varying concentrations for methanogen metabolism (Glass et al., 2014; Glass and Orphan, 2012). Of these metals, Ni is of particular interest given its low abundance in the modern ocean and the high concentration necessary for methanogens (Glass and Dupont, 2017; Schönheit et al., 1979). Laboratory culture studies show that the thermophilic methanogen *Methanothermobacter thermautotrophicus*, which utilizes the CO_2/H_2 metabolic pathway, requires a trace metal nutrient stoichiometry of 500 Fe : 7.5 Ni : 1 Co : 1 Mo to carry out metabolic activity (Schönheit et al., 1979). Another CO_2/H_2 mesophilic methanogen *Methanococcus voltae* requires a slightly different stoichiometry of 33 Fe : 1 Ni : 2.1 Co (Whitman et al., 1982).

All known methanogenic metabolic pathways require Ni in varying amounts to fuel cell growth and metabolism. Each pathway utilizes a different series of metal-rich enzymes with unique Ni requirements, though each pathway converges in the final two steps that catalyze methane formation. This final step of methanogenesis, and the first step of the reverse process of methanotrophy, is dependent on the enzyme methyl-coenzyme M reductase (MCR) (Figure 4.1a) (Glass and Orphan, 2012; Jaun and Thauer, 2007) which catalyzes methanogenesis and contains the novel nickel-based cofactor F_{430} (Figure 4.1b) (Kruger et al., 2013; Thauer et al., 2010). Cofactor F_{430} encompasses 50–80% of total cellular Ni in ANME and methanogens, and is found only in methane-metabolizing archaea (Diekert et al., 1981; Mayr et al., 2008). Cofactor F_{430} content has been shown to increase on a per cell basis with increasing Ni concentrations in the cell between 75–1500 nM (Diekert et al., 1981). Schönheit et al (1979) showed that optimal growth for *Methanothermobacter thermautotrophicus* was between 200–1000 nM Ni, and that methanogen cell numbers were strongly limited at Ni concentrations less than 100 nM.

Ni follows a nutrient profile in the ocean with low surface concentrations between 2–4 nM that increase to 7–12 nM at depth. There are three primary sources of Ni to the ocean: (1) river and groundwater input of weathering products from continental crust (Gall et al., 2013), (2) atmospheric input of mineral dust and volcanic ash (Sigurdsson et al., 2007), and (3) hydrothermal vent fluids (Gall et al., 2013). Freshwater and atmospheric input account for a combined ~80% of annual Ni input to the ocean, and hydrothermal vent fluids account for ~20% (Gall et al., 2013). In the modern ocean, ~50% of dissolved Ni exists as Ni^{2+} ion, ~10% is complexed to chloride, and the remainder forms strong bonds with organic complexes (log $K_{NiL,Ni^{2+}}^{cond} > 17$) (Glass and Dupont, 2017).

In marine sediments, diagenetic processes influence the addition and removal of Ni from the dissolved phase. Ni accumulates in sediment pore water through continued burial of seawater over time. Pore water Ni concentrations can span a large range from 0–600 nM, though maximum concentrations are typically <300 nM (Klinkhammer, 1980; Shaw et al., 1990; Riedinger et al., 2014; Glass et al., 2014). The main control on nickel enrichment and depletion in pore water is the Mn and Fe redox chemistry where Ni adsorbs to manganese and iron oxyhydroxides in oxygenated sediments and is then released back into the pore water upon burial into the zone of Mn- and Fe-reduction (Klinkhammer, 1980; Riedinger et al., 2014; Shaw et al., 1990). Other reactions that consume Ni from pore water include the *in situ* alteration of volcanic ash to smectite clay (Sigurdsson et al., 1997), incorporation into iron sulfides such as pyrite (Öztürk, 1995; Little et al., 2015), and microbial uptake.

Though much is known about the adsorption and authigenic mineral incorporation of Ni in marine sediments, it is unclear how much Ni is bound in organic complexes, though estimates range between approximately 10–50% (van den Berg and Nimmo, 1987; Glass and Dupont, 2017 and references therein). The proportion of Ni bound in these organic complexes, and the binding strength of these complexes, greatly influences the bioavailability of Ni to microbial communities (Dupont et al., 2010) including methanotrophic communities.

Although the importance of Ni in the metabolic pathway of both methanogenesis and methanotrophy is well known, there are few published profiles of pore water Ni concentrations from continental margin environments where anaerobic methanogenesis and methanotrophy largely occur, and the details of Ni bioavailability in cold seep environments remains largely unknown (Glass and Orphan, 2012; Glass et al., 2014; Glass and Dupont, 2017). Pore water profiles from 15 cm push cores taken at Hydrate Ridge, a continental slope environment dominated by fluid and gas transport, show sharp increases in total Ni concentrations to a maximum value of approximately 270 nM in both clam fields and microbial mats (Glass et al., 2014). Sulfide concentrations in these same cores span a range from 5–25 mM. In strongly reduced pore water with high sulfide concentrations, nearly all Ni is complexed as the neutrally charged $Ni(HS)_2^0$ (Al-Farawati and van den Berg, 1999; Jansen et al., 2005). Free Ni (Ni^{2+}) or organically-complexed Ni dominate in low-sulfide environments, such as the open ocean. In contrast to free Ni^{2+}, neutrally charged metal-sulfide complexes, such as $Ni(HS)_2^0$, are not bioavailable due to their high stability constants and chemical inertness (Edgcomb et al., 2004). The ubiquitous presence of sulfide in high concentration and the concomitant precipitation of metal sulfide implies that the availability of metal ions, including Ni, may be limited in continental margin sediments. A potential barrier for ANME to successfully acquire enough Ni to fuel cell growth and maintenance is not only the total concentration of Ni in sediment pore water but also the bioavailability of Ni which is highly dependent on its chemical speciation. The availability is likely even lower in systems where the dominant form of sulfur is reduced hydrogen sulfide (Jaun and Thauer, 2007; Glass et al., 2014) as is expected in cold seep environments.

The upward flux of methane and rates of AOM are higher in continental margin seep environments than in any other marine environment (Reeburgh, 2007; Boetius and Wenzhöfer, 2013) and, therefore, trace metal demand may also be highest. The probability of methane emission to overlying bottom water is higher at seeps than non-seeps because of focused methane emission in both dissolved and gaseous form and the reduced efficiency of the AOM filter (Boetius & Wenzhöfer, 2013). It is possible that bioavailability of Ni may have an impact on overall AOM efficiency at a given seep. The purpose of this study is to: (1) quantify and characterize the fraction of Ni that is accessible to ANME populations in pore water at actively venting seeps and diffusive, non-seep locations, (2) probe the possibility that low methanotrophic filter efficiency at seep sites can be a result of bioavailable Ni limitation at depth, which reduces the amount of methanotrophy possible before methane escape to the water column. We expect Ni limitation is not an issue at non-seep environments where AOM is efficient, whereas Ni limitation may be prevalent at seep sites with reduced AOM efficiency. Furthermore, this study seeks to directly detect and quantify Ni-ligand complexes in pore water at seep and non-seep locations, identify the ligands binding Ni in seep environments, and determine how organic complexation may impact the bioavailability of Ni.

4.2 Materials & Methods

4.2.1 Site Descriptions & Sample Recovery

Pore water samples for this study were collected from sediment cores collected along the Hikurangi margin offshore the north island of New Zealand during two expeditions aboard the D/V *Joides Resolution* and R/V *Roger Revelle* in 2018 and 2019, respectively (Figure 4.2). In 2019, seep sites were located by the presence of bubble plumes in shipboard hydroacoustic surveys using a 12 kHz Kongsberg EM122 multibeam echosounder. Bubble plumes, or gas flares, are hydroacoustic expressions of gas expulsion from the seafloor that is typical of cold seep systems. Locations where gas flares were absent were deemed to be non-cold seep environments dominated by diffusive methane transport.

Two gravity cores were collected at cold seep environments during the 2019 SAFFRONZ cruise on the R/V *Roger Revelle* (RR1902) on the southern and northern regions of the Hikurangi margin. Gravity core BB36 was collected at a cold seep on the lower slope along the southern margin at 1995 m water depth. Gravity core BB93 was collected from an actively venting seep along the upper slope of the northern portion of the margin at 178 m water depth. A third gravity core (BB35) was collected from a non-seep location during the SAFFRONZ campaign. BB35 was cored at 2367 m water depth and spans the upper 200 cm of the sediment column. Pore water geochemistry from additional gravity cores collected within these regions validate that these cores indeed represent cold seep (BB36 and BB93) and non-cold seep (BB35) locations (Aylward et al., 2020).

Additional non-cold seep pore water samples were collected from two holes drilled during the International Ocean Discovery Program (IODP) Expedition 375. These samples were recovered from Site U1519 Holes D and E. Site U1519 is located along the northern Hikurangi margin at 1000 m water depth in a slope basin commonly known as the Tuaheni Basin. Samples from Holes D and E span the upper 23 m and 85 m of the sediment column, respectively, and were collected using an advanced piston corer system which causes minimal disturbance of sediment pore water compared to rotary coring systems used at greater depths.

During IODP Expedition 375, 20-cm whole round sediment sections from Holes D and E were transferred to a glove bag containing a titanium squeezer and pre-filled with nitrogen gas. Pore water samples were extracted from whole rounds in an anoxic environment via squeezing and filtered using 0.2 µm syringe filters within the glove bag. Aliquots for total metal analysis were acidified within the glove bag at sea with nitric acid (Optima grade, Fisher Scientific) to pH < 2 and aliquots appropriate for voltammetric analysis were left unacidified and frozen at -20ºC.

To decrease the potential for trace metal contamination during the collection of gravity cores during the 2019 SAFFRONZ expedition (BB35, BB36, BB93), two-millimeter holes were drilled into PVC core liner at 5-cm intervals and covered with electrical tape prior to coring.

Upon shipboard recovery, cores were cut into 25-cm lengths, capped, and immediately transferred to a nitrogen-filled glove bag and stored at 4ºC. Core sections were transferred to a separate nitrogen-filled glove bag at ambient temperature for pore water sampling.

Pore water was sampled at 5–10 cm depth resolution using Rhizon fluid samplers (Rhizosphere Research Products) with 0.15 µm filters that were inserted into the pre-drilled holes in the core liner. Pore water from each sampling depth was portioned within the glove bag into vials appropriate for total trace metal concentration analysis and electrochemical analysis. Total metal samples were stored unacidified at 4ºC and later acidified onshore and left to equilibrate for a minimum of 30 days. Electrochemical samples were frozen at -20ºC immediately after recovery.

Residual pore water within the core was squeezed with a hydraulic press at normal atmospheric conditions after trace metal clean sampling and passed through a 0.2 µm syringe filter. Approximately 10–20 mL of this residual pore water was portioned into two 15-mL acid cleaned bottles for LC-ICP/ESI-MS analyses and then frozen and stored at -20ºC.

All samples, with the exception of those for LC-ICP/ESI-MS, were collected under anoxic conditions and steps were taken to preserve trace metal cleanliness for total metal and electrochemical samples collected during the SAFFRONZ cruise and IODP Expedition 375. All samples were stored using equipment and storage vessels that had undergone strict acid cleaning and were stored appropriately to reduce the risk of contamination. Ultra-pure water samples were collected at different times during the sampling process to measure any potential trace metal contamination.

4.2.2 Total Trace Metal Concentrations

Trace metal samples from gravity cores obtained during the 2019 SAFFRONZ cruise were acidified using Optima grade hydrochloric acid to a pH of 1.8 to ensure all metals were in solution. The pH was measured for every IODP Site U1519 trace metal sample to confirm pH was less than 2. Each acidified sample was then diluted either 50 or 100 times in 2% trace metal grade nitric acid solution. Total dissolved metal concentrations were analyzed using a ThermoFisher Scientific iCAP-RQ inductively-coupled plasma mass spectrometer (ICP-MS) at the University of Washington (UW) TraceLab in kinetic energy discrimination (KED) mode using platinum cones, a cyclonic spray chamber and PFA nebulizer. Samples were quantified using an in-house multi-element standard created from SPEX CertiPrep single element standards. Standards used for the calibration curve were diluted with 2% trace metal grade nitric acid. Precise volumes of scandium and yttrium were added to each standard and sample to serve as internal standards. Reagent blanks were <0.39 nM for ^{60}Ni and <6.67 nM for ^{56}Fe and the detection limit was <0.81 nM for ^{60}Ni and <20 nM for ^{56}Fe. Precision for ^{60}Ni was <9.8% and < 16.8% for ^{56}Fe.

4.2.3 – Labile Ni by Cathodic Stripping Voltammetry

The ability for ANME to access Ni for growth and repair requires environmental Ni to not only be present in sufficient concentrations, but also to be in a bioavailable form. The portion of total Ni (Ni_{tot}) considered to be bioavailable is defined in this study as the labile fraction as determined by cathodic stripping voltammetry. The labile fraction includes free Ni^{2+} and Ni bound in complexes weaker than our competitive ligand, dimethylglyoxime (DMG). The fraction of Ni_{tot} bound in complexes stronger than our competitive ligand are deemed non-bioavailable and, therefore, inaccessible to ANME without some adaptation to overcome the binding strength of the Ni-ligand complex.

Labile Ni concentrations were measured via cathodic stripping voltammetry using a BASi Controlled Growth Mercury Electrode connected to a BASi Epsilon Eclipse analyzer. The method used was adapted for pore water samples based on Saito and Moffett (2001) with slight modifications from Boiteau et al (2016). Sample aliquots ranging in volume from 0.1 to 0.75 mL were placed in cleaned and conditioned 15 mL polypropylene digestion tubes with 7.5 mL ultra-pure water and 38.8 μL recrystallized dimethylglyoxime (DMG, 0.1 M) and allowed to equilibrate overnight. Just prior to analysis, 130 μL of EPPS buffer (0.5 M, N-(2-hydroxyethyl)piperazine-N-(3-propanesulfonic acid)) and 1.5 mL of sodium nitrite catalyst (1.5 M) were added to the sample dilution. Each sample was analyzed in a Teflon reaction cell and purged with ultra-high purity N_2 (>99.999%) for 300 s before being stirred during the 120 s deposition at a potential of -0.6 V followed by a 15 s equilibration period. This was followed by a linear sweep from -0.6 V to -1.4 V with a 10 V s^{-1} scan rate. Concentrations of free or weakly bound Ni were calculated using the method of standard addition, whereby triplicate scans of each sample were followed by four additions (50 pM each) of 1 mg L^{-1} Ni standard. Sample dilution was adjusted between 13x and 100x to produce a clear growth in measured current with Ni additions. Labile concentrations were defined as the proportion of total dissolved metal that was bound to DMG after the overnight equilibration period. The difference between total Ni concentration and the fraction of Ni bound to DMG represents strong organic Ni compounds with thermodynamic conditional stability constants (log $K_{NiL,Ni^{2+}}^{cond}$) greater than 17.2 ($Ni(DMG)_2$) (van den Berg and Nimmo 1987). Reagent blanks were determined using Ni-free seawater that was generated by treating UV-irradiated Station ALOHA surface seawater with cleaned Chelex-

100 beads. This seawater was then analyzed in duplicate and any measured Ni values were averaged and subtracted from total sample values. Ni was consistently undetectable in the reagent blank.

4.2.4 – Organic Ligand Quantification and Identification

Ten milliliter pore water samples were collected at 10 cm depth increments within gravity core BB93 for characterization of Ni-containing organic compounds present at an actively venting seep. Three of these samples were analyzed using liquid chromatography (LC) coupled directly to ICP-MS to determine retention times of Ni-containing compounds and to quantify the Ni associated with organic complexes. The same chromatography was then coupled to electrospray ionization mass spectrometry (ESI-MS) to identify masses and potential fragmentation patterns of these same compounds.

Before analysis, samples were preconcentrated by passing through trace metal clean Bond Elut columns (1 g ENV, 6ml, Agilent) at a constant flow rate of 18 mL/min. Prior to use, all columns were cleaned with two column volumes of ultra-pure water acidified to pH 2 and an additional two column volumes of ultra-pure water, then activated with one column volume of trace metal clean methanol. Columns were then washed with two column volumes of ultra-pure water and stored at -20ºC. This method of column preconcentration is designed to concentrate secondary metabolites, or biomolecules produced by microorganisms, so that there is greater confidence that the organic Ni complexes measured are microbial in nature (Boiteau et al., 2013).

Compounds in each sample were separated in time using a Dionex Ultimate 3000 LC system equipped with a polyetheretherketone (PEEK) C18 column (4.2 x 150 mm, 3 µm, Agilent

Technologies). Two solvents were used for chromatographic separation, referred to here as Solvent A and Solvent B; Solvent A: ultrapure water with 5 mM ammonium formate; Solvent B: trace metal clean methanol with 5 mM ammonium formate in distilled methanol. Samples were separated at a flow rate of 50 µL/min at 30ºC and a 20-minute gradient of 5% to 90% Solvent B. This was followed by a 10-minute isocratic step of 90% Solvent B and then a 15-minute step at 5% Solvent B to condition the column prior to injecting the next sample. This same chromatography was used for both LC-ICP-MS and LC-ESI-MS analyses of each sample.

After LC separation, samples were injected into the ICP-MS equipped with a PFA-ST nebulizer (Elemental Scientific) and platinum sample and skimmer cones. Samples were introduced at a flow rate of 50 µL/min and a spray chamber kept at 2.7ºC. Measurements were made using kinetic energy discrimination mode (KED) with 3.8–4.0 mL/min flow rate of helium collision gas and 10% O_2 gas to prevent precipitation of the solvents on the cones. ^{60}Ni peaks were identified in the output using in-house R scripts (Boiteau et al., 2016).

After determining retention times of Ni-containing compounds with the ICP-MS, the same chromatography was used to further identify masses and potential fragmentation of these same compounds using a hybrid quadrupole Q-Exactive HF Orbitrap (Thermo Scientific) at the University of Washington. The spray voltage was set to 3.5 kV with capillary temperature of 320ºC, sheath gas level setting of 16, auxiliary gas setting of 3, and sweep gas setting of 1. The auxiliary gas heater temperature was kept at 90ºC, and the S-lens RF level was set to 65. The mass-to-charge ratio (*m/z*) of all compounds were monitored in positive mode and MS^1 scans were collected using 120,000 mass resolution, *m/z* range of 200–2000, AGC target of $1x10^6$, and a maximum injection time of 100 ms. Abundant, recurring compounds were also fragmented to aid in further identification. Fragmentation data (MS^2 data) were collected in data-dependent mode (dd-MS^2) with 30,000 mass resolution, an isolation window of 1.0 m/z, AGC target of $2x10^4$, 100 ms maximum injection time, and 35% collision energy. Our untargeted search for Ni-containing compounds was guided by the MS^1 spectra and Ni-containing compounds from the LC-ICP-MS data. Raw data files were converted to mzXML file format using MSConvert (Proteowizard) and processed using in-house R scripts including the XCMS package (Boiteau et al., 2016) to putatively identify potential Ni compounds in each sample based on the presence of ^{60}Ni and ^{58}Ni.

Fragmentation data were searched against a publicly available online database to identify Ni-containing compounds (METLIN). Molecular formulas for each compound were also calculated (www.chemcalc.org) in another effort to characterize the *in situ* Ni-containing molecules. Only putative compounds where MS^2 data was collected were considered for this study. All other compounds that were found to contain Ni but do not have associated fragmentation data are presented in Appendix C (Table C-1). Putative molecular formulas presented here are only those that have exact matches to measured MS^1.

4.3 Results and Discussion

4.3.1 – Total Ni in Seeps and Non-Seeps

Total nickel (Ni_{tot}) concentrations from non-seep locations in the north (Site U1519, Holes D and E) and the south (BB35) of the Hikurangi margin show elevated metal concentrations at shallow depths relative to average bottom water concentrations (Figure 4.3). Ni_{tot} concentrations from Holes D and E vary significantly from average bottom water concentrations within the upper 2 m of sediment (Figure 4.3) with concentrations of 59.4 nM and 57.8 nM, respectively. Total concentrations increase to a shallow maximum of 221.7 nM Ni at 4 m depth at Hole D. This increase in pore water Ni aligns with a layer of volcanic ash in the core that is otherwise dominated by mud (Barnes et al., 2019). Below 4 m depth, Ni concentrations decrease to values between 12.9 and 56.1 nM then climb to a second, deeper maximum concentration of 136.3 nM at 15 meters below seafloor (mbsf). The Ni_{tot} shows a similar profile at Hole E, just 20 m away, where concentrations decline with depth to a minimum of 34.1 nM before reaching a subsurface maximum of 136.4 nM at 13.6 mbsf. The two subsurface maxima between 13 and 15 mbsf within these cores occur below the SMT (Barnes et al., 2019).

Ni_{tot} is similarly enriched within the upper 5 cm of BB35 to a value of 108.0 nM. Ni_{tot} decreases with depth to values between 13.1 nM and 49.8 nM then increases drastically to 137.4 nM at 1.6 m depth. The high concentration of Ni_{tot} in the shallow subsurface indicates a strong diffusional gradient of dissolved Ni to bottom water.

Ni_{tot} profiles at the two actively venting seeps sampled in this study show markedly different trends compared to the non-seep sites. An actively venting seep in the southern margin sampled with gravity core BB36 shows strong variation in Ni_{tot} concentration with depth (Figure 4.3). Downcore Ni_{tot} values fluctuate within a narrower range than the non-seep sites, from a minimum concentration of 13.1 nM to a maximum of 37.3 nM, an order of magnitude lower than at non-seep sites. BB93 from the northern margin contained concentrations <21 nM just below the seafloor that decrease to a minimum of 11 nM at 0.55 mbsf and then climb to a maximum of 41.5 nM at 2.55 mbsf. Maximum Ni_{tot} concentrations in these two cores from advective locations are less than 42 nM whereas maximum Ni_{tot} from each non-seep site are greater than 130 nM, indicating that actively venting seep locations have a smaller reservoir of Ni for potential microbial utilization.

The whole cell Ni requirement for ANME is still largely unknown. It is difficult to ascertain these metal requirements based solely on counting the Ni atoms of individual enzymes necessary to run a given metabolic pathway because (1) shifts in cellular enzyme ratios will depend on each enzyme's affinity (K_m value) for its respective substrate, (2) we do not always know which ANME clade is dominant in a given environment and therefore which metabolic pathway is most utilized, and (3) substitutions enacted by the microbe to deal with nutrient limitations will alter overall Ni needs. For example, all methanogens use Ni-Fe hydrogenases (Thauer et al., 2010), but *Methanomicrobiales* (most closely related to ANME-1) has adapted to deal with Ni starvation by augmenting at least one hydrogenase to be Ni-free and, thus, decrease their total Ni requirement (Afting et al., 1998). This adaptation likely explains why shifts in the dominant archaeal methanogen species has been observed under Ni depletion in anaerobic bioreactor studies. In one study of the impacts of individual trace metal limitation on CH_4 production in a wheat stillage biogas reactor, Ni limitation led to a shift in methanogen population from *Methanosarcinales* (most closely related to ANME-2 and ANME-3) dominance to *Methanomicrobiales* dominance over the 2-year study period (Gustavsson et al., 2013). Based on the Gustavsson et al. (2013) study results, ANME-2 and -3 likely dominate under Ni-rich conditions. This inferred variability in Ni requirements between clades has been demonstrated in the few experiments that have been conducted that sought to define trace metal requirements in pure cultures of methanogenic archaea, but this has not been explored in cold seep environments.

Growth experiments conducted on a wide range of anaerobic methanogens utilizing a variety of substrates found optimal growth conditions of 200–1000 nM Ni_{tot} (CO_2/H_2 substrate, *Methanococcus voltae* and *Methanothermobacter thermautotrophicus*, respectively; Whitman et al., 1982; Schönheit et al., 1979), 2000 nM Ni_{tot} (acetate substrate, *Methanothrix soehngenii*;

Fathepure, 1987), and 100 nM Ni_{tot} (methanol substrate, *Methanosarcina barkeri*; Scherer and Sahm, 1981) in experiments with similar cell densities. From these pure culture studies, we can infer that metabolisms using methanol substrates require less Ni than acetate and that thermophilic methanogens utilizing CO_2/H_2 (*M. thermautotrophicus*) require more Ni than mesophilic methanogens utilizing the same substrate (*M. voltae*), implying that increased temperature may increase the trace metal requirement.

Measurements of Ni_{tot} in marine pore waters remain sparse. Ni_{tot} concentrations collected from shallow pore waters at Southern Hydrate Ridge range from 0.5 nM to 270 nM below an active seep and 8–54 nM in pore waters of a non-seep, low methane flux site (Glass et al., 2014). Pore water measurements within 8.5 m and 10 m gravity cores from the Argentine Basin fall within the published range for cold seep pore waters, from approximately 5 nM to 110 nM (Riedinger et al., 2014). Interestingly, our data show the reverse trends whereby the non-seep locations we studied (Site U1519 and BB35) showed higher overall concentrations of Ni_{tot} with depth compared to advective seep sites (BB36 and BB93).

Differences in Ni enrichment between locations in this study and those in the Argentine Basin and Southern Hydrate Ridge may be due to ANME and methanogen community utilization. It is possible that the non-seep (or diffusion-dominated) locations in our study sites have higher Ni_{tot} concentrations because of a smaller microbial community and therefore less Ni is consumed from pore water. Our seep profiles can then be interpreted as having larger archaeal communities and, therefore, pore water Ni is drawn down. Only specific horizons within the non-cold seep locations cored in this study have Ni_{tot} concentrations that meet the lowest optimal Ni concentration of 100 nM (Scherer and Sahm, 1981) required to support metabolic function (Figure 4.3).

4.3.2 – Ni Bioavailability in Seeps and Non-Seeps

Differences in the labile Ni fraction were apparent between those sites with and without active fluid advection. The labile Ni fraction from diffusive Site U1519 holes ranges from 10–90% of the Ni_{tot} pool (Figure 4.4). Conversely, only approximately 3–36% of Ni_{tot} within active seep site BB36 pore water is bioavailable. The remaining 64–97% of the Ni_{tot} measured in the pore water is bound to complexes stronger than our competing ligand, DMG (log $K_{NiL,Ni^{2+}}^{cond} >$ 17.2). In BB93, another active seep site, the Ni_{tot} concentration increases while the labile fraction decreases, so that the percentage of Ni associated with strong complexes increases with depth. On average, 36.6% of the Ni_{tot} pool at diffusive non-seep sites in this study is bioavailable while only 15.2% of the Ni_{tot} pool at active seep sites is bioavailable. This larger fraction of bioavailable Ni at diffusive sites compared to actively venting sites could be due to several reasons. There could be less draw-down of labile Ni in non-seep sites due to a smaller microbial community, lower sulfide concentrations leading to higher concentrations of bioavailable Ni, or less strong organic complexation of Ni at non-seep sites leading to higher concentrations of labile Ni. For this study, we have no information on any potential differences in the methanogen community between our non-seep and active seep sites, so we are not able to assess whether the differences in bioavailable Ni we observed are related to differences in the size of the microbial community at each site. In the remaining sections we will discuss how the presence of sulfide and/or organic compounds may impact the differences in bioavailable Ni observed between sites, and how this might impact the microbial community.

4.3.3 – The Impact of Sulfide on Ni Bioavailability

The bioavailability of Ni in sulfide-rich pore water is likely controlled by several factors, including metal-sulfide precipitation, the solubility of neutral metal-sulfide complexes (Emerson et al., 1983) and complexation with organic matter (Gardiner, 1974). Free, non-complexed Ni (Ni^{2+}) is thought to be the most bioavailable, while Ni-sulfides and Ni associated with strong organic complexes are thought to be less bioavailable, but their true bioavailability to different microbes is unknown. For example, there is indirect evidence that some methanogens are able to directly access Ni from soluble sulfide complexes (Jansen et al., 2007). In mixed anaerobic bioreactor cultures amended with Ni, addition of Ni stimulated methanogenesis despite 95% of the dissolved Ni being present in sulfide complexes (Jansen et al., 2005). Since the bioavailable fraction of Ni at all of the sites in this study is insufficient to maintain optimal growth and metabolism, either ANME or their SRB partners may be able to directly access Ni from sulfide or strong organic complexes.

4.3.4 – The Impact of Strong Organic Nickel Complexes on Ni Bioavailability

To probe how ANME may be acquiring non-labile Ni in cold seep locations, we sought to quantify and characterize the organic Ni-binding ligands in pore water to determine whether production of extracellular Ni-binding ligands might be a strategy employed by the microbial community to enhance Ni availability and uptake. This strategy is common in other organisms for the acquisition of trace metals. For example, the marine sediment SRB *Desulfococcus multivorans* is capable of producing extracellular ligands to reversibly bind copper and irreversibly bind zinc in culture to manage metal uptake (Bridge et al., 1999). The Ni requirement for SRB involved in AOM is not well constrained, but some SRB possess Ni-Fe hydrogenases (Pereira et al., 2011). Marine heterotrophic bacteria also produce organic Fe-binding ligands in order to mobilize Fe from mineral phases (Vraspir and Butler, 2009). It is possible that one or both organisms involved in AOM may produce extracellular ligands to bind Ni to meet metabolic needs, or to extract Ni from Ni-sulfide complexes. While our CSV measurements provide the fraction of Ni_{tot} that was strongly complexed, it could not be determined from that measurement alone how much of the strongly complexed Ni was in Ni-sulfide versus organic Ni complexes.

LC-ICP-MS was used to detect the abundance of organic ligands complexed to Ni in the pore water of three depths within the active seep BB93 gravity core. In the resulting ICP-MS chromatograms, peaks in signal intensity for ^{60}Ni are representative of organic compounds that were isolated by our solid phase extraction step and are complexed to Ni. Retention time gives an indication of polarity of the eluted compounds, whereby more polar molecules are eluted earlier in each chromatogram. The largest Ni peaks were observed early in the chromatography, suggesting that many of the observed organic Ni ligands are relatively small (200-600 Da) and polar. The chromatography is optimized for microbially-produced ligands rather than humic-like compounds, organic degradation products, or abiotically-produced small molecules, indicating that many of the organic compounds detected are likely discrete ligands that are microbial in nature (Boiteau et al. 2013).

To quantify the fraction of strongly complexed Ni that was due to organic complexation, we first integrated the area beneath each ^{60}Ni chromatogram and corrected for background Ni contained in the reagents and solvents. Each area was normalized to counts from in-house Fe standards and an Fe/Ni sensitivity ratio to account for differences in the ionization of Ni relative to the organic compound standard which contained Fe (ferrioxamine E; Boiteau et al. 2016). This corrected Ni area was then converted to a concentration and corrected for pore water volume.

The concentration of organically complexed Ni in each sample that was resolved by our solid phase extraction column is shown in Table 4.1. In general, the percentage of organically complexed Ni increases with depth, and the majority of Ni_{tot} is bound in strong organic complexes at every depth that was sampled in this active seep site. Assuming this LC-ICP-MS method is detecting only those ligands that are strongly complexing Ni, and knowing that the method of sample preparation concentrates ligands that are likely microbially produced, then the subsurface microbial population is saturating pore water with Ni-binding ligands at all depths.

Metal-binding ligand secretion could have several functions, and it might differ between the ANME and SRB communities. For example, microbes in the water column are known to compete for the scarce nutrient Fe by secreting siderophores, which are very strong organic ligands that can solubilize Fe from mineral phases and keep Fe in solution above its inorganic solubility limits (Vraspir and Butler, 2009). Heterotrophic bacteria and fungi are the known producers of these ligands, and they also possess the necessary cellular receptors to take up the Fe-siderophore complex after secretion. In some microbial consortia, for example heterotrophic bacteria associated with *Trichodesmium* colonies, the heterotrophic bacteria are able to produce and take-up Fe-siderophore complexes, but the *Trichodesmium* is not (Roe et al. 2012). Thus, strong ligand production by the associated heterotrophs (e.g. SRB) may be a mechanism for competing for this scarce resource. It is unknown whether the presence of Ni-binding organic ligands enhances or diminishes the bioavailability of Ni to the microbial community at the sites sampled in this study, or whether ANME or SRB might be producing these ligands to compete with the other for Ni.

From this dataset, we cannot determine whether these organic Ni ligands are released from cells during cell lysis, desorbed from mineral phases, or being actively produced by the *in-*

situ microbial community. However, it is possible that organic Ni ligands may be actively produced by the seep community in an effort to acquire trace metals necessary to run one of the most metal-rich metabolisms known in the modern biosphere (Zerkle et al., 2005).

In an effort to determine whether the Ni ligands observed are being actively produced by the microbial community, we identified the masses and chemical formulas of Ni-containing organic ligands using specific retention times and *m/z* ratios determined from the LC-ICP-MS traces. Intensities from MS^1 scans were normalized to the most abundant mass in the spectra from each sample. We found 14 unique Ni-containing ligands across the three samples that were identified using Ni isotope search algorithms, confirming that each compound contained a Ni atom, and calculated their putative chemical formulas (Table 4.2). Only one putative ligand was detected in all three samples (Figure 4.5). This compound has a *m/z* of 330.914 and eluted at 3.71 minutes. Two additional masses were identified in at least two samples from different depths. All other detected masses were unique to each sample, illustrating that a range of organic Ni compounds exist in pore waters.

Many of the putative chemical formulas calculated for the compounds identified contain sulfur, similar to Ni compounds identified in surface ocean waters (Boiteau et al. 2016). Of all of the possible chemical formulas that fit the data, 84% require sulfur to exactly match the measured *m/z*. In the shallowest sample from BB93, 82% of calculated formulas require S to exactly match the *m/z* data. Mid-depth in the core, at 140 cm, 100% of compounds require S, and in the deepest sample at 270 cm, 86% of compounds require S.

Mass-to-charge ratios from MS^1 spectra were used to guide our untargeted search for molecular fragments that could be compared to known databases in an attempt to more definitively identify the organic ligands binding Ni in pore water. Three fragments that were found in multiple compounds matched known fragments within 10 ppm mass difference (Table 4.3). One of these fragments with *m/z* of 204.96 is an exact match for dimercaptosuccinic acid ($C_4H_6O_4S_2$) (DMSA) meaning that the ligand we identified in our sample has the same functional groups and the same *m/z* of DMSA. Dimercaptosuccinic acid is a synthetic compound known to strongly complex lead, mercury, arsenic, and cadmium (Aposhian, 1983). Major functional groups in DMSA include carboxylic acid and thiol which are functional groups common in metal-binding ligands found in the ocean (e.g. Gorman-Lewis et al., 2014; Boiteau et al., 2016; Bundy et al., 2018). Measurement of this particular fragment in association with some of our organic Ni-containing compounds provides additional evidence that subsurface microbes may be intentionally secreting trace metal-specific ligands to enhance bio-uptake or in response to metal toxicity. As is common with marine organic ligands, the vast majority of our putative Ni compounds did not have exact matches to compounds and their fragments in public databases, thus precluding the definitive identifications of the organic Ni compounds we observed (Boiteau et al. 2016; Bundy et al. 2018). The paucity of metal compounds in fragmentation databases is a barrier to identification of any potentially novel metal-binding ligands that may be excreted by subsurface microorganisms for metal acquisition.

4.3.5 – Future Directions

To date, we are unaware of published studies identifying or characterizing microbial ligands in continental margin sediments yet there is little doubt that ANME, or their SRB partners, must secrete extracellular ligands to acquire Ni from pore water at actively venting seep sites where bioavailable Ni is drastically reduced compared to non-seep sites. Metagenomic analysis from shallow Hydrate Ridge sediments identified Ni^{2+} transporter genes belonging to

ANME within cold seep pore water (Glass et al., 2014), yet data from our study show that very little of the Ni_{tot} present is likely to be present as Ni^{2+}. Microbes may use Ni ligands to solubilize Ni from mineral phases and keep Ni in solution, and then dissociate Ni from the ligand prior to uptake. Comparison of these organic Ni compounds to those in other seep and non-seep settings would aid in further elucidating this unknown.

From the data presented in this paper, we propose that trace metal limitation, specifically Ni limitation, may indeed have an impact on AOM filter efficiency. It is likely that the AOM community is larger in seep locations compared to non-seep locations and the seep community consumes the bioavailable pool of Ni much faster than non-seep communities where rates of AOM are lower. The bioavailable fraction of Ni at active seep locations in this study was less than half of the bioavailable fraction at non-seep locations. When the rate of community growth and Ni utilization outpaces the supply of bioavailable Ni, there may be a threshold below which the scarcity of bioavailable Ni in the environment induces ANME, or SRB, to produce extracellular Ni-binding ligands in order to meet cellular demands. This production likely comes at a high energetic cost and may be less efficient than transporting readily bioavailable Ni into the cell. As such, bioavailable Ni limitation at seep settings could induce lower AOM filter efficiency due to the energetic cost of famine-induced ligand production.

4.4 Conclusion

This study is the first of its kind to measure the bioavailability of Ni in marine pore water as well as quantify and characterize organic Ni-binding ligands. The results shown herein support the hypothesis that higher concentrations of bioavailable Ni exist at non-cold seep settings compared to cold seep settings where there is greater uptake and utilization of Ni from pore water to fuel ANME metabolism. Cold seep environments tend to have a greater depletion of Ni_{tot} and less than half of the average bioavailable Ni present at non-seep locations. This relative depletion of bioavailable Ni in cold seep settings where ANME communities thrive should lead to a diminished capacity of AOM to oxidize CH_4 before release to the water column in the absence of an evolutionary adaptation for ANME to acquire non-bioavailable Ni from strong organic complexes, such as extracellular ligand production. Though this study cannot determine if, or identify which, extracellular ligands may be released into pore water from ANME or their SRB partners to acquire Ni, the data demonstrates the abundant diversity of microbially produced ligands that complex Ni in cold seep sediments. One or some of these may be key to ANME Ni acquisition. Future isolation of extracellular ligands will benefit from the involvement of coupled geochemical and microbiological studies. This study serves as a foundation for more investigations that measure the bioavailability of essential metals for ANME to understand (1) evolutionary adaptations to nutrient availability, (2) the role metal acquisition plays in the health of AOM consortia and efficiency of CH_4 consumption, and (3) the effect subsurface complexation of trace metals has on nutrient exchange with the water column. Additionally, this study uncovered the large diffusional gradients of Ni from the shallow sediment of both seep and non-seep settings to seawater. The bulk of the Ni pool is strongly complexed in organic compounds that might be an important source of complexed Ni to the global ocean.

4.5 References

Afting, C., Hochheimer, A., and Thauer, R. (1998) Function of H_2- forming methylenetetrahydromethanopterin dehydrogenase from *Methanobacterium thermautotrophicum* in coenzyme F_{420} reduction with H_2. *Archives of Microbiology* **169**: 206-210.

Al-Farawati, R. and van den Berg, C.M. (1999) Metal-sulfide complexation in seawater. *Marine*

Chemistry **63**: 331-352.

Anderson, I., Ulrich, L.E., Lupa, B., Susanti, D., Porat, I., Hooper, S.D., Lykidis, A., Sieprawska-Lupa, M., Dharmarajan, L., Goltsman, E., Lapidus, A., Saunders, E., Han, C., Land, M., Lucas, S., Mukhopadhyay, B., Whitman, W.B., Woese, C., Bristow, J., Kyrpides, N. (2009) Genomic Characterization of Methanomicrobiales Reveals Three Classes of Methanogens. *PLoS One* **4**(6): 1-9.

Aposhian, H.V. (1983) DMSA and DMPS—Water Soluble Antidotes for Heavy Metal Poisoning. *Annual Review of Pharmacology and Toxicology* **23**: 193-215.

Aylward, I.E., Solomon, E.A., Torres, M.E., Whorley, T.L., Harris, R.N., Hillman, J., Philip, B.T. (2020) Geochemical Constraints on the Hikurangi Margin Hydrogeologic System – Results from the SAFFRONZ Expedition. *American Geophysical Union Fall Meeting*.

Barnes, P.M., Wallace, L.M., Saffer, D.M., Pecher, I.A., Petronotis, K.E., LeVay, L.J., Bell, R.E., Crundwell, M.P., Engelmann de Oliveira, C.H., Fagereng, A., Fulton, P.M., Greve, A., Harris, R.N., Hashimoto, Y., Hüpers, A., Ikari, M.J., Ito, Y., Kitajima, H., Kutterolf, S., Lee, H., Li, X., Luo, M., Malie, P.R., Meneghini, F., Morgan, J.K., Noda, A., Rabinowitz, H.S., Savage, H.M., Shepherd, C.L., Shreedharan, S., Solomon, E.A., Underwood, M.B., Wang, M., Woodhouse, A.D., Bourlange, S.M., Brunet, M.M.Y., Cardona, S., Clennell, M.B., Cook, A.E., Dugan, B., Elger, J., Gamboa, D., Georgiopoulou, A., Han, S., Heeschen, K.U., Hu, G., Kim, G.Y., Koge, H., Machado, K.S., McNamara, D.D., Moore, G.F., Mountjoy, J.J., Nole, M.A., Owari, S., Paganoni, M., Rose, P.S., Screaton, E.J., Shankar, U., Torres, M.E., Wang, X., and Wu, H.-Y., 2019. Site U1519. *In* Wallace, L.M., Saffer, D.M., Barnes, P.M., Pecher, I.A., Petronotis, K.E., LeVay, L.J., and the Expedition 372/375 Scientists, *Hikurangi Subduction Margin Coring, Logging, and Observatories.* Proceedings of the International Ocean Discovery Program, 372B/375: College Station, TX (International Ocean Discovery Program). https://doi.org/10.14379/iodp.proc.372B375.104.2019

Boietius, A., Ravenschlag, K., Schubert, C.J., Rickert, D., Widdel, F., Gleseke, A., Amann, R., Jørgensen, B.B., Witte, U., Pfannkuche, O. (2000) A marine microbial consortium apparently mediating anaerobic oxidation of methane. *Nature* **407**: 623-626.

Boetius, A. and Wenzhöfer, F. (2013). Seafloor oxygen consumption fuelled by methane from cold seeps. *Nature Geoscience* **6**(9) 725-734.

Boiteau, R.M., Fitzsimmons, J.N., Repeta, D.J., Boyle, E.A. (2013) Detection of iron ligands in seawater and marine cyanobacteria cultures by high-performance liquid chromatography–inductively coupled plasma-mass spectrometry. *Analytical Chemistry* **85**(9): 4357-4362.

Boiteau, R.M., Till, C.P., Ruacho, A., Bundy, R.M., Hawco, N.J., McKenna, A.M., Barbeau, K.A., Bruland, K.W., Saito, M.A., Repeta, D.J. (2016), Structure characterization of natural nickel and copper binding ligands along the US GEOTRACES Eastern Pacific Zonal Transect. *Frontiers in Marine Science* **3**: 1-16

Bridge, T.A.M., White, C., Gadd, G.M. (1999) Extracellular metal-binding activity of the sulphate-reducing bacterium *Desulfococcus multivorans*. *Microbiology* **125**: 2987-2995.

Bundy, R.M., Boiteau, R.M., McLean, C., Turk-Kubo, K.A., McIlvin, M.R., Saito, M.A., Van Mooy, B.A.S., Repeta, D.J. (2018) Distinct siderophores contribute to iron cycling in the mesopelagic at station ALOHA. *Frontiers in Marine Science* **5**: 1-15.

Diekert, G., Konheiser, U., Piechulla, K., Thauer, R.K. (1981) Nickel requirement and factor F_{430} content of methanogenic bacteria. *Journal of Bacteriology* **148**(2): 459-464.

Dupont, C.L., Buck, K.N., Palenik, B., Barbeau, K. (2010) Nickel utilization in phytoplankton asemblages from contrasting oceanic regimes. *Deep-Sea Research, Part 1* **57**(2010): 553-566.

Edgcomb, V.P., Molyneaux, S.J., Saito, M.A., Lloyd, K., Böer, S., Wirsen, C.O., Atkins, M.S., Teske, A. (2004) Sulfide Ameliorates Metal Toxicity for Deep-Sea Hydrothermal Vent Archaea. *Applied and Environmental Microbiology* 2551-2555.

Emerson, S., Jacobs, L., and Tebo, B. (1983) The behavior of trace metals in marine anoxic waters: solubilities at the oxygen-hydrogen sulfide interface. In *Trace Metals in Sea Water*. Wong, C.S., Boyle, E., Bruland, K.W., Burton, J.D., and Goldberg, E.D. (eds). *NATO Conference Series*. Springer US, pp. 579-608.

Fathepure, B.Z. (1987) Factors Affecting the Methanogenic Activity of *Methanothrix soehngenii* VNBF. *Applied and Environmental Microbiology* **53**(12): 2978-2982.

Gall, L., Williams, H.M., Siebert, C., Halliday, A.N., Herrington, R.J., Hein, J.R. (2013) Nickel isotopic compositions of ferromanganese crusts and the constancy of deep ocean inputs and continental weathering effects over the Cenozoic. *Earth and Planetary Science Letters* **375**: 148-155.

Gardner, L.R. (1974) Organic versus inorganic trace metal complexes in sulfidic marine waters: some speculative calculations based on available stability constants. *Geochimica et Cosmochimica Acta* **38**: 1297-1302.

Glass, J.B. and Orphan, V.J. (2012) Trace metal requirements for microbial enzymes involved in the production and consumption of methane and nitrous oxide. *Frontiers in Microbiology* **3**(61): 1-20.

Glass, J.B., Yu, H., Steele, J.A., Dawson, K.S., Sun, S., Chourey, K., Pan, C., Hettich, R.L., Orphan, V.J. (2014) Geochemical, metagenomic and metaproteomic insights into trace metal utilization by methane-oxidizing microbial consortia in sulphidic marine sediments. *Environmental Microbiology* **16**(6): 1592-1611.

Glass, J.B. and Dupont, C.L. (2017) Oceanic nickel biogeochemistry and the evolution of nickel use. In: *The Biological Chemistry of Nickel*, p. 12-26

Gorman-Lewis, D., Martens-Habbena, W. and D.A. Stahl (2014) Thermodynamic characterization of proton-ionizable functional groups on the cell surfaces of ammonia-oxidizing bacteria and archaea. *Geobiology* **12**: 157-171.

Gustavsson, J., Yekta, S.S., Sundberg, C., Karlsson, A., Ejlertsson, J., Skyllberg, U., Svensson, B.H. (2013) Bioavailability of cobalt and nickel during anaerobic digestion of sulfur-rich stillage for biogas formation. *Applied Energy* **112**: 473-477.

Heuer, V.B., Pohlman, J.W., Torres, M.E., Elvert, M., Hinrichs, K.-U. (2009) The stable carbon isotope biogeochemistry of acetate and other dissolved carbon species in deep subseafloor sediments at the northern Cascadia Margin. *Geochimica et Cosmochimica Acta* **73**(11): 3323-3336.

Hinrichs, K-U., Hayes, J.M., Sylva, S.P., Brewer, P.G., DeLong, E.F. (1999) Methane-consuming archaebacteria in marine sediments. *Nature* **398**: 802-805.

Jansen, S., Steffen, F., Threels, W.F., van Leeuwen, H.P. (2005) Speciation of Co(II) and Ni(II) in Anaerobic Bioreactors Measured by Competitive Ligand Exchange–Adsorptive Stripping Voltammetry. *Environmental Science & Technology* **39**(24): 9493-9499.

Jansen, S., Gonzalez-Gil, G., van Leeuwen, H.P. (2007) The impact of Co and Ni speciation on methanogenesis in sulfidic media – Biouptake versus metal dissolution. *Enzyme Microbiology Technology* **40**: 823-830.

Jaun, B. and Thauer, R.K. (2007) Methyl-Coenzyme M Reductase and its nickel corphin coenzyme F_{430} in methanogenic archaea. In: *Nickel and Its Surprising Impact in Nature, vol. 2*, p. 323-356.

Klinkhammer, G. (1980) Early diagenesis in sediments from the eastern equatorial Pacific, II. Pore water metal results. *Earth and Planetary Science Letters* **49**: 81-101.

Knittel, K. and Boetius, A. (2009) Anaerobic oxidation of methane: Progress with an unknown process. *Annual Review of Microbiology* **63**(1): 311-334.

Krüger, M., Meyerdierks, A., Glöckner, F.O., Amann, R., Widdel, F., Kube, M., Reinhardt, R., Kahnt, J., Böcher, R., Thauer, R.K., Shima, S. (2003) A conspicuous nickel protein in microbial mats that oxidize methane anaerobically. *Nature* **426**(6968): 878-881.

Little, S.H., Vance, D., Lyons, T.W., McManus, J. (2015) Controls on trace metal authigenic enrichment in reducing sediments: Insights from modern oxygen-deficient settings. *American Journal of Science* **315**: 77-119.

Mau et al. (2013) Vertical distribution of methane oxidation and methanotrophic response to elevated methane concentrations in stratified waters of the Arctic fjord Storfjorden (Svalbard, Norway). *Biogeosciences* **10**: 6267-6278.

Mayr, S., Latkoczy, C., Krüger, M., Günther, D., Shima, S., Thauer, R.K., Widdel, F., Jaun, B. (2008) Structure of an F430 variant from archaea associated with anaerobic oxidation of methane. *Journal of the American Chemical Society* **130**: 10758-10767.
oxidation of methane.

Orphan, V.J., House, C.H., Hinrichs, K-U., McKeegan, K.D., DeLong, E.F. (2002) Multiple archaeal groups mediate methane oxidation in anoxic cold seep sediments. *Proceedings of the National Academies of Science* **99**(11): 7663-7668.

Öztürk, M. (1995) Trends of trace metal (Mn, Fe, Co, Ni, Cu, Zn, Cd and Pb) distributions at the oxic-anoxic interface and in sulfidic water of the Drammensfjord. *Marine Chemistry* **47**: 329-342.

Pereira, I.A.C., Ramos, A.R., Grein, F., Marques, M.C., da Silva, S.M., Venceslau, S.S. (2011) A comparative genomic analysis of energy metabolism in sulfate reducing bacteria and archaea. *Frontiers in Microbiology* **2**: 69.

Reeburgh, W.S. (2007) Oceanic methane biogeochemistry. *Chemical Reviews* **107**: 486-513.

Riedinger, N., Formolo, M.J., Lyons, T.W., Henkel, S., Beck, A., Kasten, S. (2014) An inorganic geochemical argument for coupled anaerobic oxidation of methane and iron reduction in marine sediments. *Geobiology* **12**: 172-181.

Roe, K.L., Barbeau, K., Mann, E.L., and Haygood, M.G. (2012) Acquisition of iron by Trichodesmium and associated bacteria in culture. *Environmental microbiology* **14**(7): 1681-1695.

Ruff, S.E., Biddle, J.F., Teske, A.P., Knittel, K., Boetius, A., Ramette, A. (2015) Global dispersion and local diversification of the methane seep microbiome. *Proceedings of the Natural Academies of Sciences* **112**(13): 4015-4020.

Saito, M.A. and Moffett, J.W. (2001) Complexation of cobalt by natural organic ligands in the Sargasso Sea as determined by a new high-sensitivity electrochemical cobalt speciation method suitablef or open ocean work. *Marine Chemistry* **75**: 49-68.

Scheller, S., Goenrich, M., Boecher, R., Thauer, R.K., Jaun, B. (2010) The key nickel enzyme of methanogenesis catalyses the anaerobic oxidation of methane. *Nature* **465**(3): 606-608.

Scherer, P. and Sahm, H. (1981) Effect of trace elements and vitamins on the growth of *Methanosarcina barkeri*. *Acta Biotechnologica* **1**: 57-65.

Schöndheit, P., Moll, J., Thauer, R.K. (1979) Nickel, cobalt, and molybdenum requirement for growth of *Methanobacterium thermautotrophicum*. *Archives of Microbiology* **123**: 105-107.

Shaw, T.J., Gieskes, J.M., and Jahnke, R.A. (1990) Early diagenesis in differing depositional environments: The response of transition metals in pore water. *Geochimica et Cosmochimica Acta* **54**: 1233-1246.

Sigurdsson, H., Leckie, R.M., and Acton, G.D., et al. (1997) Caribbean Volcanism, Createaceous/Tertiary Impact, and Ocean-Climate History: Synthesis of Leg 165. *Proceedings of the Ocean Drilling Program, Initial Reports* **165**: 377-400.

Thauer, R.K., Kaster, A.-K., Goenrich, M., Schick, M., Hiromoto, T., Shima, S. (2010) Hydrogenases from methanogenic archaea, nickel, a novel cofactor, and H_2 storage. *Annual Reviews in Biochemistry* **79**: 507-536.

Valentine, D.L., Blanton, D.C., Reeburgh, W.S., Kastner, M. (2001) Water column methane oxidation adjacent to an area of active hydrate dissociation, Eel River Basin. *Geochimica et Cosmochimica Acta* **65**: 2633-2640.

Van den Berg, C.M.G. and Nimmo, M. (1987) Determination of interactions of nickel with dissolved organic material in seawater using cathodic stripping voltammetry. *Science of the Total Environment* **60**: 185-195.

Vraspir, J.M. and Butlet, A. (2009) Chemistry of Marine Ligands and Siderophores. *Annual Review of Marine Science* **1**: 43-63.

Wallman, K., Riedel, M., Hong, W.L., Patton, H., Hubbard, A., Pape, T., Hsu, C.W., Schmidt, C.,
Johnson, J.E., Torres, M.E., Andreassen, K., Berndt, C., Bohrmann, G. (2018) Gas hydrate dissociation off Svalbard induced by isostatic rebound rather than global warming. *Nature Communications* **9**(83):1-9

Whitman, W.B., Ankwanda, E., and Wolfe, R.S. (1982) Nutrition and Carbon Metabolism of *Methanococcus voltae* **149**(3): 852-863.

Zerkle, A.L., House, C.H., and Brantley, S.L. (2005) Biogeochemical signatures through time as inferred from whole microbial genomes. *American Journal of Science* **305**(6-8): 467-502.

4.6 Figures & Tables

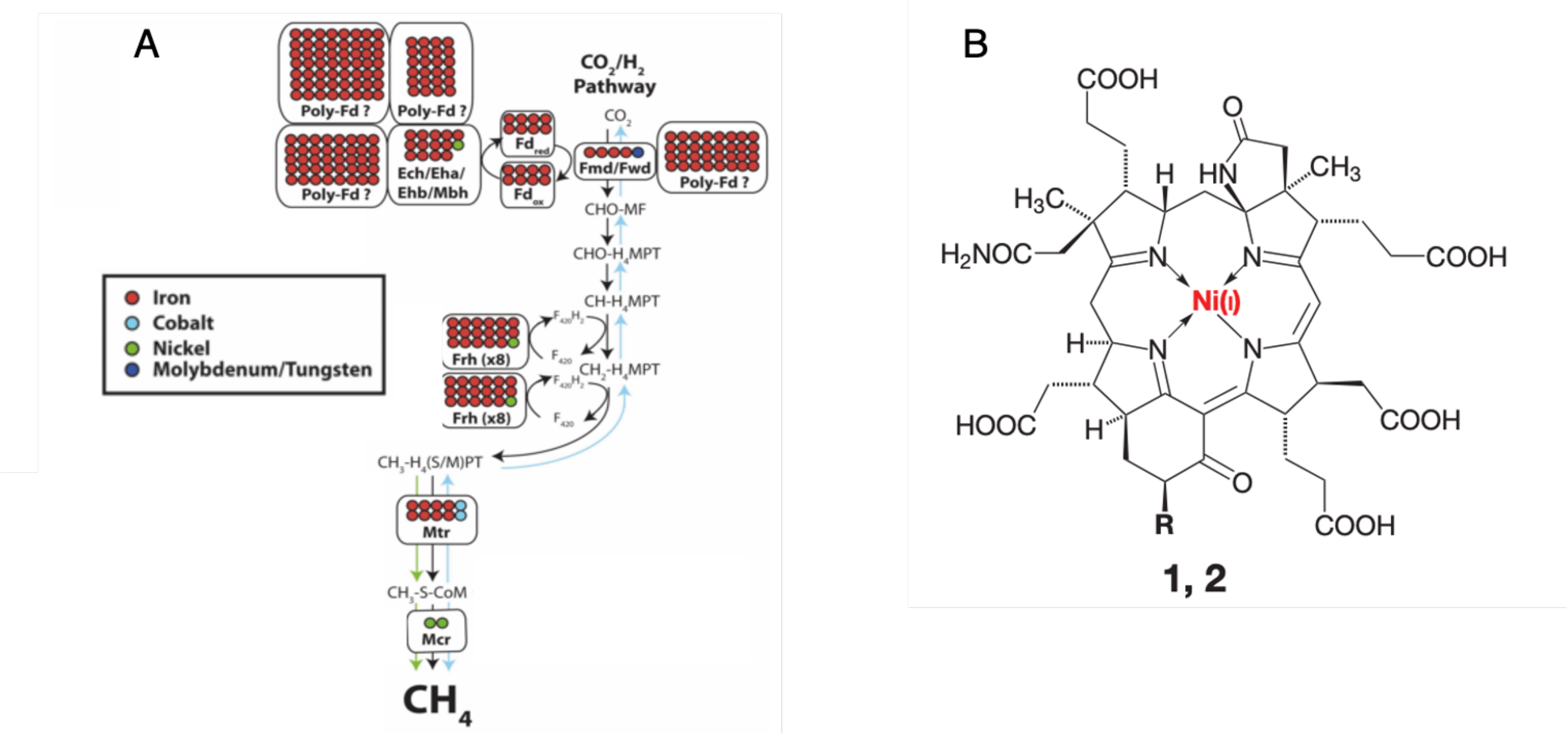

Figure 4.1. (A) Schematic of metalloenzymes involved in the CO_2/H_2 production of CH_4. Each circle represents one metal atom. Black arrows between boxes correspond to the CO_2/H_2 metabolic pathway. The final step of methanogenesis and the first step of methanotrophy are catalyzed by methyl-coenzyme M reductase (MCR). **(B)** Cofactor F_{430} is the central cofactor in MCR. *Figure (A) modified from Glass and Orphan (2012). Figure (B) from Scheller et al., 2010.*

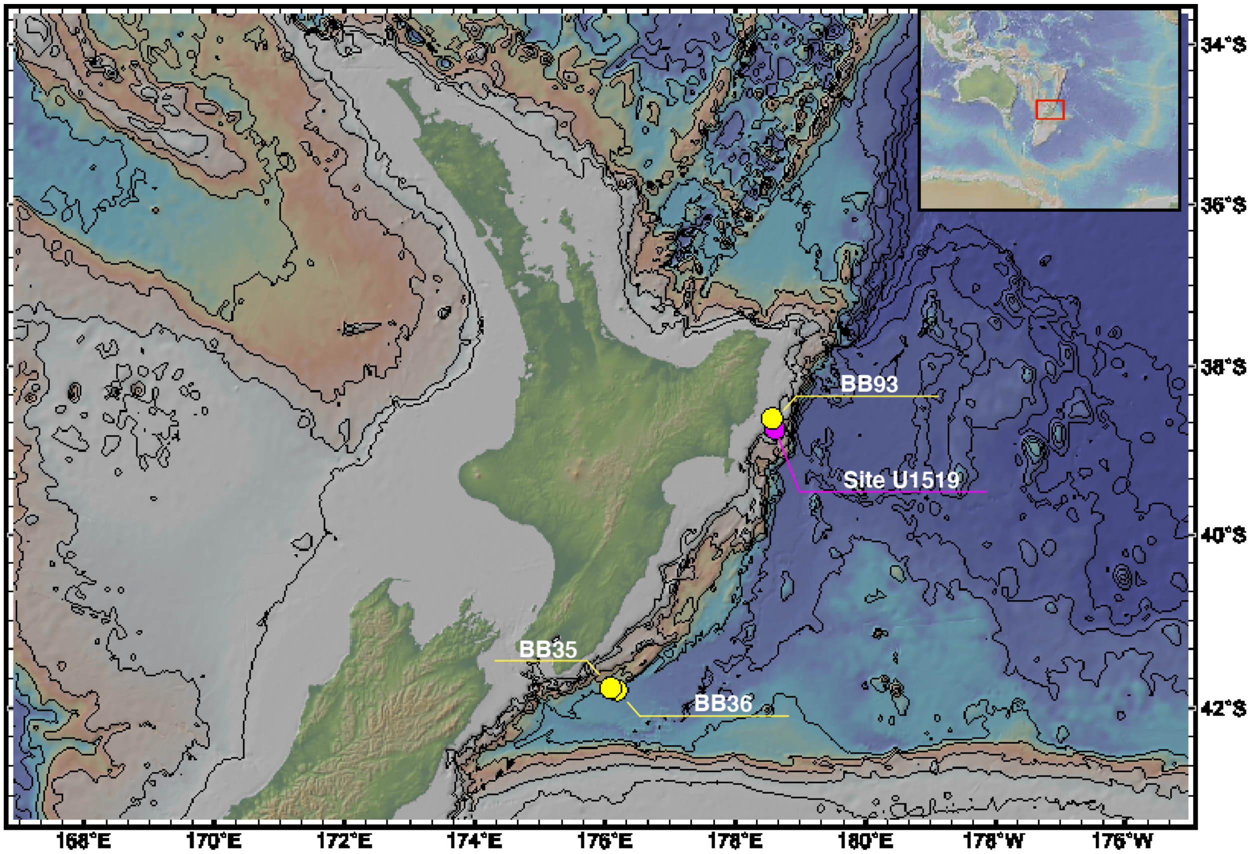

Figure 4.2. Regional map of the Hikurangi margin offshore the North Island of New Zealand. Yellow circles identify locations cored during the 2019 SAFFRONZ cruise. BB35 and BB36 are located on the southern portion of the margin. BB93 is located on the northern portion of the margin near Site U1519, identified in pink.

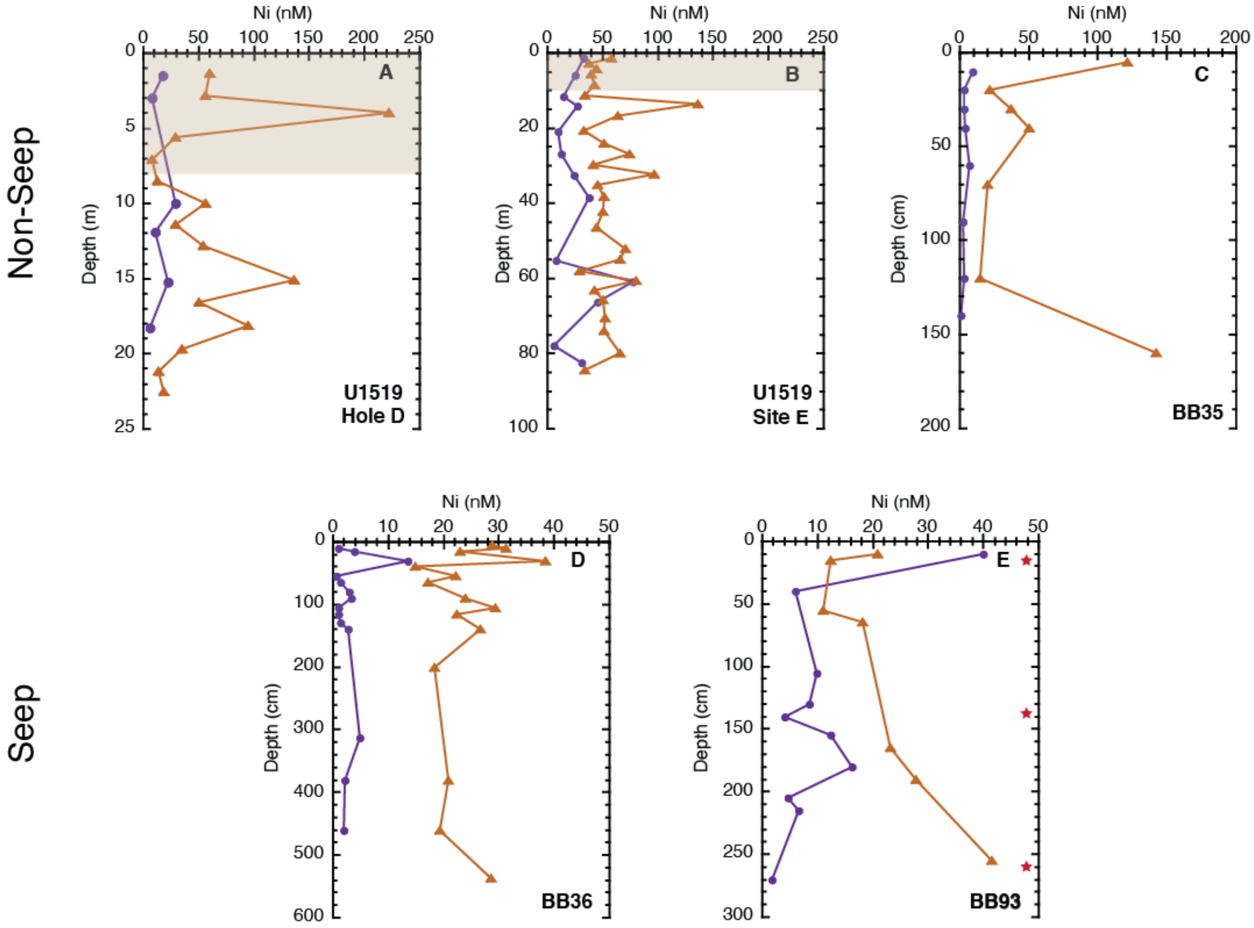

Figure 4.3. Downcore profiles of total nickel concentrations (orange triangles) and labile concentrations (purple circles) for each core in this study. Holes D and E (A and B, respectively) were drilled at IODP Site U1519 along the northern Hikurangi margin in a slope basin where solute transport is dominated by diffusion. The shaded regions in (A) and (B) denote the depth range where sulfate was detected in pore water. BB35 (C) was also cored at a site dominated by diffusive solute transport on the southern Hikurangi margin. BB36 (D) and BB93 (E) were collected at actively venting seep sites in the south and north, respectively. The red stars along the y-axis of the BB93 profile indicate the sampling depths that were analyzed for characterization of organic nickel complexes via LC-ICP/ESI-MS. Global average bottom water Ni_{tot} is approximately 7–12 nM.

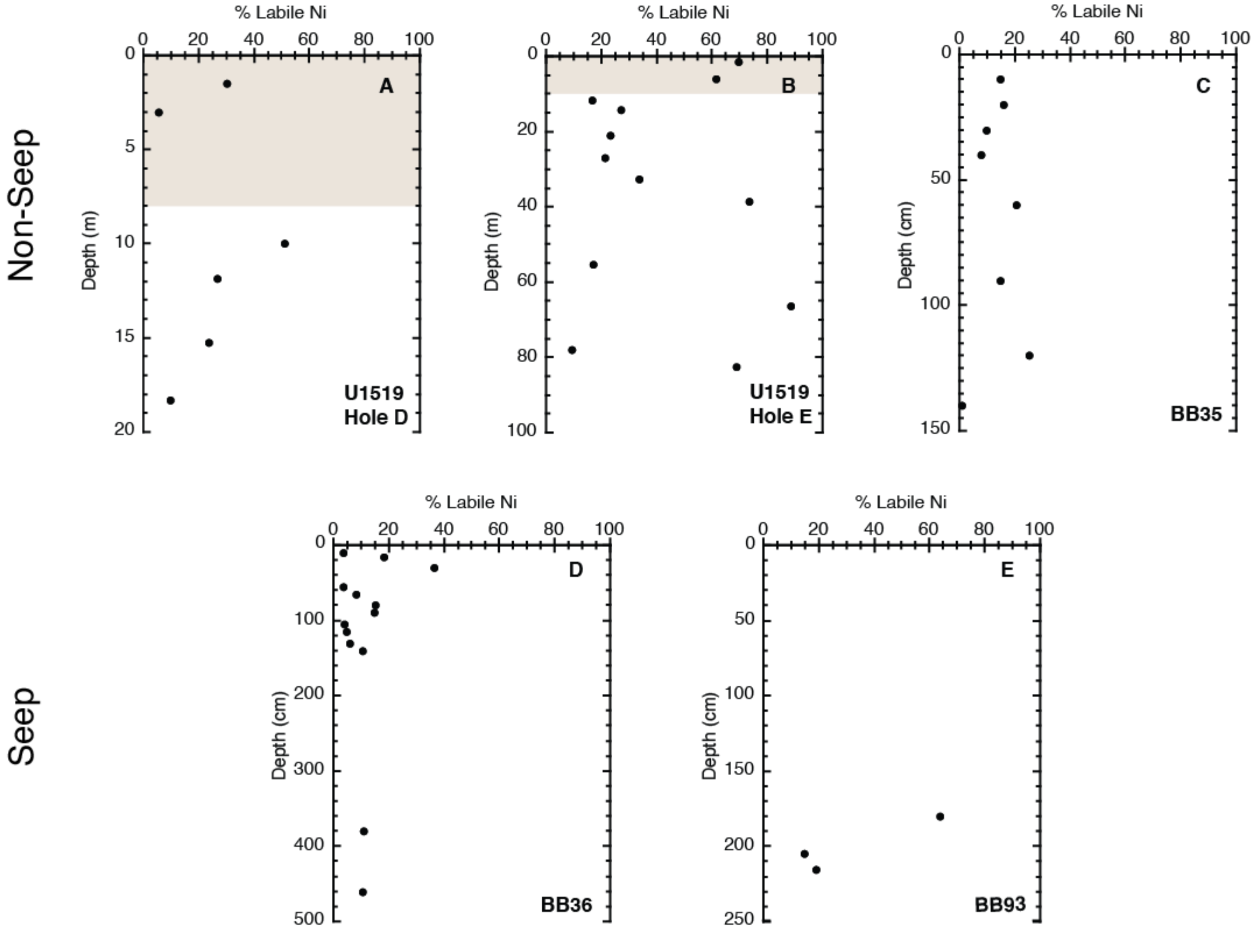

Figure 4.4. Downcore profiles of the labile fraction of total nickel in each core. The shaded regions in (A) and (B) denote the depth range where sulfate was detected in pore water.

Table 4.1. Measured concentrations of labile nickel (CSV), strongly complexed nickel (LC-ICP-MS), and total nickel (ICP-MS) for three samples from BB93. The labile Ni fraction was not measured for BB93–15cm.

Sample	$[\mathrm{Ni}]_{\mathrm{labile}}$ (nM)	$[\mathrm{Ni}]_{\mathrm{SOC}}$† (nM)	$[\mathrm{Ni}]_{\mathrm{total}}$ (nM)	% $\mathrm{Ni}_{\mathrm{labile}}$	% $\mathrm{Ni}_{\mathrm{complexed}}$
BB93–15cm	-	9.2	12.43	-	74%
BB93–140cm	4.09	10.9	19.4*	27%	73%
BB93–270cm	1.80	10.8	15.4*	14%	86%

* $[\mathrm{Ni}]_{\mathrm{total}}$ calculated from adding $[\mathrm{Ni}]_{\mathrm{labile}}$ and $[\mathrm{Ni}]_{\mathrm{complexed}}$. This is not a measured value.

† SOC – strong organic complex

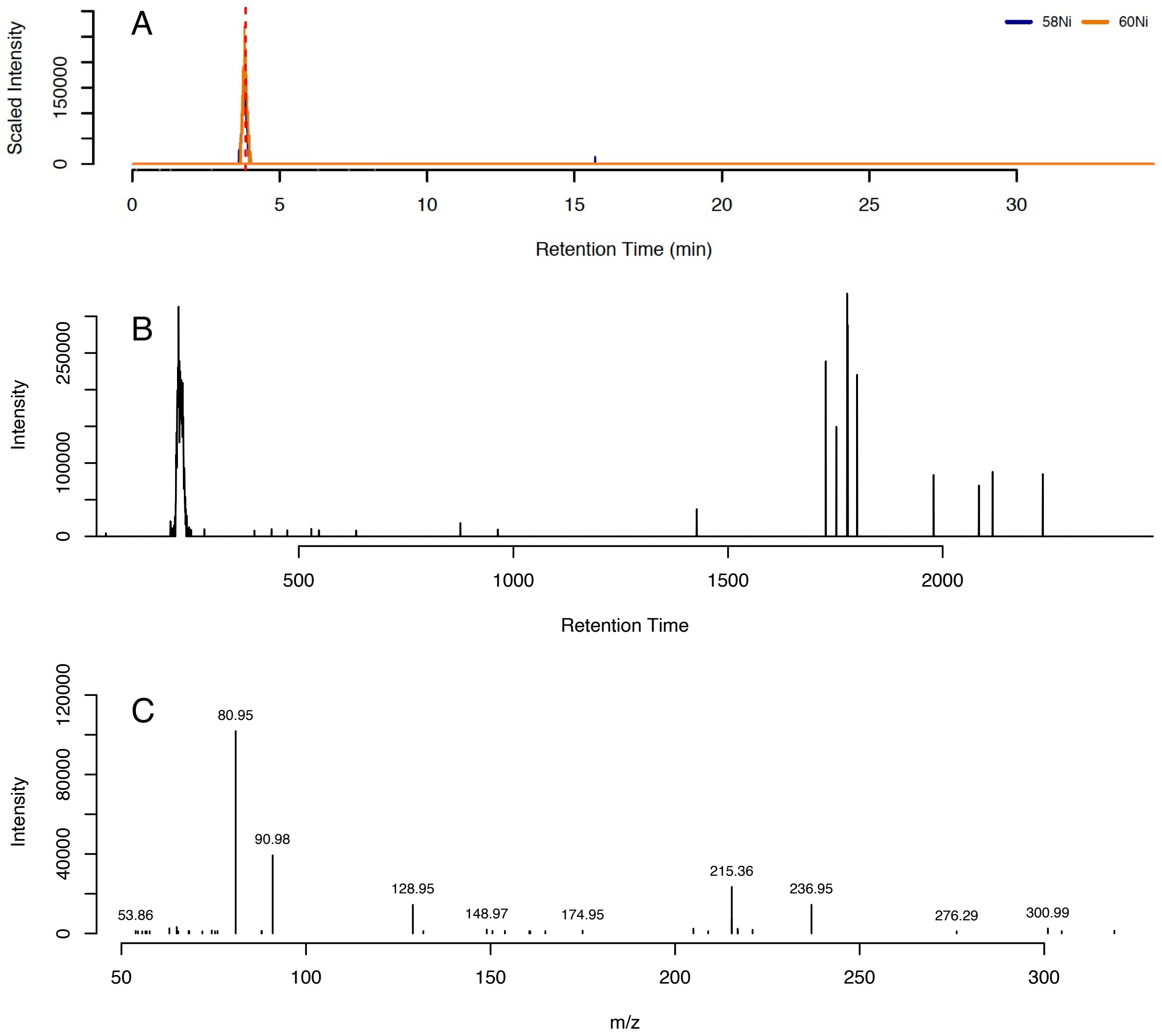

Figure 4.5. Panel (A) shows the extracted ion chromatogram at *m/z* = 330.914 which eluted at 3.71 minutes. Panel (B) shows the MS^1 of this compound and (C) shows the fragmentation *m/z* ratios. This unknown nickel-containing organic compound was found at all sampled depths within core BB93.

Table 4.2. MS^1 masses, dominant fragments, and putative chemical formulas for Ni-containing compounds recognized in the three samples analyzed from BB93. This table shows only those compounds for which fragmentation data was collected. Putative chemical formulas were calculated using www.chemcalc.org to find those formulas that matched the *m/z* within 0.02 PPM, contained Ni, and had a monoisotopic mass equal to losing either one H^+ or Na^+. Chemical formulas were unable to be calculated for two *m/z* ratios using C, H, N, O, S, Ni, and ^{13}C.

Sample	Retention Time (min)	*m/z*	Dominant Fragments (*m/z*)	Putative Chemical Formula
15 cm	3.38	342.788	80.95 164.92 90.98	$C_4HNi_3O_3S^{13}C_3$ C_3NNiO_9S
15 cm	3.18	284.872	164.92 216.7	C_3NNiO_9S
15 cm **140 cm**	3.35	400.747	992.93 3763.75 5089.47	$C_3H_3NNi_2S_6{}^{13}C_3$ $C_2H_{111}N_4NiO_6S$
15 cm	3.63	386.853	90.98 214.98 204.96	$C_4H_{20}Ni_3OS_4$ $C_5HNO_7S_5{}^{13}C_3$
15 cm **270 cm**	3.80	360.925	90.98 128.95	$H_{125}N_8NiO_4$ $C_8H_7NiO_3S_2{}^{13}C_5$ $H_{125}N_8NiO_4$
15 cm **140cm** **270 cm**	3.71	330.914	80.95 90.98	$C_9H_{12}NNi_2OS_2$
140 cm	4.03	530.766	64.98 200.95 218.8	$C_7HN_5NiO_7S_6{}^{13}C$ $H_9N_6Ni_4O_7S^{13}C_3$
140 cm	24.71	331.000	98.98	–
270 cm	3.79	522.828	90.98 215.14 204.96	$C_2H_{24}N_2Ni_4O_8S_2$ $C_3H_{128}N_6NiOS_5{}^{13}C_3$ $C_9H_{124}N_2Ni_2O_3S^{13}C_5$
270 cm	3.82	560.805	214.91 330.93 128.95	$C_{10}H_6N_6Ni_3O_9S$ $C_9N_{13}Ni_3O_4S$ $C_{11}H_{17}N_2Ni_5O_2{}^{13}C_3$ $C_5H_{21}N_6Ni_4S_4{}^{13}C$ $C_{18}H_9NNi_2O_2S_5{}^{13}C$ $C_7H_8NiO_{11}S_5{}^{13}C_4$ $H_{137}N_4Ni_3O_5S_2{}^{13}C_2$
270 cm	3.89	360.925	90.98 216.32 128.95	$H_{125}N_8NiO_4$ $CH_{131}NNiO_9$ $C_8H_7NiO_3S_2{}^{13}C_5$ $C_2H_{11}N_4OS_6{}^{13}C_3$
270 cm	3.71	400.886	128.95 214.67	$H_{21}N_2Ni_4O_3S^{13}C_3$ $H_6N_5NiO_6S_3{}^{13}C_4$

				$C_6H_{123}N_4NiO_2S^{13}C_2$
270 cm	3.74	272.998	90.98	–
270 cm	3.87	288.953	174.95 217.52	$CH_4N_7NiS_2{}^{13}C_4$ $C_2H_{10}NiO_5S_2{}^{13}C_4$

Table 4.3. Three molecular fragments were found to occur in multiple Ni-containing compounds within samples from BB93. Similar fragments within 10 ppm mass difference are presented along with representative functional groups of each fragment.

Sample	# of occurrences	Fragment *m/z*	ΔPPM	Similar Fragment	Functional Group(s)
15 cm 140 cm 270 cm	7	90.98	10	Carbon suboxide (C_3O_2)	Carboxyl
15 cm 270 cm	4	128.95	10	Methylthiothichloroborane (CH_3BCl_2S)	Methyl sulfide
15 cm 270 cm	2	204.96	0	Dimercaptosuccinic acid ($C_4H_6O_4S_2$)	Carboxylic acid (2) Thiol (2)

Chapter 5.

Summary and Conclusions

5.1 Key Conclusions from Chapter 2

Chapter 2 evaluated the impact of modern bottom water warming on the methane hydrate reservoir along the upper continental slope of the Washington margin using pore water geochemistry. Data presented in this chapter lack diagnostic evidence for widespread methane hydrate dissociation hypothesized as a result of modern bottom water warming at the upper limit of methane hydrate stability but revealed deep-sourced mineral dehydration reactions and meteoric water are important fluid sources. Though there is no unambiguous geochemical evidence for contemporary methane hydrate dissociation, continued bottom water warming will eventually lead to dissociation of hydrates along the upper continental slope. The impact of future methane release into the sediment column and hydrosphere remains unknown, but factors enhancing and limiting the rates of anaerobic oxidation of methane (AOM) in the sediment column—the most important sink for methane—are investigated in Chapters 3 and 4.

5.2 Key Conclusions from Chapter 3

In Chapter 3, I presented time-series measurements of fluid flow and composition within a *Beggiatoa* bacterial mat at a Southern Hydrate Ridge cold seep. This time-series data was collected as part of the Ocean Observatories Initiative Regional Cabled Array and is the longest continuous record of fluid flow rates and composition at a cold seep to date. Continuous fluid flow rate measurements reveal persistent downward flow of seawater into the bacterial mat community over time, contrary to the expected flow pattern. Despite the chronic downward flow of seawater into the sediment column, records of pore water geochemistry revealed the rapid depletion of sulfate at shallow depths, indicating that rates of microbial reactions are enhanced in this system compared to systems characterized by the upward advection of fluid. Recharge of sulfate-rich seawater coupled with high pore water concentrations of dissolved methane increases the rate of sulfate consumption and bisulfide production via AOM, thus generating a steep diffusional gradient of reduced sulfur to the overlying *Beggiatoa* community. Model results indicate that the rate of AOM must be far greater in this system than in a system with predominantly upward fluid flow, and thus the consumption of oxygen, nitrate, and calcium must also be greater in this setting, as should the production of alkalinity. The exact mechanism of gas transport that induces shallow seawater circulation in this environment remains unclear and requires numerical modeling of 2-phase (water and gas) flow.

Shallow seawater circulation may be a prevalent phenomenon at cold seeps globally (e.g. Henry et al., 1996; Solomon et al., 2008; Aylward et al., 2020). The potential pervasiveness of shallow seawater circulation and enhanced rates of microbial reactions in these systems may have a profound impact on regional and global biogeochemical cycling. Additional studies that measure volumetric discharge and residence time of circulating fluid across a seep site and further constrain the rates of microbial reactions in these systems are necessary before regional and global modeling of this phenomenon can elucidate the impact on biogeochemical cycles.

5.3 Key Conclusions from Chapter 4

Chapter 4 probed the possibility that variation in the efficiency of AOM to remove methane from pore water before escape to the water column could be a result of bio-essential nickel limitation to the anaerobic methanotrophic community. The investigation of trace metal complexation and, thus, bioavailability is a new endeavor in cold seep systems. The study results presented in this chapter are the first of its kind. Data collected in this investigation show that seep systems have a smaller fraction of bioavailable nickel than non-cold seep systems, possibly due to greater nickel utilization in active seeps than non-seep environments. The relative depletion of bioavailable nickel in cold seeps where ANME thrive should lead to a diminished capacity of AOM to reduce methane before discharging into the water column. In addition, data presented in this chapter uncover a strong diffusional gradient of nickel to the ocean in each environmental setting with most of the nickel bound in strong complexes. The effect of subsurface complexation of nickel, and potentially other trace metals, on nutrient exchange with the hydrosphere is unknown and requires further study.

I additionally sought to characterize the organic nickel-ligand complexes in an attempt to shed light on whether ANME may excrete extracellular ligands to compete for strongly-bound nickel, similar to how heterotrophic bacteria and fungi produce siderophores to compete for iron. We found there is an abundant diversity of microbially produced ligands that complex nickel in cold seep pore water, one of which may be key to nickel acquisition. One nickel-ligand fragment identified is an exact match to a well-known metal chelator (dimercaptosuccinic acid) used in modern medicine to complex lead, arsenic, and mercury in cases of chronic toxicity. Measurement of this particular fragment in association with some of the organic nickel-containing compounds provides additional support for the hypothesis that microbes in cold seep sediments may be intentionally secreting trace metal-specific ligands to either enhance bio-uptake or to prevent toxicity. Further testing of this hypothesis requires coupled geochemical and microbiological studies of ANME ligand production under nickel limitation. The organic nickel ligands discovered in this environment may be actively produced by the *in situ* microbial community, desorbed from mineral phases, or released from cells during viral lysis. Little is known about the virosphere in cold seep sediments. Virus-archaea interactions could be a key link to understanding ANME community health and implications for AOM efficiency.

5.4 Final Thoughts

The research presented in this dissertation adds to our understanding of the biogeochemical coupling of the hydrosphere and the subseafloor biosphere in cold seep and methane hydrate systems. These biogeochemical systems respond acutely to changes in ocean temperature, subseafloor hydrogeology, and nutrient cycling.

As demonstrated in Chapters 3 and 4, the investigation of nutrient cycling between cold seep sediments and the ocean is an area of research ripe with potential for new discovery. Cold seeps are dynamic environments with high biogeochemical turnover and the exchange of solutes between the seafloor sediments and the overlying ocean cannot be decoupled. The exchange of fluid and solutes among the hydrosphere, geosphere, and subseafloor biosphere may have a profound influence on regional and global biogeochemical cycling of nutrients and deserves further investigation.

5.5 References

Aylward, I.E., Solomon, E.A., Torres, M.E., Whorley, T.L., Harris, R.N., Hillman, J., Philip, B.T. (2020) Geochemical Constraints on the Hikurangi Margin Hydrogeologic System – Results from the SAFFRONZ Expedition. *American Geophysical Union Fall Meeting*.

Henry, P., Le Pichon, X., Lallemant, S., Lance, S., Martin, J.B., Foucher, J-P., Fiala-Médioni, A., Rostek, F., Guilhaumou, N., Pranal, V., Castrec, M. (1996) Fluid flow in and around a mud volcano field seaward of the Barbados accretionary wedge: Results from Manon cruise. *Journal of Geophysical Research* **101**(96): 297-323.

Solomon, E.A., Kastner, M., Jannash, H., Robertson, G., Weinstein, Y. (2008) Dynamic fluid flow and chemical fluxes associated with a seafloor gas hydrate deposit on the northern Gulf of Mexico slope. *Earth and Planetary Science Letters* **270**: 95-105.

Appendix A.

Supplemental Material for Chapter 2.

Table A-1**.** Pore water hydrocarbon concentrations from five Sites. Dashes indicate no measurable concentration in the sample. Concentrations are given in parts per million by volume (ppmv).

Site	Sample ID	$C_1/(C_2+C_3+n\text{-}C_4)$	C_1 (ppmv)	C_2 (ppmv)	C_3 (ppmv)	n-C_4 (ppmv)
6	H200	10852	9767	-	-	0.90
2	H17	8036	8036	-	-	<0.5
4	H118	1721	6797	3.95	<0.5	<0.5
4	H120	2809	6911	2.46	<0.5	<0.5
4	H122	2715	7357	2.71	<0.5	<0.5
4	H138	1780	7782	4.37	<0.5	<0.5
4	H139	1493	4627	2.40	<0.5	0.70
4	H141	1557	2880	1.85	<0.5	<0.5
5	H158	2819	11447	3.36	0.7	<0.5
5	H160	2720	12811	4.71	<0.5	<0.5
5	H162	10260	22264	2.17	<0.5	<0.5
8	H273	4538	4538	<0.5	<0.5	-
8	H275	9157	9157	<0.5	<0.5	-
8	H286	7688	6535	0.85	<0.5	-
8	H284	15245	6708	0.44	<0.5	-

Table A-2. Fractionation factors (i.e. enrichment factors from initial isotope values of individual fluid sources) for fluid sources invoked in Site 4 mixing scenarios.

Source	**Cl (mM)**	**δ^{18}O (‰, VSMOW)**	**δD (‰, VSMOW)**
Clay Formation	N/A	-28.5[a]	+70[a]
Deep Source (Site 2)	0	+2.51[b]	-11.1[b]
Meteoric Water (Elwha springs)	0	-12.7[c]	-96.56[c]
Meteoric Water (Forks, WA)	0	-8.5[d]	-62‰
Fresh Fluid end-member (Site 4)	0	-2.42‰	-13.2‰
GH Formation	–	-3	-21[e]
GH Dissociation	0	+3	+21
Seawater	559	0	0

[a] Values taken from Savin & Epstein (1970).

[b] Values taken from deep fluid end-member at Site 2.

[c] Meteoric Water isotope values calculated from Sidle & Cvetic (2011) for groundwater springs in the Elwha watershed, Olympic Peninsula, WA, USA.

[d] Theoretical values calculated from the University of Utah Online Isotopes in Precipitation Calculator (OIPC) at 47.9022ºN 124.624ºW accounting for 3 m elevation above sea level (Bowen, 2020; IAEA/WMO, 2015).

[e] δD value taken from Maekawa & Imai (2000)

Mixing calculations for Site 4 fluid sources

We explored four potential scenarios of fluid mixing to investigate the source of fluids sampled at Site 4 and the negative trends in $\delta^{18}O$ and δD with depth. Scenario 1 invokes a binary mixing situation between seawater and meteoric water. Meteoric water (MW) isotopic values were calculated from a local meteoric water line (LMWL) calculated specifically from groundwater springs in the Elwha watershed, Olympic Peninsula on the coast of Washington (Sidle and Cvetic, 2011). Two end-member mixing was calculated using measured $\delta^{18}O$ values in the following series of equations:

$$f_A + f_B = 1 \qquad \text{Eqn. A-1}$$

$$\delta^{18}O_{meas} = f_A\delta^{18}O_A + f_B\delta^{18}O_B \qquad \text{Eqn. A-2}$$

where f is the fraction of each end-member fluid contributing to the measured pore water, A is the seawater end-member fluid, B is the meteoric water end-member, and $\delta^{18}O_{meas}$ is the measured $\delta^{18}O$ of the pore water at a single depth. $\delta^{18}O$ is assumed to be conservative. Equation S-2 can be rearranged to form the new equation

$$f_B = \frac{\delta^{18}O_{meas} - \delta^{18}O_A}{\delta^{18}O_B - \delta^{18}O_A} \qquad \text{Eqn.A-3}$$

The product of this equation is then used to compute f_A in Equation A-1 above.

Calculating individual proportions of fluid input in a three end-member mixing scenario requires three equations and two conservative tracers. $\delta^{18}O$ and Cl were assumed to be conservative and end-member fluids were assigned the compositions outlined in Table A-2. The three governing equations are as follows:

$$1 = f_1 + f_2 + f_3 \qquad \text{Eqn.A-4}$$

$$Cl_{meas} = Cl_1f_1 + Cl_2f_2 + Cl_3f_3 \qquad \text{Eqn. A-5}$$

$$\delta^{18}O_{meas} = \delta^{18}O_1f_1 + \delta^{18}O_2f_2 + \delta^{18}O_3f_3 \qquad \text{Eqn. A-6}$$

where f is the fraction of each of the three end-member fluids.

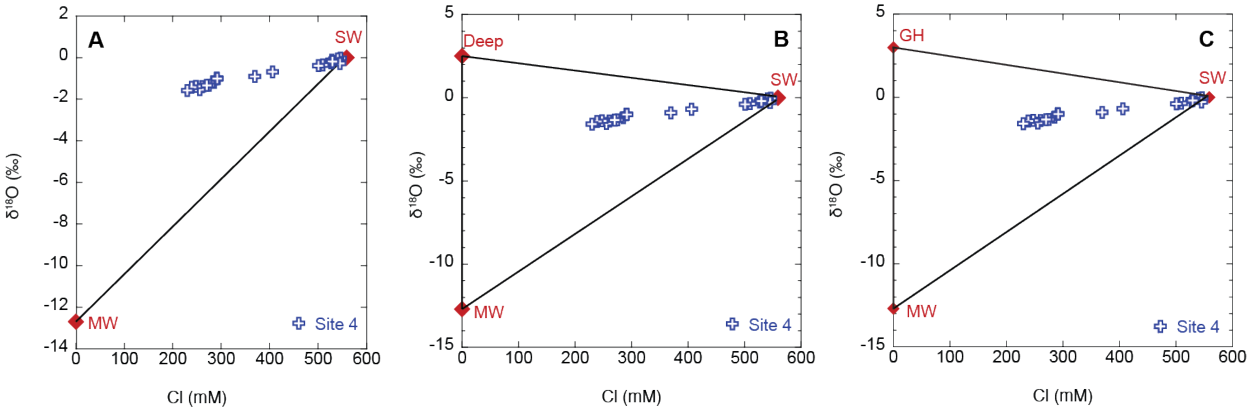

Figure A-1. Fluid end-member mixing scenarios for Site 4 pore water. Meteoric water $\delta^{18}O$ is taken from average groundwater spring values measured within the Elwha watershed (Sidle and Cvetic, 2011). (A) is a linear mixing line between seawater (SW) and meteoric water (MW); (B) is the region of Cl concentrations and $\delta^{18}O$ values for mixing of seawater, meteoric water, and deep water with an isotopic signature identical to that of Site 2 end-member fluid, and (C) is the region of values for mixing seawater, meteoric water, and gas hydrate (GH).

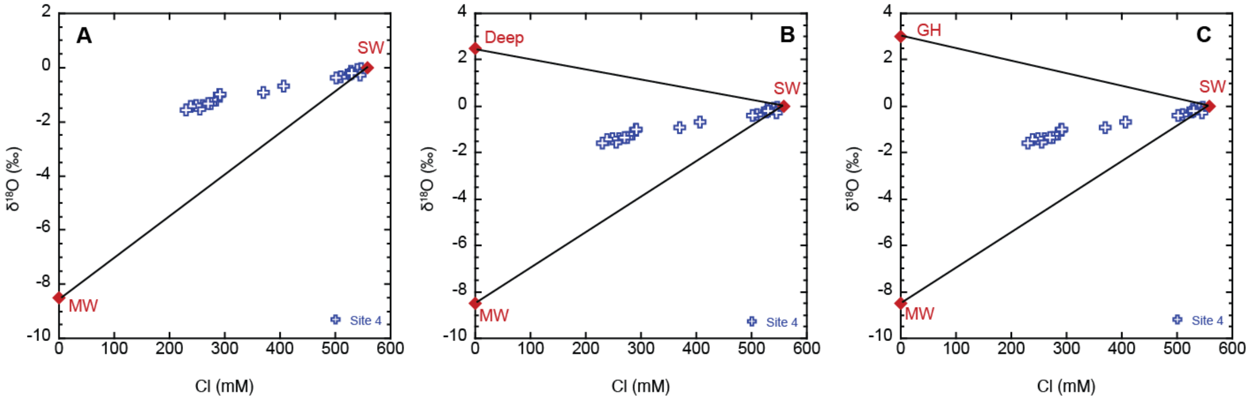

Figure A-2. Fluid end-member mixing scenarios for Site 4 pore water. Meteoric water $\delta^{18}O$ is a theoretical calculation for Forks, WA (47.9022º, -124.624º, 3 m above sea level), and is presented as a proxy for coastal meteoric water $\delta^{18}O$ during the last glacial maximum. (A) is a linear mixing line between seawater (SW) and meteoric water (MW); (B) is the region of Cl concentrations and $\delta^{18}O$ values for mixing of seawater, meteoric water, and deep water with an isotopic signature identical to that of Site 2 end-member fluid, and (C) is the region of values for mixing seawater, meteoric water, and gas hydrate (GH).

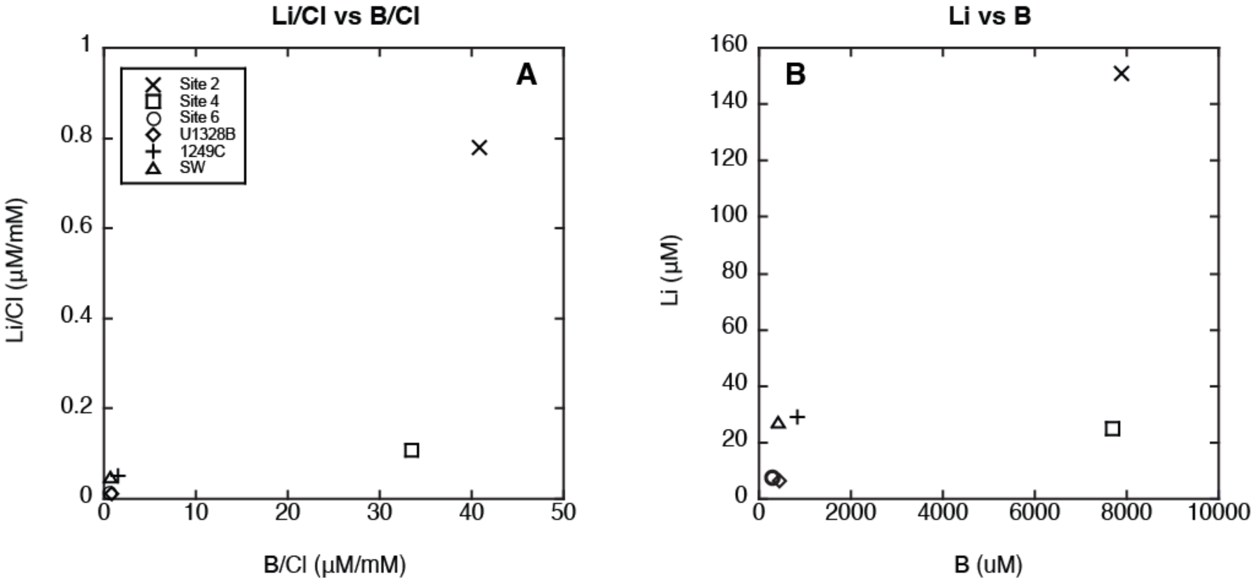

Figure A-3. Cross-plot of end-member Li and B concentrations. The values from each core were extrapolated to zero Cl concentration to estimate the Li and B concentrations in the original fresh fluid end-member. Values are from this study (GC5 – Site 2; GC17 – Site 4; GC31 – Site6), IODP Expedition 311 Site U1328 (Bullseye vent) on the mid-slope of the Cascadia margin offshore Vancouver Island (Riedel et al., 2006), and ODP Leg 204 Site 1249 at the summit of Southern Hydrate Ridge (Tréhu et al., 2003).

Appendix B.

Supplemental Figures for Chapter 3

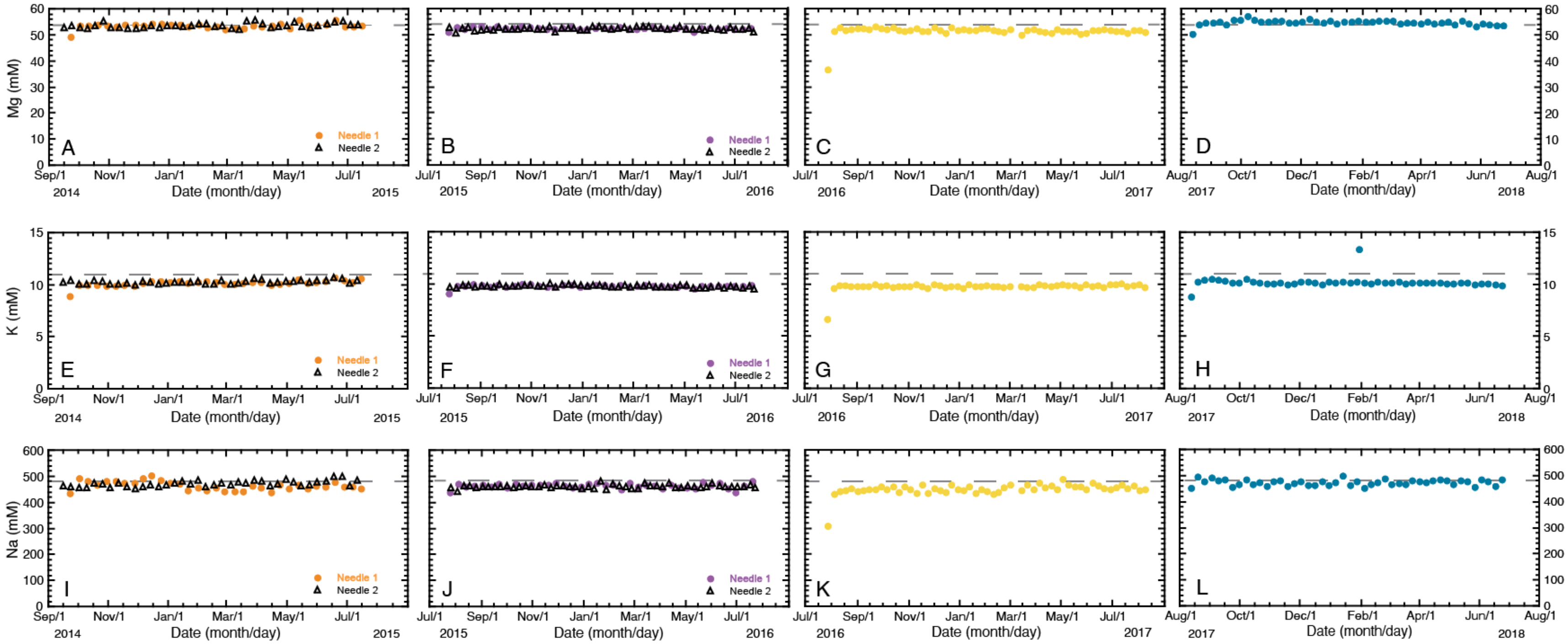

Figure B-1. Concentrations of Mg, K, and Na for Mosquitos deployed from 2014 through 2018. Gray dashed lines indicate seawater concentration of each solute.

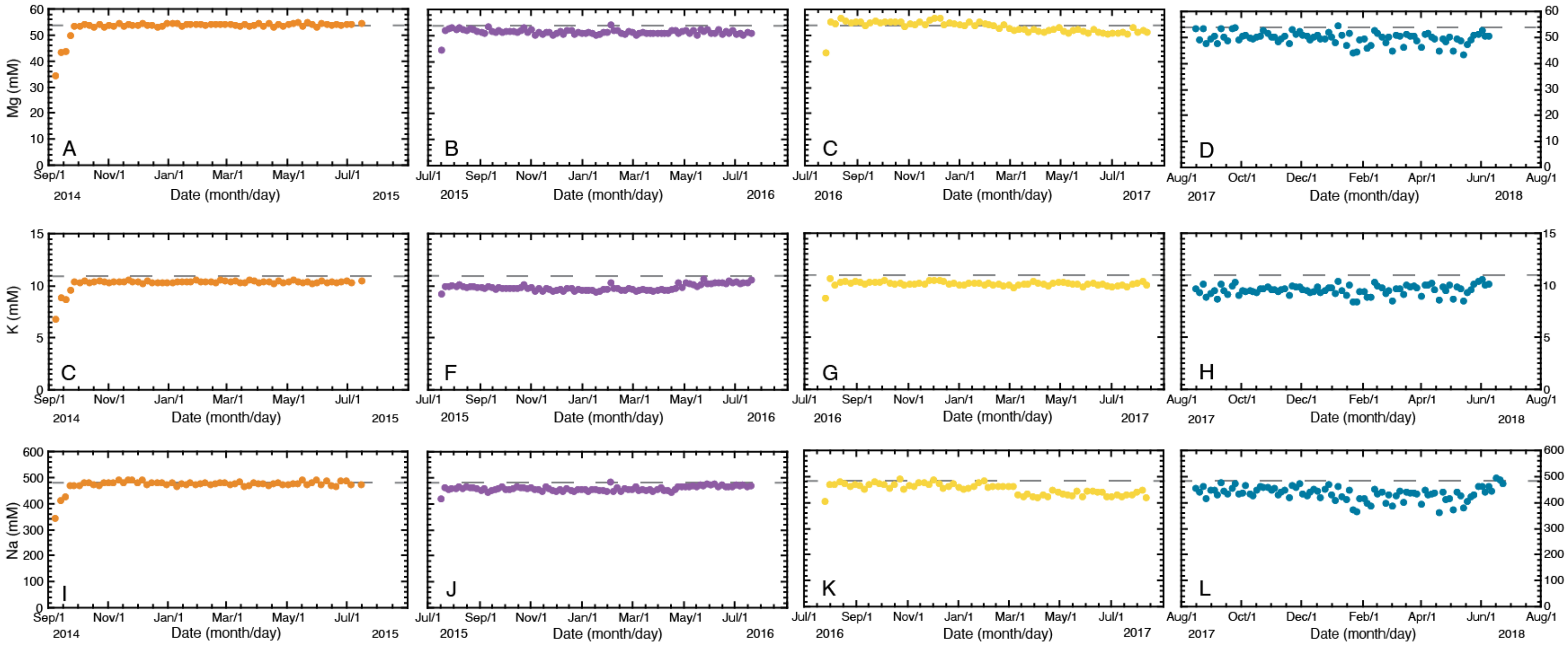

Figure B-2. Concentrations of Mg, K, and Na for CATs deployed from 2014 through 2018. Gray dashed lines indicate seawater concentration of each solute.

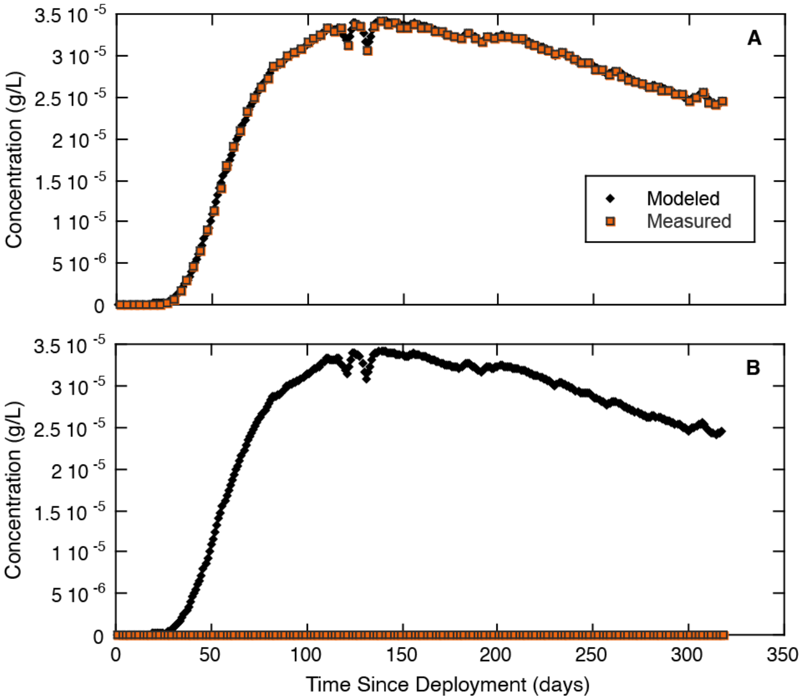

Figure B-3. Modeled fluid flow solution for M2017 Needle 3 (A) does not match the fluorescein concentration captured in the Needle 2 record (B). This discrepancy suggests that fluid flow is decoupled between 14.4 cm and 19.4 cm depth.

Appendix C.

Supplemental Material for Chapter 4

Table C-1. MS^1 masses and putative chemical formulas for Ni-containing compounds recognized in three BB93 samples. Putative chemical formulas were calculated using www.chemcalc.org to find those formulas that contained Ni, matched *m/z* data within 0.02 ppm, and had a monoisotopic mass equal to losing either one H^+ or Na^+.

Sample	Retention Time (min)	*m/z*	Putative Chemical Formula
15 cm	3.42	462.779	$C_9H_8N_2Ni_4O_4$
15 cm	3.45	436.780	$C_2H_3N_9Ni_4O^{13}C$
15 cm	3.45	378.863	$C_3H_{16}N_4Ni_4O$
15 cm	3.52	454.840	$C_{13}H_{12}Ni_3S_2{}^{13}C_2$ $H_{11}N_7Ni_4OS^{13}C_5$ $C_2H_{132}N_2NiO_3S_4{}^{13}C$
140 cm	3.81	904.349	$C_3N_{12}Ni_6S_{11}$ $C_{29}H_{95}NNi_3O_3S_7$ $C_3H_8N_2Ni_9O_{14}S_2$
140 cm	4.02	412.851	$C_{17}H_6Ni_2S_2$
140 cm	4.09	422.880	$C_2H_{18}N_3Ni_4O_5{}^{13}C_2$
140 cm	4.09	558.855	$CH_{126}N_9Ni_2O_5S^{13}C_5$ $C_{14}H_{127}N_2NiO_4S_2{}^{13}C_2$ $C_6H_{10}N_{11}Ni_3S_3{}^{13}C_4$ $C_{25}H_7Ni_3O^{13}C_3$ $C_{11}H_8N_9Ni_3O_6$
140 cm	3.86	554.601	$C_6H_{95}N_{12}NiO_2S_4$ $C_{12}H_{91}N_8Ni_2O_4{}^{13}C_2$ $CH_{90}N_7NiO_{13}{}^{13}C_5$
140 cm	3.86	620.684	$C_{16}H_{99}N_3NiO_{11}{}^{13}C_4$ $C_2H_{100}N_{12}NiO_{16}{}^{13}C$ $C_{11}H_{114}N_3Ni_2O_2S_3{}^{13}C_5$ $C_5H_{118}N_7NiS_7{}^{13}C_3$ $C_6H_{124}NiO_5S_7{}^{13}C_3$ $C_3H_{20}N_4Ni_6O_4S_3$ $H_{143}NNi_3S_9$
140 cm	4.09	600.843	$C_4H_{26}N_5Ni_4O_8S_3$ $C_8H_{20}N_{10}Ni_5O_2$ $C_{17}H_4N_6NiOS_5{}^{13}C_4$ $C_9HN_{11}Ni_2O_8S^{13}C_3$

			$C_{12}H_{29}Ni_3OS_7{}^{13}C$ $C_{10}H_7N_4Ni_2O_{13}S{}^{13}C_3$ $C_4H_{11}N_8NiO_{11}S_5{}^{13}C$ $C_{11}H_{139}N_3Ni_3S_2{}^{13}C_2$
140 cm	4.11	722.778	$C_{34}H_{107}N_6NiO_4$ $C_6H_{18}N_4NiO_{15}S8$ $C_5H_{143}N_4Ni_4O_{11}S$ $C_{12}H_{14}Ni_2O_{17}S_4{}^{13}C_2$ $C_{11}H_{25}N_4Ni_6O_{2s}2{}^{13}C_5$ $H_{130}N_9NiO_8S_6{}^{13}C_5$ $C_5H_{29}N_8Ni_5S_6{}^{13}C_3$ $C_2HN_{19}Ni_4O_7{}^{13}C_5$ $C_5H_{14}N_{11}Ni_2O_3S_8{}^{13}C_4$ $CH_{20}N_6NiO_9S_{11}{}^{13}C_4$ $C_3H_{128}N_{15}Ni_3O_6S_2{}^{13}C$ $H_{39}N_5Ni_4O_3S_{10}{}^{13}C$ $H_{145}N_6Ni_4O_5S_4{}^{13}C_4$ $C_{17}H_{127}N_6Ni_3OS_2{}^{13}C_4$ $C_3H_7N_{12}Ni_4O_{12}{}^{13}C_5$ $C_6H_{35}NNi_5O_5S_6{}^{13}C_3$
140 cm	3.92	376.824	$C_{123}N_2NiO_2S_3{}^{13}C_2$
140 cm	4.02	480.839	$C_7HN_3NiO_7S_3{}^{13}C_5$ $C_{13}H_{118}N_2NiO_3S{}^{13}C_3$ $H_{130}N_7Ni_3O{}^{13}C_3$
140 cm	4.19	442.891	$C_4H_4N_4NiO_{11}S{}^{13}C_2$
140 cm	4.13	442.890	$C_5H_{10}N_5Ni_2O_7S$ $C_{13}H_{13}NiS_5{}^{13}C$ $H_{12}N_7Ni_2OS_4{}^{13}C_4$
140 cm	4.09	326.898	$C_4H_{18}Ni_3O_2S$
140 cm	4.12	674.772	$C_7H_2N_{17}Ni_3O_5S_3$ $C_4H_{44}Ni_7O_3S_4$
270 cm	3.74	354.893	$C_{11}H_2N_2NiO_5S$
270 cm	3.72	422.880	$C_2H_{18}N_3Ni_4O_5{}^{13}C_2$ $CH_{12}N_{10}Ni_4{}^{13}C_2$
270 cm	3.49	436.780	$C_8H_{105}N_{11}Ni$ $C_2H_3N_9Ni_4O{}^{13}C$
270 cm	3.54	386.853	$C_4H_{20}Ni_3OS_4$ $C_5HNO_7S_5{}^{13}C_3$
270 cm	3.7	460.857	$CH_{34}Ni_4S_5$ $H_{131}N_5Ni_3O_2{}^{13}C_4$

270 cm	3.57	364.964	$CH_{19}N_4Ni_3O_4{}^{13}C_3$
270 cm	3.72	442.891	$C_3H_{127}N_4NiO_3S_2{}^{13}C_4$ $H_8N_{11}Ni_3O_5{}^{13}C_2$
270 cm	3.83	456.908	$C_4H_{18}NNi_3O_{11}{}^{13}C_2$ $C_6H_{25}NiO_2S_8{}^{13}C$ $C_2H_{16}N_{10}Ni_3O_3S$ $C_{15}H_4N_5NiO_5S_2$
270 cm	3.81	428.913	$C_8H_{20}N_3Ni_3O_2S_2$
270 cm	3.86	474.905	$C_{10}H_{128}N_5Ni_2{}^{13}C_3$ $C_4H_{11}N_6Ni_2O_4S_2{}^{13}C_5$
270 cm	3.89	330.915	$C_7H_{10}N_2NiO_2S_3$
270 cm	3.86	361.925	$C_3H_{23}Ni_2S_5{}^{13}C_2$

VITA

Theresa Whorley was born in Naples, Italy the day an earthquake beneath Mt. Vesuvius shook the hospital. Thus began her enthusiasm for geology. She received her Associate of Arts degree from the Florida State College at Jacksonville in 2011 then moved on to earn her Bachelor of Science degree from the University of South Florida in 2013. She majored in Geology during her undergraduate studies and became fascinated with using chemistry as a tool to understand geologic phenomena and the impact biology can play in masking geochemical signals. In 2014, Theresa joined the University of Washington School of Oceanography to study marine sediment pore water biogeochemistry where she carved out a research niche that utilized biology, chemistry, and geology to answer fundamental questions in the deep biosphere. She has been to sea on four research expeditions and become one of only a few people in the world capable of building two specific benthic fluid flow meters. While pursuing graduate studies, Theresa was fortunate to teach many undergraduate courses and share her excitement for science with other students. For this, she earned the Dean A. McManus Excellence in Teaching Award in 2020. In 2021, Theresa earned a Doctor of Philosophy degree in Oceanography with a focus in marine geology and geochemistry and currently works and lives in Seattle, WA with her family.